UNIVERSITÀ POLITECNICA
DELLE MARCHE
FACOLTÀ DI INGEGNERIA

Corso di Laurea Triennale in Ingegneria Gestionale

"Effetti delle impurità nella CO_2 nel trasporto via pipeline"

"Effect of impurities on CO_2 during pipeline transportation"

Relatore: ***Chiar.mo***

Prof. **Francesco CORVARO**

Laureando:

Giulio Rastelli

Anno Accademico 2019-2020

Table of contents

Riassunto dell'elaborato in lingua italiana

Questa tesi ha avuto come obiettivo quello di valutare gli effetti delle impurità durante il trasporto della CO_2 per via pipeline, in tutte le sue sfaccettature, passando dall'impatto sulle proprietà termodinamiche della CO_2 alle conseguenti problematiche legate alle caratteristiche tecniche e meccaniche della conduttura. La stesura dell'elaborato è stata possibile grazie all'analisi e alla lettura di articoli scientifici (presenti nella pagina dei riferimenti), più o meno recenti. È stata una scelta voluta quella di fare riferimento ad articoli pubblicati in anni diversi in modo da poter apprezzare meglio, nei casi studio considerati, le differenze negli approcci sperimentali degli stessi. La tesi è stata suddivisa in quattro capitoli, seguirà un sunto di quanto visto nei capitoli appena citati. Il primo capitolo, suddiviso in tre paragrafi, è una breve introduzione allo scenario del trasporto del diossido di carbonio per via pipeline, in cui è presente un quadro generale delle esistenti pipeline in giro per il mondo, con annessi cenni storici, ponendo particolare enfasi, nel continuo del capitolo, su quelle presenti negli Stati Uniti, che risulterà essere la nazione con maggior affluenza di queste tecnologie. A chiudere questa parte vi è un paragrafo dedicato alle applicazioni più comuni di queste procedure riferendosi sempre agli Stati Uniti. Il secondo capitolo è il cuore della tesi, in quanto sono affrontate in maniera più approfondita le tematiche salienti riguardanti le impurità, anche qui il capitolo è stato suddiviso in tre paragrafi. Il primo descrive le tipiche proprietà termodinamiche della CO_2 nel suo stato supercritico (stato tipicamente usato nelle operazioni di cattura e stoccaggio del carbonio, CCS), in modo tale da aver posto le basi per poter trarre le conseguenti considerazioni nel paragrafo successivo, legato proprio agli effetti sulle proprietà termodinamiche sopra citate. In questa sezione sono stati trattati due casi studio, diversi per quanto riguarda le modalità ma in linea di massima convergenti agli stessi risultati. Il primo caso studio ha avuto un approccio di tipo sperimentale, mediante la combinazione di diversi strumenti, come per esempio trasduttori di pressione e densimetri. Dal punto di vista quantitativo l'approccio è stato di tipo analitico, mediante l'utilizzo delle equazioni più idonee per i casi specifici. Il secondo caso studio, a differenza del precedente, è stato realizzato mediante l'uso di software di simulazione, in particolare Apem HSYS, un simulatore di processi chimici, e gPROMS, un software di modellazione generale. I risultati sono stati espressi in funzione delle grandezze densità, viscosità, temperatura e pressione, che inevitabilmente hanno subito variazioni. L'ultimo paragrafo di questo capitolo tratta le principali problematiche strutturali della conduttura causate proprio dalle variazioni delle proprietà termodinamiche della CO_2 viste precedentemente. In particolare, per affrontare queste tematiche, è stato introdotto un terzo caso studio nel quale viene valutato il fenomeno della corrosione su materiali in gomma sottoposti al passaggio del flusso di CO_2 affetta da diverse impurità. Successivamente, oltre al fenomeno della corrosione sono stati valutati gli effetti delle impurità su diverse caratteristiche delle pipeline, ovvero la capacità di stoccaggio, la selezione dei materiali e le prestazioni dei compressori. Il terzo capitolo affronta la tematica dei possibili guasti che possono interessare la conduttura. Nello specifico, anche qui si è fatto riferimento ad un caso studio. Data la recente pubblicazione dell'articolo (2019), il caso studio è risultato essere "più completo" rispetto agli altri visti nelle sezioni precedenti in quanto è stato realizzato mediante la combinazione di più metodologie: una puramente sperimentale, una numerica ed una di simulazione. A seguire è stato dedicato un paragrafo all'analisi dei risultati ottenuti in questo esperimento.

Il quarto e ultimo capitolo invece verte a definire a grandi linee una revisione sistematica dei processi di trasporto della CO_2 odierni (in riferimento ad un articolo pubblicato nel 2020), ponendo particolare enfasi ai progetti previsti per il futuro. In conclusione viene ripreso il discorso delle impurità, definite comunque molto impattanti sul processo e quindi non trascurabili, tuttavia non esiste ancora una metodologia sistematica per valutare l'impatto delle diverse impurità sull'equilibrio di fase e sulla corrosione delle pipeline.

References

[1] Paul Noothouta, Frank Wiersmaa, Omar Hurtadob, Doug Macdonaldb, Jasmin Kemperc, Klaas van Alphend (2014). "*CO_2 Pipeline infrastructure – lessons learnt*." Faculty of Engineering, University of Wollongong, Northfields Ave, Wollongong, NSW 2522, Australia.

[2] Forbes, S. M., Verma, P., Curry, T. E., Friedmann, S. J., & Wade, S. M. (2008). "*Guidelines for carbon dioxide capture, transport and storage."*

[3] Global CCS Institute, Guloren Turan, General Manager, Advocacy and Communications (2020). "*CCS: Applications and Opportunities for the Oil and Gas Industry*."

[4] Antoine Oosterkamp, Joakim Ramsen (2008). "*State-of-the-Art Overview of CO_2 Pipeline Transport with Relevance to Offshore Pipelines*".

[5] Antonin Chapoya, Mahmoud Nazeri, Mahdi Kapateha, Rod Burgass, Christophe Coquelet, Bahman Tohidi (2013). *"Effect of impurities on thermophysical properties and phase behaviour of a CO_2-rich system in CCS".*

[6] Suoton Philip Peletiri, Iqbal M. Mujtaba, Nejat Rahmanian (2019). *"Process simulation of impurity impacts on CO2 fluids flowing in pipelines"*.

[7] Filip Neele, Joris Koornneef, Jana Poplsteinova Jakobsen, Amy Brunsvold, Charles Eickhoff, (2017). "*Toolbox of effects of CO_2 impurities on CO_2 transport and storage systems*".

[8] Dajiang Zhu, Yuanhua Lin, Huali Zhang, Yufei Li, Dezhi Zeng, Wanying Liu, Chen Qiang, Kuanhai Deng (2017), *"Corrosion evaluation of packer rubber materials in CO_2 injection wells under supercritical conditions".*

[9] Malgorzata Halseid, Arne Dugstad, Bjørn Morlan (2014). *"Corrosion and bulk phase reactions in CO_2 transport pipelines with impurities: review of recent published studies".*

[10] Jinsheng Wang, David Ryan, Edward J. Anthony, Neil Wildgust, Toby Aiken (2011). *"Effects of Impurities on CO_2 Transport, Injection and Storage".*

[11] Wetenhall, B. , Aghajani, H. , Chalmers, H. , Benson, S.D. , Ferrari, M-C. , Li, J. , Race, J.M., Singh, P. , Davison, J. (2014). *"Impact of CO_2 impurity on CO_2 compression, liquefaction and transportation".*

[12] S.B. Martynov, N.K. Daud, H. Mahgerefteh, S. Brown1 R.T.J. Porter (2016). *"Impact of stream impurities on compressor power requirements for CO_2 pipeline transportation".*

[13] Chima Okezue and Dmitriy Kuvshinova (2017). *"Effect of Chemical Impurities on Centrifugal Machine Performance: Implications for Compressor Sizing In A CO_2 Transport Pipeline".*

[14] Xiong Liu, Ajit Godbole, Cheng Lu, Guillaume Michal, Valerie Linton (2019). *"Investigation of the consequence of high-pressure CO_2 pipeline failure through experimental and numerical studies".*

[15] Hongfang Lu, Xin Ma, Kun Huang, Lingdi Fu, Mohammadamin Azimi (2020). "*Carbon dioxide transport via pipelines: A systematic review".*

CHAPTER 1 – INTRODUCTION

1.1 General description of CO_2 transport process

Nowadays, there are over 6,500 km of CO_2 pipelines in North-America, Europe, the Middle East, Africa and Australia (Ref.[1]). Some of these pipelines have been operating for many years, mostly to transport CO_2 for enhanced oil recovery (EOR) operations in the Americas. Some pipelines are linked to Carbon Capture and Storage (CCS) projects and some pipelines (associated with CCS) are currently under development. Worldwide there are over eighty CO_2 pipeline projects, twenty-nine of these projects have been carefully selected (as shown in Table 1) in order to cover all key regions and conditions in a balanced way. In this process the following main criteria were taken into consideration:

- Geographical coverage;
- Onshore and offshore;
- Time of construction covering both recent and older projects;
- EOR and storage projects;
- Existing and planned;
- Conventional and new concepts;
- New-built and reuse of pre-existing pipelines.

For each of these pipelines a database was populated. A checklist was prepared for this purpose covering all sought data elements. The first step in data gathering was to carry out a literature survey of the selected CO_2 pipeline projects. The following sources were consulted:

- Project websites;
- Environmental Impact Assessments or Environmental Statements;
- Reports on pipeline routes (sometimes as part of a permit application);
- FEED-studies;
- Journal articles, including scientific articles.

	Project name	Country code[a]	Status[b]	Length (km)	Capacity (Mton/y)	Onshore / Offshore	Sink[c]
	North-America						
1	CO_2 Slurry	CA	P	Unknown	Unknown	Onshore	EOR
2	Quest	CA	P	84	1.2	Onshore	Saline aquifer
3	Alberta Trunk Line	CA	P	240	15	Onshore	Unknown
4	Weyburn	CA	O	330	2	Onshore	EOR
5	Saskpower Boundary Dam	CA	P	66	1.2	Onshore	EOR
6	Beaver Creek	US	O	76	Unknown	Onshore	EOR
7	Monell	US	O	52.6	1.6	Onshore	EOR
8	Bairoil	US	O	258	23	Onshore	Unknown
9	Salt Creek	US	O	201	4.3	Onshore	EOR
10	Sheep Mountain	US	O	656	11	Onshore	CO_2 hub
11	Slaughter	US	O	56	2.6	Onshore	EOR
12	Cortez	US	O	808	24	Onshore	CO_2 hub
13	Central Basin	US	O	231.75	27	Onshore	CO_2 hub
14	Canyon Reef Carriers	US	O	354	Unknown	Onshore	Unknown
15	Choctaw (NEJD)	US	O	294	7	Onshore	EOR
16	Decatur	US	O	1.9	1.1	Onshore	Saline aquifer
	Europe						
17	Snøhvit	NO	O	153	0.7	Both	Porous Sandstone formation
18	Peterhead	UK	P	116	10	Both	Depleted oil/gas field
19	Longannet	UK	C	380	2	Both	Depleted oil/gas field
20	White Rose	UK	P	165	20	Both	Saline aquifer
21	Kingsnorth	UK	C	270	10	Both	Depleted oil/gas field
22	ROAD	NL	P	25	5	Both	Depleted oil/gas field
23	Barendrecht	NL	C	20	0.9	Onshore	Depleted oil/gas field
24	OCAP	NL	O	97	0.4	Onshore	Greenhouses
25	Jänschwalde	DE	C	52	2	Onshore	Sandstone formation
26	Lacq	FR	O	27	0.06	Onshore	Depleted oil/gas field
	Rest of the World						
27	Rhourde Nouss-Quartzites	DZ	P	30	0.5	Onshore	Depleted oil/gas field
28	Qinshui	CN	P	116	0.5	Onshore	ECBMR
29	Gorgon	AU	P	8.4	4	Onshore	Sandstone formation

[a] Country codes: AU=Australia, CA=Canada, CN=China, DE=Germany, DZ=Algeria, FR=France NL=Netherlands, NO=Norway, UK=United Kingdom, US=United States

[b] Legend status: P=Planned, O=Operational and C=Cancelled

[c] EOR=Enhanced Oil Recovery, ECBMR=Enhanced Coal Bed Methane Recovery

Figure 1 "CO_2 pipeline projects included in the assessment", (Ref. [1]).

Afterwards, pipeline owners were contacted to seek additional information. Contacts were established by telephone, email and face-to-face meetings by their offices and at conferences. Many interviews were conducted and additional information was obtained that could not be retrieved from literature.

1.1.2 Main characteristics of CO_2 pipelines

The objective of CO_2 pipelines is to connect sinks and sources with each other. The most common CO_2 sources are gas, processing plants, fossil-fuelled power stations and natural sources of CO_2.Common sinks are oil fields for EOR, but also depleted oil and gas fields are used. The advantage of these storage sites is that there is existing infrastructure in place that may be reused for CO_2 transportation and injection. In some of the European projects existing infrastructure has been reused or this option is being considered.

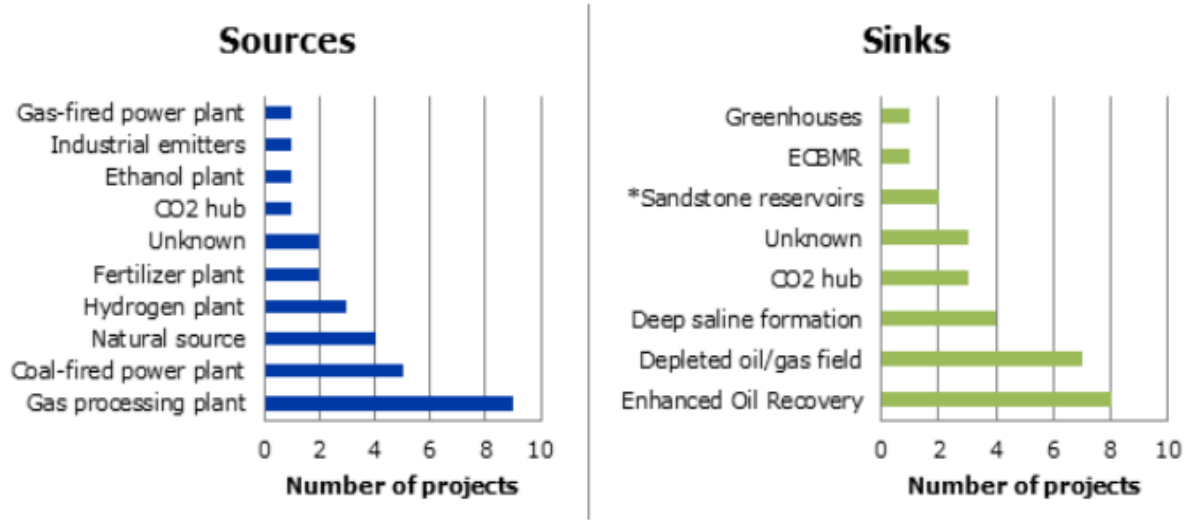

Table 1"Sources and sinks of the twenty-nine CO_2 pipeline projects studied", (Ref.[1]).

The purity of the CO_2 stream depends on the CO_2 source and, if appropriate, the CO_2 capture technology (for example the design and construction of CO_2 pipelines). In all 29 pipeline projects (Table 1) the purity exceeds 95% and $\frac{1}{3}$ of the projects deliver a purity greater than 99%. The most relevant impurities in the CO_2 stream are H2O, N2, O_2, H2S and CO.Where multiple CO_2 sources and sinks exist, a transmission and distribution network it could be possible to develop a hub. CO_2 hubs have no specific set of rules because they are usually developed ad-hoc when CO_2 sources are available and/or a viable market exists. Each hub has its own standards for CO_2 purity, acceptable impurities, pressure and temperature. The physical characteristics of the CO_2 pipelines can vary considerably. For example, the range in length lies between 1.9 and 808 km, shows the spread including other characteristics such as diameter and wall thickness.

Parameter	Range
Length (km)	1.9 - 808
External diameter (mm)	152 – 921
Wall thickness (mm)	5.2 – 27
Capacity designed (Mt/y)	0.06 – 28
Pressure min (bar)	3 – 151
Pressure max (bar)	21 – 200
Compressor capacity (MW)	0.2 - 68

Table 2 "Physical characteristics of CO_2 pipelines", (Ref.[1]).

The inclusion of short-distance demonstration projects as well as commercial, long-distance EOR projects is the main reason for the large variation. Another interesting point is a positive correlation between length and capacity of the pipelines; longer pipelines have to transport larger volumes of CO_2 to be economically viable. In many respects, CO_2 pipelines are comparable to natural gas pipelines but there are the following key differences:

• The properties of CO_2 lead to different design parameters.
• In many places CO_2 pipeline projects are first-of-a-kind.
• CO_2 pipelines do not transport a product that people see as directly beneficial.
• Risks associated with geological storage and the Lake Nyos incident (a limnic eruption in 1986) in influence the public perception of CO_2 pipelines.

The project cycle typically takes between 3 to 6 years from concept stage to the final investment decision. The actual construction time usually lies typically between 1 and 4 years depending on the length and complexity of the pipeline (Ref.[1]).Generally a CCS project can start in different ways, for example using existing CO_2 pipeline infrastructure and the development of dedicated pipelines that are sized and located for individual projects to accommodate the CO_2 specifications of those projects. Another scenario could be a fully integrated network that utilizes CO_2 from several sources. In light of the overall costs associated with CO_2 pipelines, including the uncertainty about future material costs and cost recovery, some analysts anticipate that the CO_2 network for CCS will begin with short pipelines from CO_2 sources located close to storage sites, with a larger regional network of interconnected lines developing as the number of projects grows.

Another study estimates that storage reservoirs may be sufficiently distributed, such that 77% of the total annual CO_2 emissions from the major North American sources may be stored in reservoirs directly underlying these sources, and an additional 18 percent may be stored within 100 miles of the original sources. As geologic formations are characterized in more detail and suitable repositories are identified, CO_2 sources can be mapped against storage sites with increasing certainty (Ref.[2]).

1.2 Historical notes

In the United States, significant CO_2 pipeline operating experience exists in the EOR industry. Since the early 1970s, pipeline companies have been successfully operating a substantial CO_2 pipeline infrastructure (Figure 2), transporting an estimated 0.78 trillion cubic feet of CO_2 per year through an estimated 3,900 miles1 of infrastructure, through pipelines of varying diameters, mainly for use in EOR. The Permian Basin region of West Texas and New Mexico remains the centre of CO_2-based EOR activity. The oldest long-distance CO_2 pipeline in the United States is the 140-mile Canyon Reef Carriers pipeline, which began service in 1972 for EOR in regional Texas oil fields. The longest CO_2 pipeline, the 502-mile Cortez pipeline, has been delivering about 20 million metric tons of CO_2 per year to the CO_2 hub in Denver City, Texas, since 1984 (Ref.[2]).

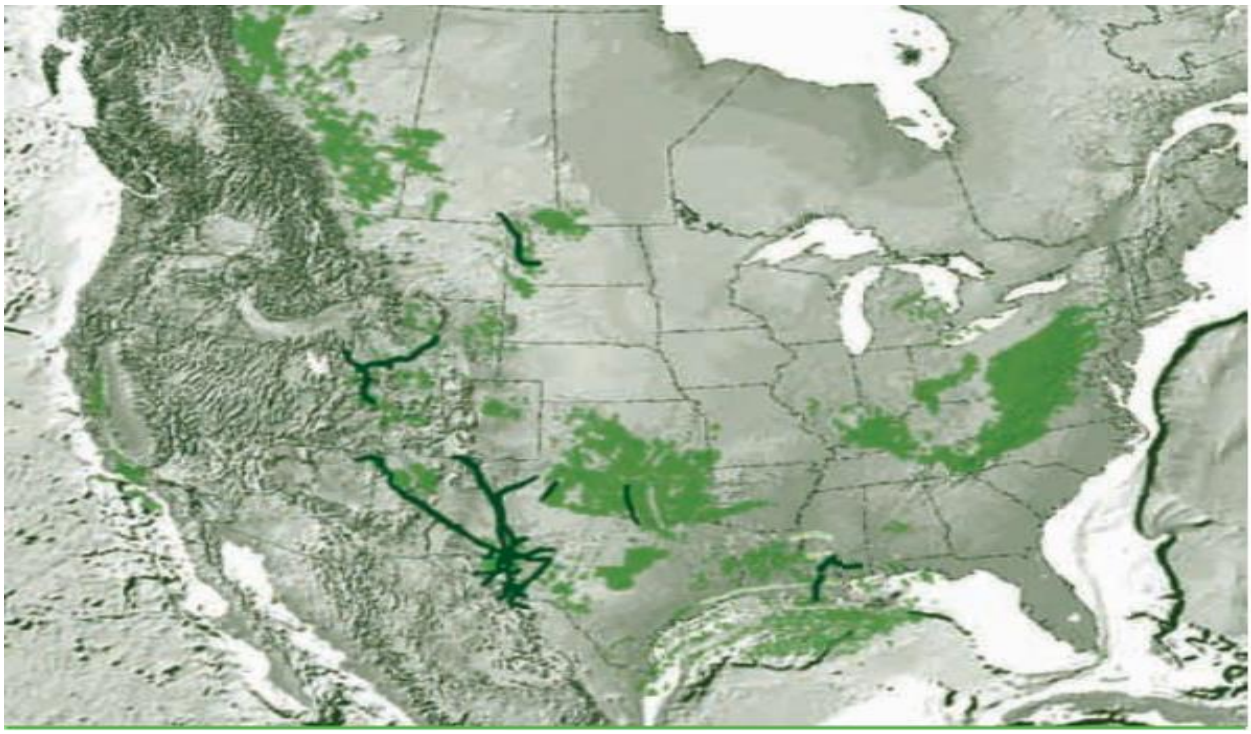

Figure 2 "Existing CO_2 Pipelines in the USA", (Ref.[2]).

1.3 Some applications

Most of the CO_2 transport applications (talking about lower-cost opportunities) are in gas processing (Ref.[3]). Some of the most common applications are listed here below:

• **Ethanol production**, is a lower cost application of CCS. Currently the only commercial scale ethanol plant with CCS is the Illinois Industrial CCS facility , but there is increased interest from both project developers and finance community due to smaller scale and ease of replicability of ethanol applications coupled with supportive policies in the US, including the 45Q tax credit and CCS Protocol in California's Low-Carbon Fuel Standard. In 2018, White Energy and Oxy announced plans to capture CO_2 from White Energy's two ethanol facilities in the Midwest US.

• **Refining**, is a part of the oil value chain that provides an opportunity to apply CCS.
Refineries have several units that emit CO_2, including steam methane reformers that produce hydrogen, catalytic crackers and Combined Heat and Power (CHP) units. Currently there are two refineries (Shell's Quest Refinery and Air Products' Steam Methane Reformer at the Port Arthur refinery) that capture and store CO_2 from their steam methane reformers (SMRs), whilst a third (Sturgeon Refinery) is scheduled to come online in 2020.

• **Gas-fired power generation,** it offers another emerging application for CCS. NetPower's 50 MW first of a kind natural gas-fired demonstration power plant in the US employs Allam cycle technology, which uses CO_2 as a working fluid in a supercritical CO_2 power cycle. The plant, first operated in 2018, aims to demonstrate it can produce zero-carbon electricity at costs competitive to conventional power generation.

• **Direct Air Capture (DAC)**, is a nascent but promising technology which enables 'sucking' CO_2 from the atmosphere as opposed to large emission sources. Whilst it is not directly linked to the operations of oil and gas companies, DAC could enable capturing and storing residual atmospheric emissions. As several oil and gas majors have started to aim for and commit to emission reduction targets, including from the end-use of their products, utilizing DAC is likely to emerge as a possible option to meet these targets.

CHAPTER 2 – THE EFFECT OF IMPURITIES IN CO_2 TRANSPORT

2.0 Typical thermodynamics and operating parameters

CO_2 used for carbon dioxide capture and storage is typically in the supercritical stage, where the density resembles a liquid but it expands to fill space like a gas. Supercritical CO_2 is purchased, as a commodity, to be used in many industrial processes. In the climate change context CO_2 is mostly classified as an important greenhouse gas, an emission, or in some countries as a waste. In response to this concern, the Interstate Oil and Gas Compact Commission recommends that CO_2 shall not be classified as a waste and therefore it suggests states to adopt a legislation recognizing CO_2 of a certain purity as a commodity. Some stakeholders have advocated for the setting of a >90 % CO_2 purity standard, but many feel that, considering the existing uncertainty about the precise composition of the CO_2 stream, the best solution is to design projects with materials and procedures that account for any co-constituents in the gas stream (Ref.[2]). Many properties of pure CO_2 have been extensively studied, but only a few of them are relevant for the transport by pipeline, these properties will be shown in this section (Ref.[4]).

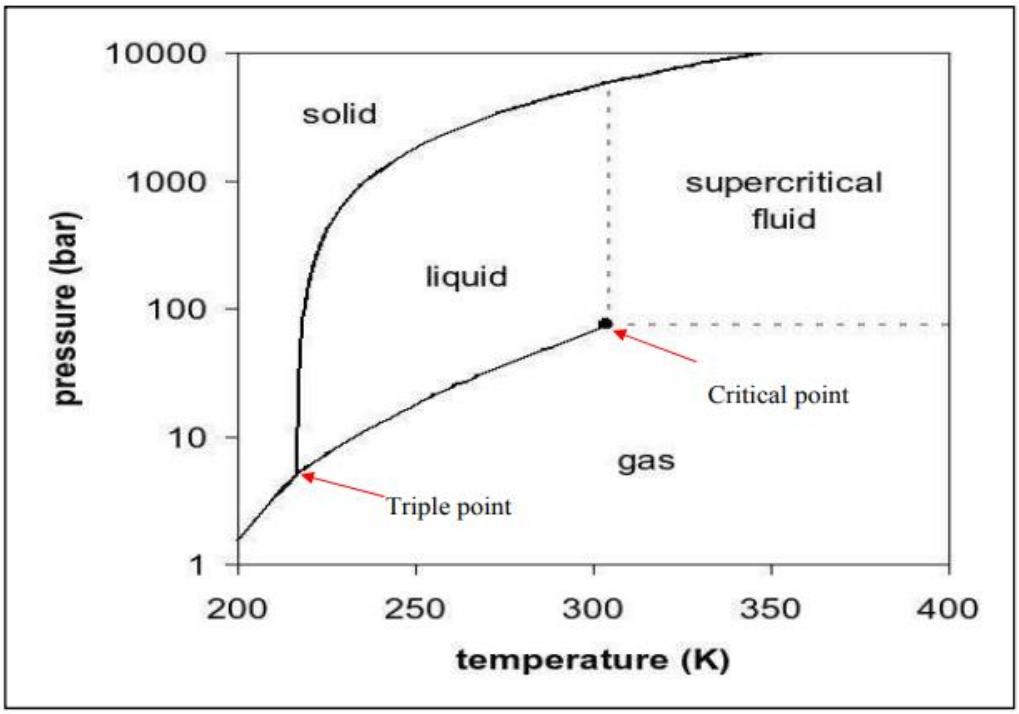

Figure 3 "Phase diagram for pure CO_2", (Ref.[4]).

It is important to note (Figure 3) that pure CO_2 has a triple point at -56.6 ºC and 5.18 bara. It has its critical point at 30.9782 ºC and 73.773 bara. This has implications for both compression and transport conditions. It shall be noted that above the critical point CO_2 will not be able to separate in two phases (except at very low temperature or high pressure where solid CO_2 can form).The diagram shown here below can be used to estimate how the temperature changes during de-pressurization, e.g. over a valve (Figure 4) .

Note that the isotherms are almost vertical at low temperatures. This means that a throttling in this region (liquid) will not alter the temperature significantly as long as the CO_2 is kept in one phase. The Pressure-Enthalpy diagram is also used to visualize the thermodynamic path for compression and pumping. It can be seen from the diagram that in the liquid region relatively low energy input is necessary to increase the pressure, compared to compression of the gas (isentropic lines are steeper).

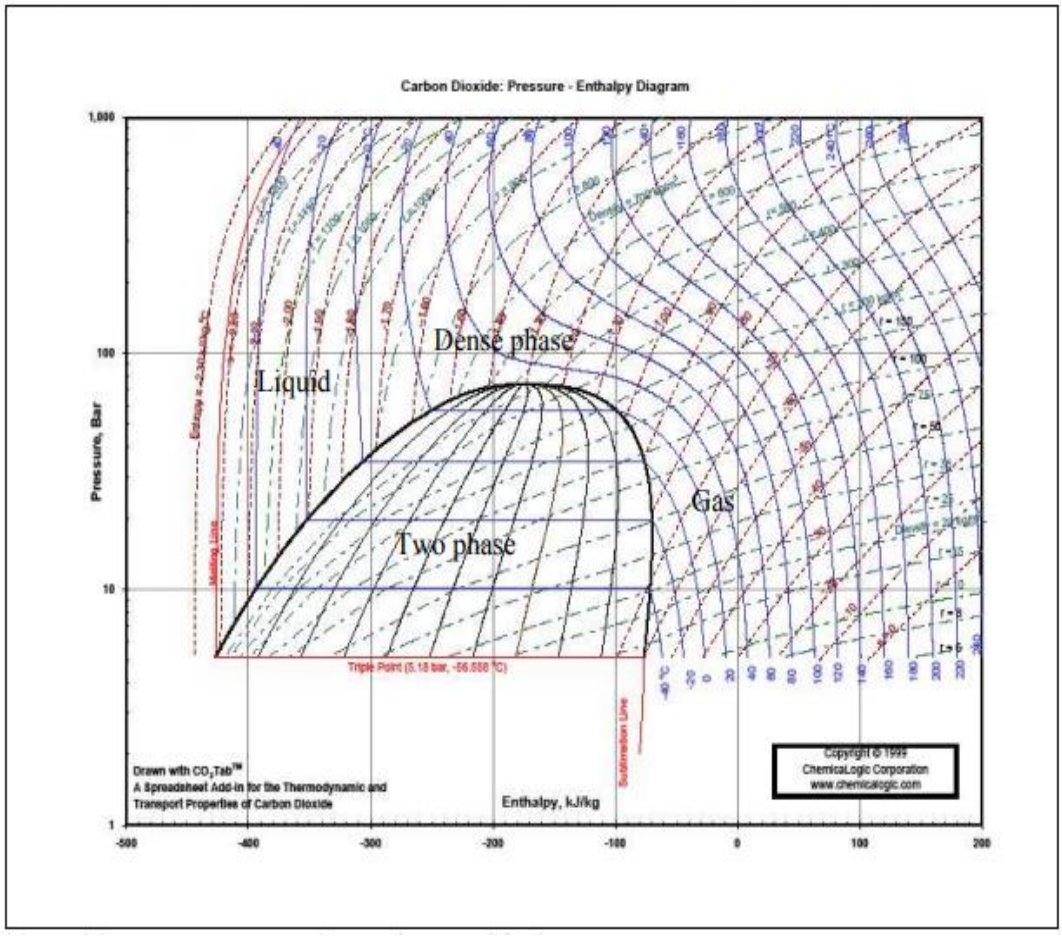

Figure 4"Pressure-Enthalpy diagram for pure CO_2", (Ref.[4]).

In the following pages other characteristics of pure CO_2 relevant for the transport process by pipeline will be described.

• ***Density***, as it can be seen from Figure 5, the density of CO_2 has a stronger dependency on temperature than pressure at lower temperatures. It can also be seen that the density is very sensitive to small temperature changes near the critical point. Density is an important factor in flow calculations. This means that accurate knowledge of inlet temperature, ambient temperature and heat transfer is necessary to model the flow correctly, especially if conditions are close to the critical point.

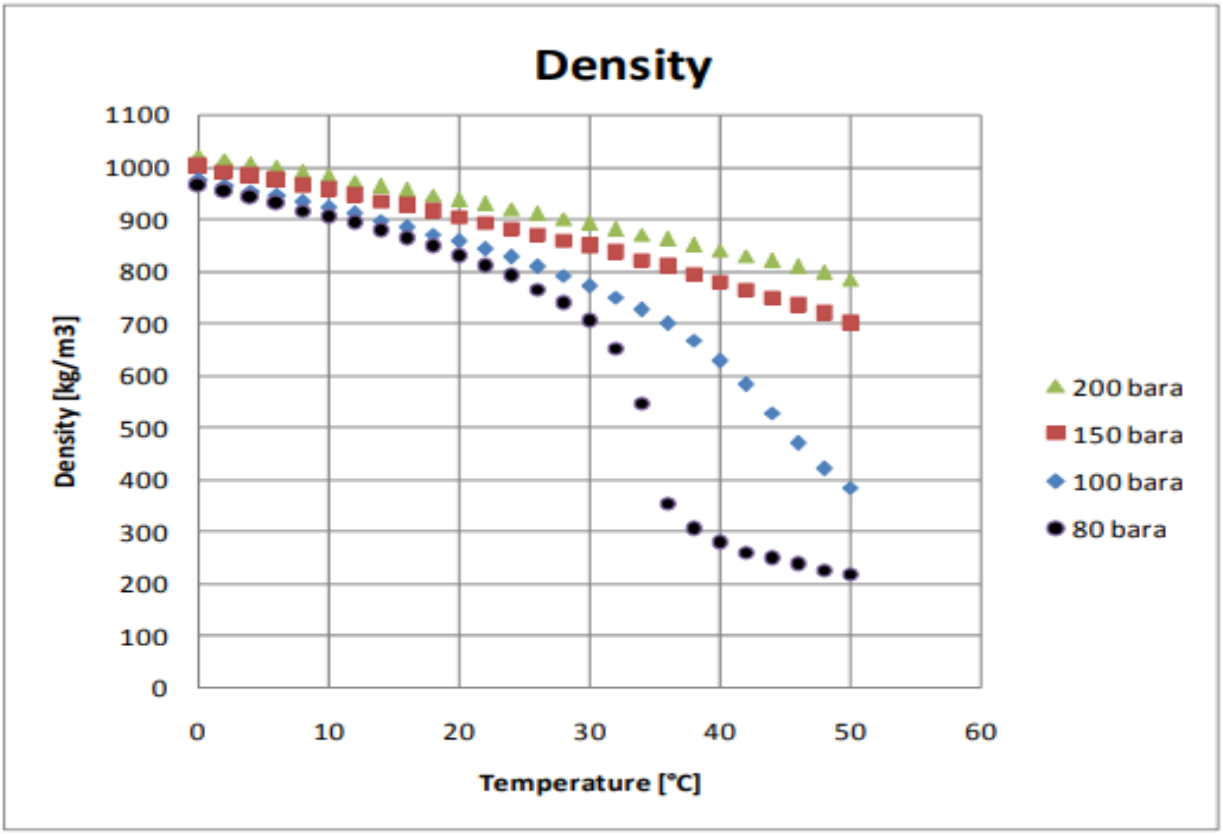

Figure 5 "Density of CO2 as function of temperature and pressure", (Ref.[4]).

It is the combination of high molecular weight and low compressibility factor (Z-factor) that makes CO_2 density so temperature dependent.

• ***Z factor***, the compressibility factor at different temperatures and pressures is shown in Figure 6. It shows that ideal gas assumption for CO_2 is not applicable. The compressibility factor is used to alter the ideal gas equation to account for the real gas behaviour. For an ideal gas, the Z-factor will be one, independent of pressure and temperature. The compressibility factor needs to be taken into account to give correct density in flow calculations.

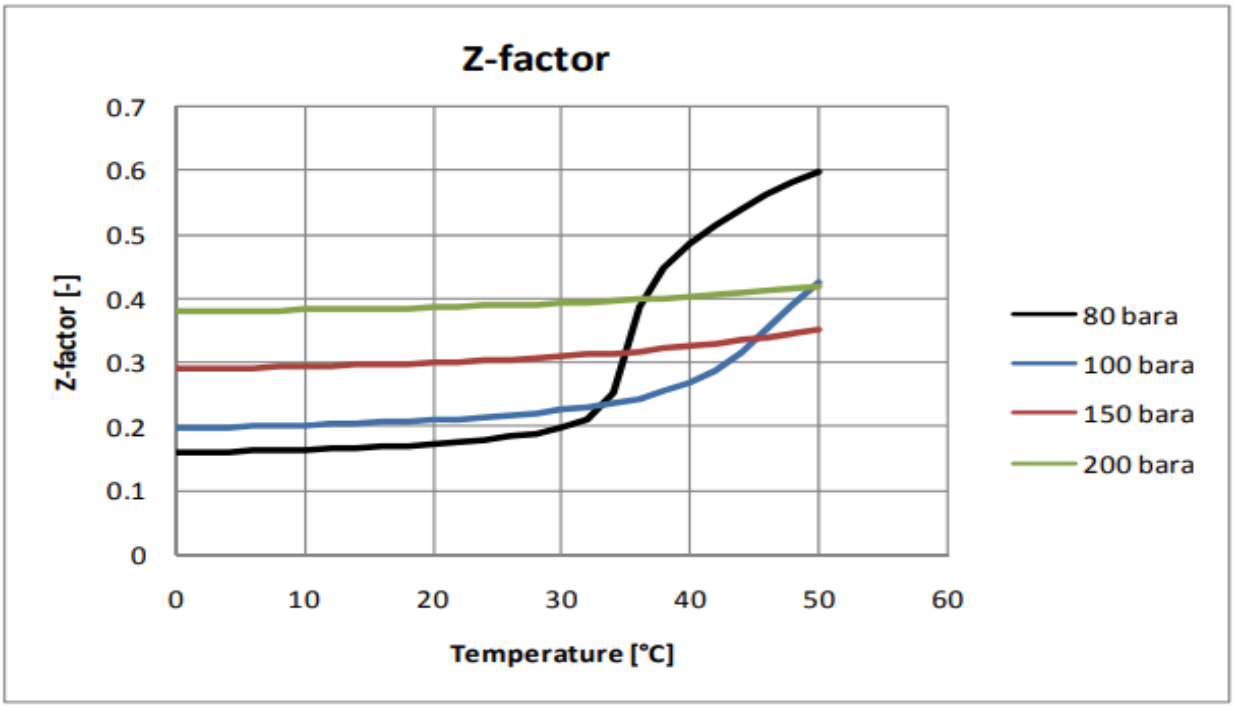

Figure 6 "Compressibility factor (z-factor) at different pressures and temperatures", (Ref. [4]).

• ***Viscosity,*** CO_2 has a low viscosity compared to some other high-density fluids, for example olive oil (80 cP), water (0.89 cP). Viscosity of CO_2 versus temperature at different pressures is shown in Figure 7. As it can be seen from the figure above, also the viscosity of CO_2 shows a strong temperature dependency, especially near the critical point.

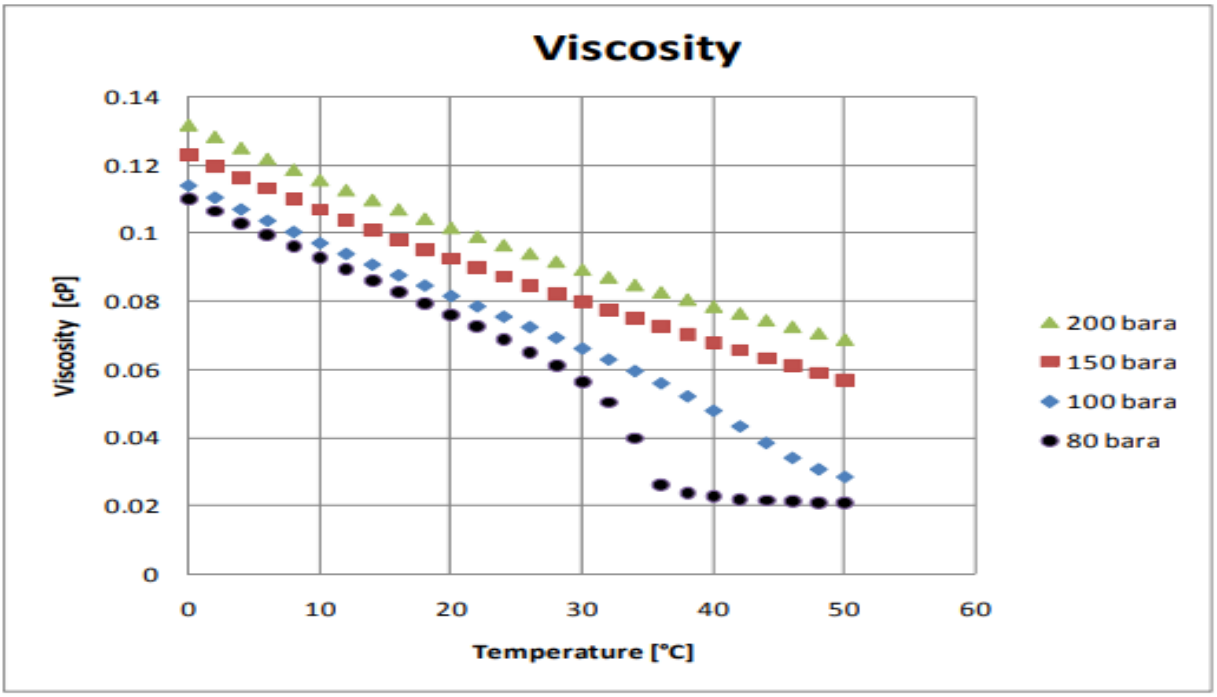

Figure 7 "Viscosity of CO2 as function of temperature and pressure", (Ref. [4]).

2.1 Effects on thermodynamic properties

Impurities in the CO_2 can affect the phase behaviour, the thermodynamic properties and the viscosity. For example small amounts of hydrogen in the CO_2 will increase the vapour pressure significantly (Ref.[4]).

2.1.1 Effects on Density, Viscosity and Vapour Pressure

The following section contains a series of diagrams that show how the impurities impact on thermodynamic properties of pure CO_2. The composition, used to produce the diagrams, is 98 mole% CO_2 with 2 mole% of the other component (Ref.[4]).

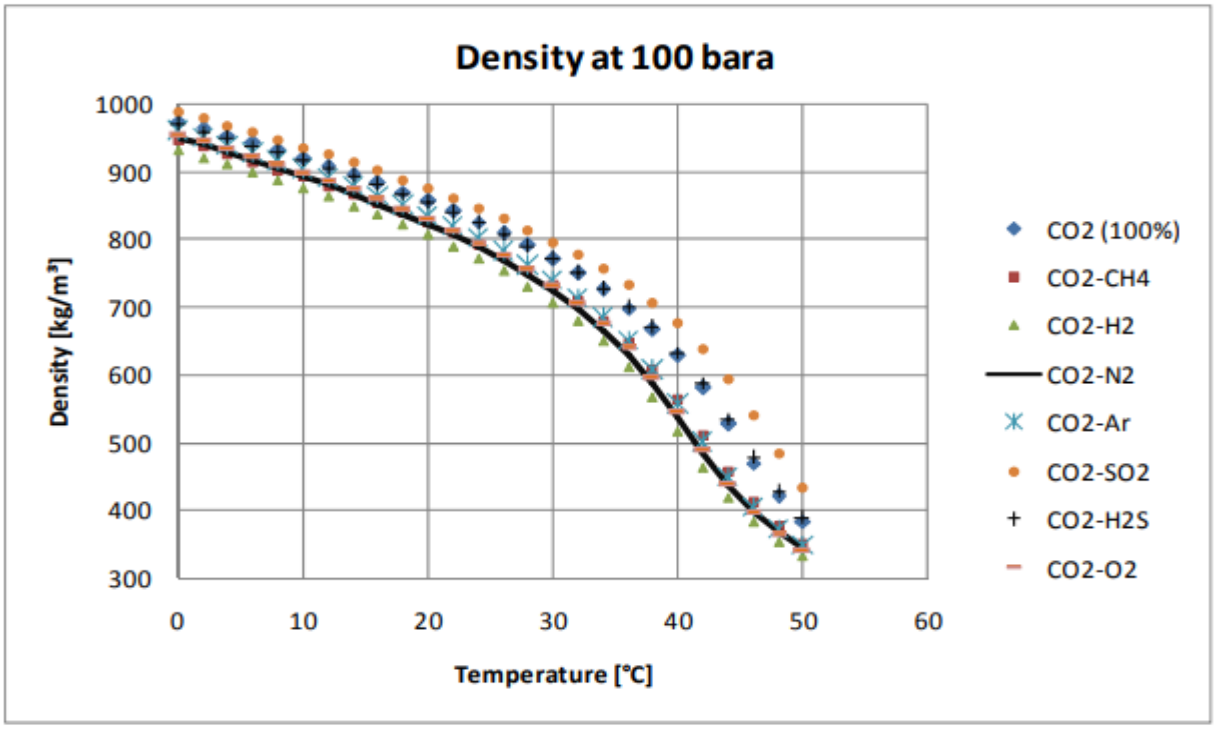

Figure 8 "Density at 100 bara with different temperatures for CO_2 with mole% of another component.", (Ref.[4]).

As we can see in Figure 9 SO_2 is the only component that increases the density compared to pure CO_2. The estimated density for this mixture is very uncertain since no mixture parameters were available. From this figure it can be seen that H_2S has minimal impact on the fluid density while H_2 has a significant impact.

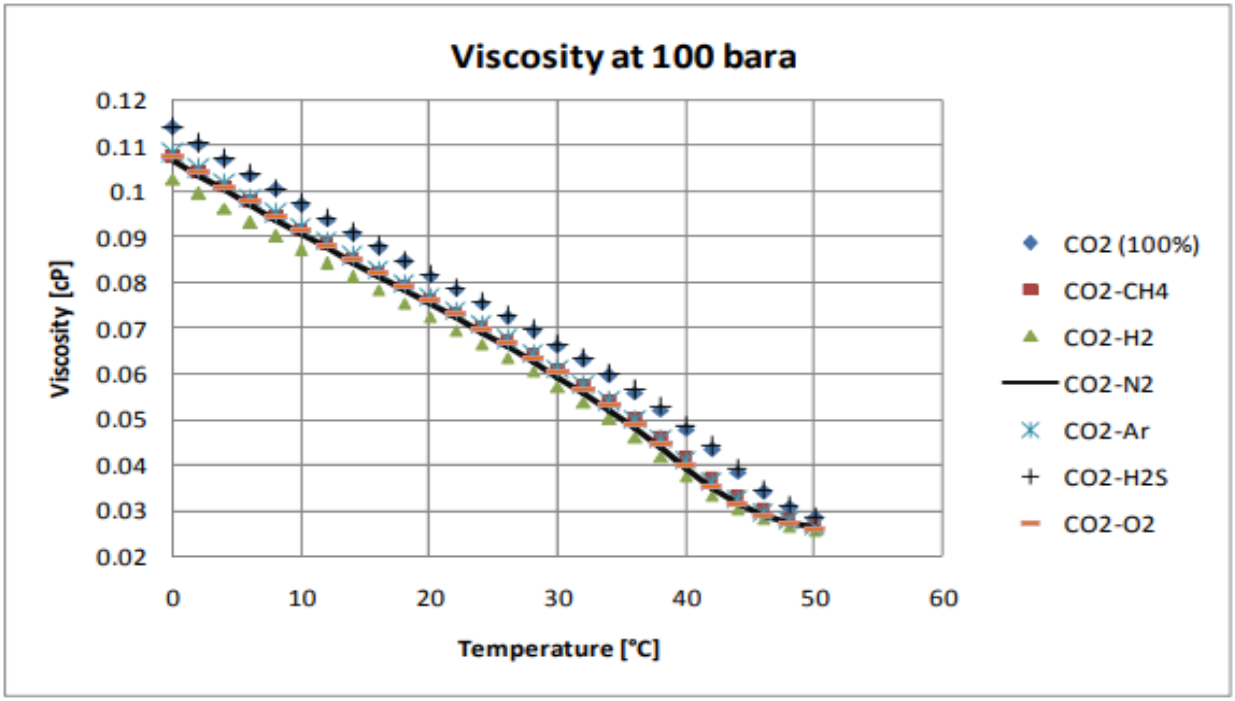

Figure 9 "Viscosity at 100 bara with different temperatures for CO_2 with 2 mole% of another component", (Ref.[4]).

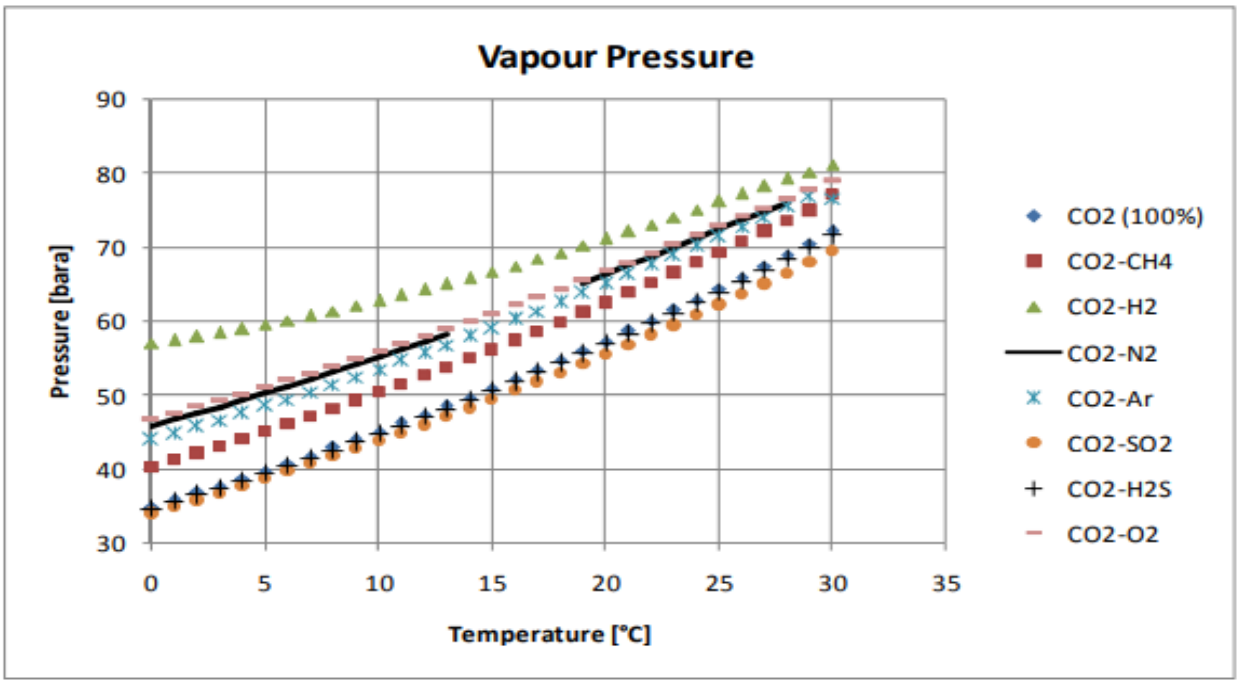

Figure 10 "Vapour pressure for different mixtures (98 mole% CO_2)", (Ref.[4]).

Figure 9 indicates that impurities typically will reduce the viscosity. It can be seen, in Figure 10, that the presence of impurities has a significant effect on the vapour pressure. Exceptions are H_2S and SO_2. As with the other properties, the values for CO_2-SO_2 mixture are very uncertain since the mixing parameters were estimated and not based on any actual measurement data. The presence of impurities implies that a two-phase region will be present.

2.1.2 Case study 1 – Experiment: CO_2-rich system, evaluation of thermodynamic parameters

The previous considerations about the effects of impurities on thermodynamic properties (Ref.[4]) were based on a study made using REFPROP program from NIST (National Institute of Standards and Technology) to evaluate graphically how impurities affect density, viscosity and vapour pressure. In this paragraph we will see a case study that shows a practical approach divided into two parts, an experimental and an analytical one based on mathematical models, to estimate the issues derived from impurities.

2.1.2.1 Set-up

All viscosity measurements were conducted in an in-house designed and constructed set-up, a schematic view is shown in Figure 11. This set-up has been designed to have a maximum working pressure of 200 Mpa and a maximum working temperature of 523.15K. The set-up is located inside the chamber of an oven, manufactured by BINDER GmbH, capable of being used at temperatures from 203.15 to 473.15K (Ref.[5]).

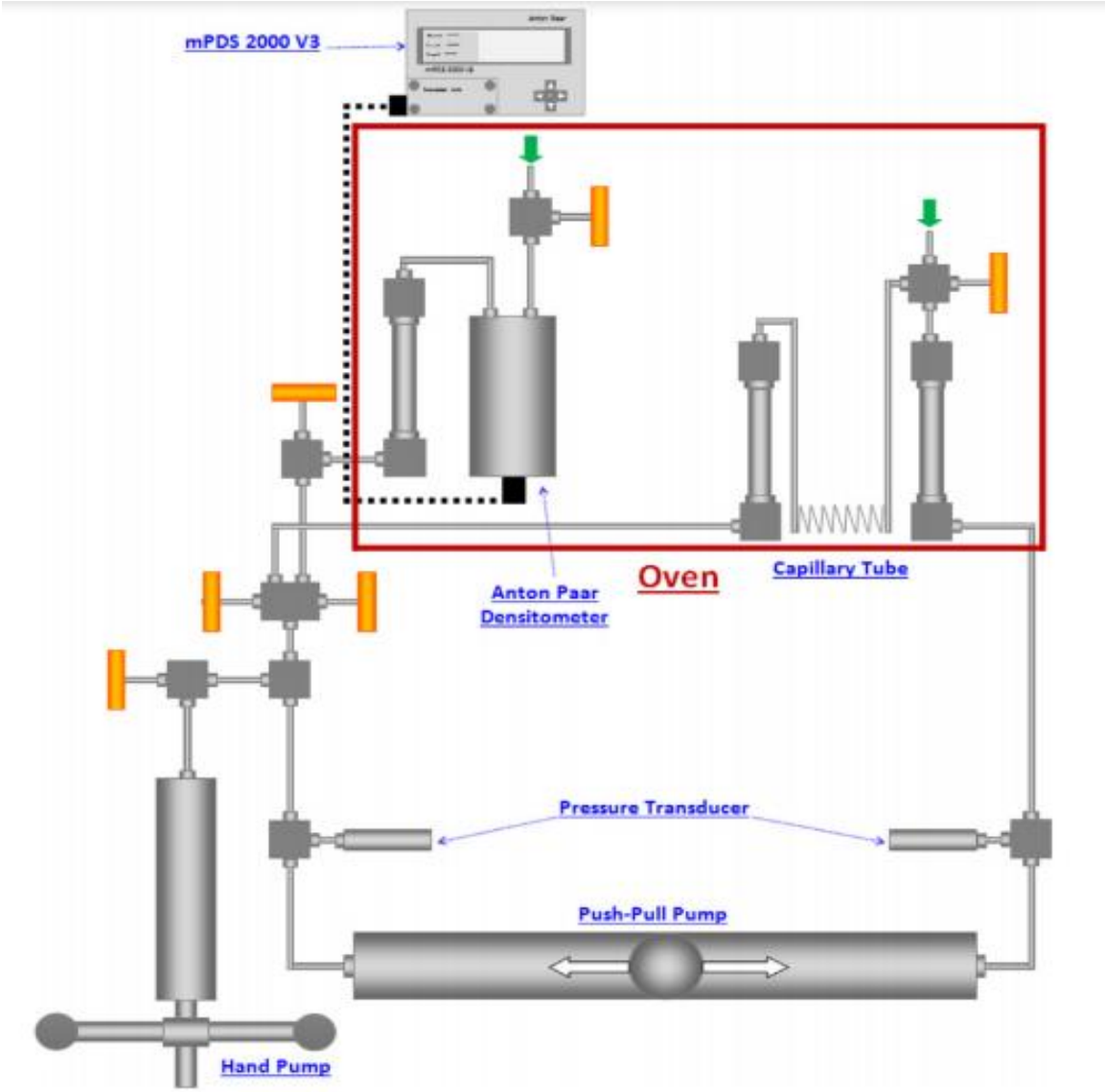

Figure 11 "Schematic drawing of the viscosity-density set-up", (Ref.[5]).

The set-up (Figure 11) consists in two small cylinders, with volumes of 15 cm^3, connected to each other through a capillary tube with measured length of 14.781 m and a calculated internal diameter of 0.29478 mm. An oscillating U tube densitometer Anton Paar DMA-HPM is connected to the set-up. The measuring cell contains a U-shaped Hastelloy C-276 tube that is excited to vibrate at its characteristic frequency electronically. The DMA-HPM is connected to a mPDS 2000V3 evaluation unit which measures the period of oscillation with a resolution of seven significant digits. The temperature of the vibrating tube cell is measured by a built-in thermometer connected to the mPDS 2000V3 unit. Two three-way valves, one on top of the cylinders connected to capillary tube and one on top of the densitometer, are installed to inject the sample inside the cylinders, tube system and densitometer. The base sides of the two cylinders are connected to opposite sides of a push–pull, motor driven mercury pump. This pump can move the sample fluid forwards and backwards between the two cylinders. There is also a hand pump connected to the system to control the pressure of the entire fluid system by injection and withdrawal of mercury. Both the opposed piston pump and the hand pump are fitted with Mitutoyo linear transducers readable to 0.005 mm on Mitutoyo SD-D1E readouts. As a 1 mm movement represents 0.151 cm^3 displacement in both pumps, the readability is 0.000755 cm^3. Each of the two opposed piston pumps has a variable control with which the speed can be adjusted to a maximum of 5 cm^3/s. The rate can be set with an error margin of ±0.00003 cm^3/s (Ref.[5]).

2.1.2.2 Procedures

The capillary tube viscosity measurement method has been employed to measure the viscosity of CO_2 systems with impurities. In each test, the set-up was loaded with the sample mixtures through the injection point on top of the densitometer after vacuuming the entire system. After disconnecting the sample cylinder from the system, the sample fluid was pushed through the capillary tube into the other cylinder using the push–pull mercury pump. The temperature of the system was set to the desired condition and the desired pressure was set using the hand pump. Once conditions had stabilized after isolating the densitometer by closing the related valve, the sample was pumped through the capillary tube at a number of different flow rates. To ensure consistency of the measurements, at each pressure, viscosities were determined at two or three different flow rates and at each flow rate three readings were logged. Consequently, the reported viscosity data in this study are an average of at least six to nine separate readings (with deviation typically lower than 1%). Pumping the sample fluid through the capillary tube by the piston pump resulted in a dynamic differential pressure that was monitored and recorded until stable. The pump was then stopped to record the static differential pressure. The difference between the dynamic and static differential pressures was used as the pressure drop across the tube. To ensure laminar flow conditions, Reynolds numbers were checked for the flow rates in which the measurements were performed. The Poiseuille equation can relate the pressure drop across the capillary tube to the viscosity, tube characteristics and also volumetric flow rate for laminar flow:

$$\Delta P = \frac{128LQ\eta}{C\pi D^4} \quad (1)$$

Where:

• ΔP: is the differential pressure across the capillary tube viscometer in psi;

• Q: represents flow rate in $\frac{cm^3}{s}$;

• L: is the length of the capillary tube in cm;

• D: refers to internal diameter of the capillary tube (0.029478 cm);

• η: represents the viscosity of the fluid in cP;

• C: is the unit of conversion factor equal to 6,894,757 if the above units are used.

The viscosity measurement results sufficiently accurate because, even if the tube length changes with the temperature, this has no noticeable influence on viscosity, as long as the flow is laminar. Only differential pressure as a variable in the above formulation can cause error in the viscosity measurement. The usual variation in differential pressure measurement is 0.01 psi and this leads to ±1% error in the calculated viscosity for those measured in this study. Density measurements were performed when the temperature of the vibrating tube became stable. Once the system conditions had stabilized, the oscillation period of the U-tube was determined from the interface mPDS 2000V3 evaluation unit. The measurement of density with a vibrating tube densitometer is not absolute, thus, the raw data (period of oscillation) were further treated to obtain the densities. The relationship between them is:

$$\rho(T,P) = A(T,P)\tau^2(T,P) - B(T,P) \quad (2)$$

Where:

• $\rho(T,P)$: sample density at temperature T and pressure P;

• $\tau(T,P)$: period of oscillation at temperature T and pressure P;

• $A(T,P)$ and $B(T,P)$: apparatus parameters depending on temperature and pressure, they must be determined from calibration measurements.

In our calibration, pure CO_2 is used as a reference substance at two different pressures (the lowest and the highest desired pressures in the system at the same temperature) in gas, liquid and supercritical phases. The apparatus parameters were defined as follows:

$$A(T,P) = \frac{\rho(T,P_1) - \rho(T,P_2)}{\tau^2(T,P_1) - \tau^2(T,\ P_2)} \quad (3)$$

$$B(T,P) = \frac{\tau^2(T,P_2)\rho(T,P_1) - \tau^2(T,P_1)\rho(T,P_2)}{\tau^2(T,P_1) - \tau^2(T,P_2)} \quad (4)$$

2.1.2.3 Density calculation

In this part of the work (Ref.[5]), the molar volume for CO_2 or a CO_2-rich mixture calculated by the SRK-EoS (Equation of State) is corrected using the exact volume of pure CO_2 at the given T and P.

$$V^{new} = V^{EoS} - V^{C} \quad (5)$$

Where:

• V^{EoS}: molar volume obtained from the equation of state;

• V^{C}: correction of molar volume.

The correction of molar volume is defined as: $V^{C} = \sum_{=1}^{N} x_i V_i^{C}$ (6)

Where:

• x_i : composition of the component I in the phase in which the volume is calculated.

For CO_2, V_i^{C} is defined by: $V_{CO2}^{C} = V_{Pure\ CO2}^{EoS} - V^{MBWR}$

The carbon dioxide density is computed from the MBWR equation (Modified Benedict-Webb-Rubin equation):

$$P = \sum_{n=1}^{9} a_n(T)\rho^n + \sum_{n=10}^{15} a_n(T)\rho^{2n-17} e^{-\gamma\rho^2} \quad (7)$$

2.1.2.4 Viscosity mathematical model

According to the corresponding states principles applied to viscosity (Ref.[5]), $\eta = \eta(T, P)/\eta_C$, for two components at the same reduced pressure, $P_{r=}P/P_C$ and reduced temperature, $T_r = T/T_C$, will be the same.

$$\eta_r = f(T_r, P_r) \quad (8)$$

Based on the dilute gases considerations and kinetic theory, viscosity at critical point can be approximated as:

$$\eta_C \approx \frac{P_C^{2/3} M^{1/2}}{T_C^{1/6}} \quad (9)$$

Where:

• M: molecular wight.

Thus, the reduced viscosity can be expressed as:

$$\eta_r = \frac{\eta(T,P)}{\eta_C} = \frac{\eta(T,P)T_C^{1/6}}{P_C^{2/3}M^{1/2}} \quad (10)$$

If the function f [Eq. (8)] is known, it is possible to calculate the viscosity of any other component, such as component I, at any pressure and temperature. Thus,

$$\eta_i = \frac{(P_{C,i}/P_{C,0})^{2/3}\,(M_i/M_0)^{1/2}}{\left(T_{C,i}/T_{C,0}\right)^{1/6}}\eta_0(TT_{C0}/T_{C,i}\,, PP_{C0}/P_{C,i}) \quad (11)$$

Where:

• 0: refers to the reference component.

The viscosity of CO_2 as a function of density and temperature can be calculated from the following equation:

$$\eta(\rho,T) = \eta_0(T) + \Delta\eta(\rho,T) \quad (12)$$

Where:

• $\eta_0(T)$: zero-density viscosity.

$\eta_0(T)$ can be obtained from the following equation:

$$\eta(T) = \frac{1.00697T^{1/2}}{\psi_\eta^*(T^*)} \quad (13)$$

In this equation, the zero-density viscosity is in units of Pa S and temperature, T, in K. The reduced effective cross section, $\psi_\eta^*(T^*)$ is represented by the empirical equation:

$$ln\psi_\eta^*(T^*) = \sum_{i=0}^{4} a_i\,(lnT^*)^i \quad (14)$$

where the reduced temperature, T^*, is given by:

$$T^* = \frac{kT}{e} \quad (15)$$

Finally, the expression to calculate the viscosity of mixtures at any pressure and temperature is:

$$\eta_{mix} = \frac{(P_{C,mix}/P_{C,0})^{2/3}\,(M_{mix}/M_0)^{1/2}}{(T_{C,mix}/T_{C,0})^{1/6}}\,\frac{\alpha_{mix}}{\alpha_0}\eta_0(T_0,P_0) \quad (16)$$

Where:

$$P_0 = \frac{PP_{C0}}{P_{C,mix}}\frac{\alpha_0}{\alpha_{mix}} \quad (17)$$

$$T_0 = \frac{TT_{C0}}{T_{C,mix}}\frac{\alpha_0}{\alpha_{mix}} \quad (18)$$

$$T_{C,mix} = \frac{\sum_j^N \sum_j^N z_i z_j [(T_{C,i}/P_{C,i})^{1/3} + (T_{C,j}/P_{C,j})^{1/3}]^3 \sqrt{T_{C,i}T_{C,j}}}{\sum_j^N \sum_j^N z_i z_j [(T_{C,i}/P_{C,i})^{1/3} + (T_{C,j}/P_{C,j})^{1/3}]^3} \quad (19)$$

$$P_{C,mix} = \frac{8\sum_j^N \sum_j^N z_i z_j [(T_{C,i}/P_{C,i})^{1/3} + (T_{C,j}/P_{C,j})^{1/3}]^3 \sqrt{T_{C,i}T_{C,j}}}{(\sum_j^N \sum_j^N z_i z_j [(T_{C,i}/P_{C,i})^{1/3} + (T_{C,j}/P_{C,j})^{1/3}]^3\ )^2} \quad (20)$$

The mixture molecular weight is found from:

$$M_{mix} = 1.304\ x\ 10^{-4}(M_w^{2.303} - M_n^{2.303}) + M_n \quad (21)$$

Where M_w and $M_n$are the weight average and number average molecular weights, respectively:

$$M_w = \frac{\sum_i^N z_i M_i^2}{\sum_i^N z_i M_i} \quad (22)$$

$$M_n = \sum_i^N z_i M_i \quad (23)$$

The parameter α for mixtures in Eq. (17) and (18) can be found from:

$$\alpha_{mix} = 1.000 + 7.378\ x\ 10^{-3}\rho_r^{1.847} M_{mix}^{0.5173} \quad (24)$$

Finally, the reduced density, ρ_r, is defined as:

$$\rho_r = \frac{\rho_{0((TT_{C0}/T_{C,mix}),\ (PP_{C0}/P_{C,mix}))}}{\rho_{C0}} \quad (25)$$

In summary:

I. Calculate the $T_{C,mix}$, $P_{C,mix}$ and M_{mix} from Eq.(19) ,(20) and (21), respectively.

II. Obtain the CO2 density at $PP_{C0}/P_{C,mix}$, $TT_{C0}/T_{C,mix}$ from the MBWR EOS and calculate the reduced density from Eq. (25).

III. The mixture parameter α_{mix} and α_0 should be calculated from Eq. (24).

IV. The reference pressure and temperature, P_0 and T_0, should be calculated from Eq. (17) and (18).

V. Calculate the CO2 reference fluid, $\eta_0(P_0, T_0)$ in Eq. (16) from Eq. (12).

VI. Calculate the mixture viscosity from Eq. (16).

2.1.2.5 Results about viscosity

The experimental and modelling results for the viscosity of the stream are plotted in Figure 12 and Figure 13.

All experiments for the stream were conducted at pressures above saturation or in the supercritical region and then at low pressures, i.e., in the single gas phase region. The viscosity of each conducted test was calculated using the modified Pedersen model.

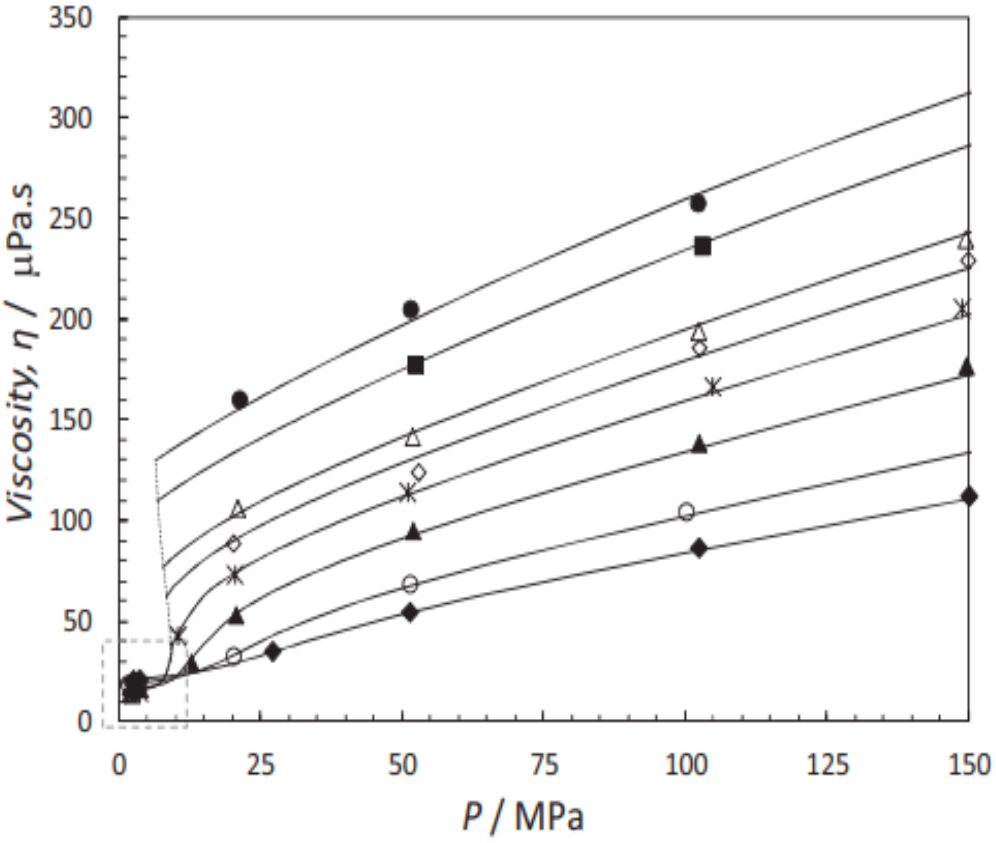

Figure 12 "Predicted and experimental viscosity of the multicomponent CO_2-rich stream", (Ref.[5]).

Key:

Black lines: Predictions using CSP model.

Black dotted lines: Predictions using CSP model at the bubble and dew pressures of the system. Data inside the grey box are plotted in Figure 13.

This work: (●)T = 243.15K, (■)T = 253.15K, (Δ)T = 273.15K, (◊)T = 283.15K, (*) T = 298.15K, (▲)T = 323.15K, (○)T = 373.15K, (♦)T = 423.15K.

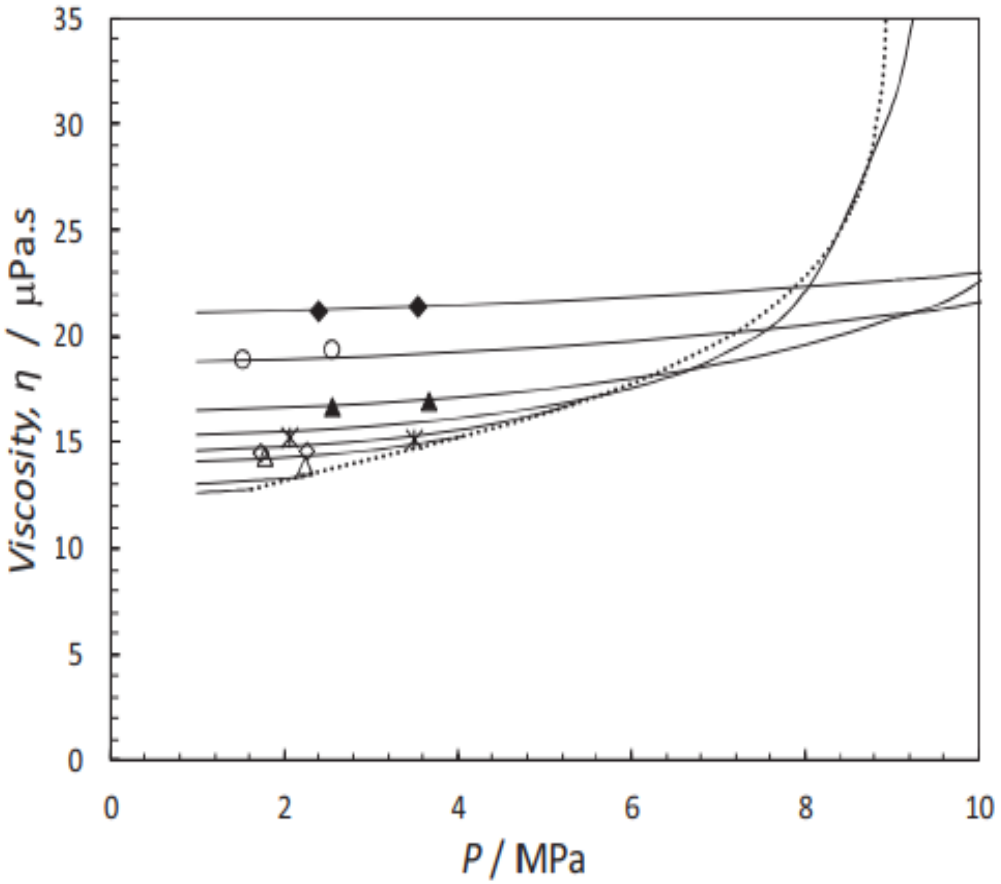

Figure 13"Predicted and experimental viscosity of the multicomponent CO_2-rich stream", (Ref.[5]).

Key:

Black lines: Predictions using CSP model.

Black dotted lines: Predictions using CSP model at the bubble and dew pressures of the system.

This work: (Δ)T = 273.15K, (◊)T = 283.15K, (*)T = 298.15K, (▲)T = 323.15K, (○)T = 373.15K, (♦)T = 423.15K.

As it can be seen from Figure 12 and Figure 13, the model predictions and experimental data are in good agreement. The absolute average deviation (AAD) is 1.7% (AAD is >30% if methane is used as a reference fluid). Both in the liquid and the supercritical regions, the viscosity is increasing with pressure and decreasing with temperature. In the vapour region, pressure has a weak effect on viscosity and the viscosity is increasing with temperature as expected for low pressure gaseous systems.

2.1.2.6 Results about density

Densities of this multicomponent mixture with 10% impurity were measured at different pressures and temperatures in gas, liquid and supercritical regions. Both experimental and modelling results with and without density correction are plotted in Figure 14 and Figure 15. By employing density correction using SRK-EoS the absolute average deviation reduces from 5.4% to 1.7%.

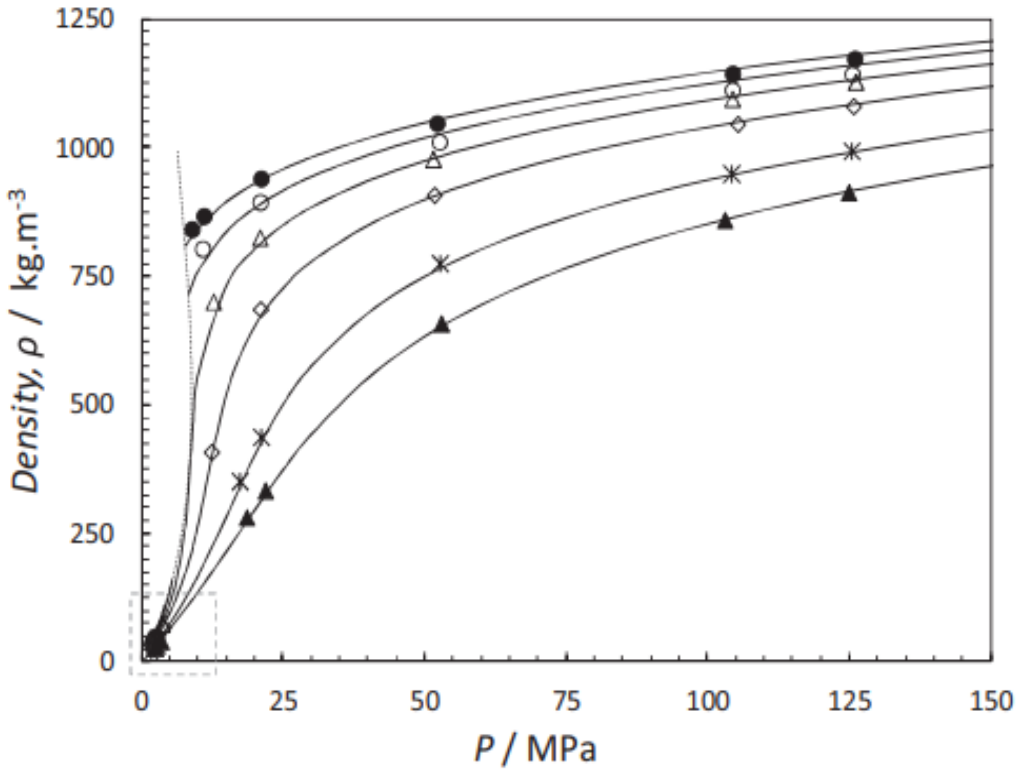

Figure 14 "Predicted and experimental density of the multicomponent CO_2-rich stream",(Ref.[5]).

Key:

Black lines: Predictions using the corrected SRK-EoS model.

Black dotted lines: Predictions using the corrected SRK-EoS model at the bubble and dew pressures of the system.

Data inside the grey box are plotted in Figure 15.

This work: (●)T = 273.26K, (○)T = 283.31K, (Δ)T = 298.39K, (◊)T = 323.48K, (*)T = 373.54K, (▲) T = 423.43K.

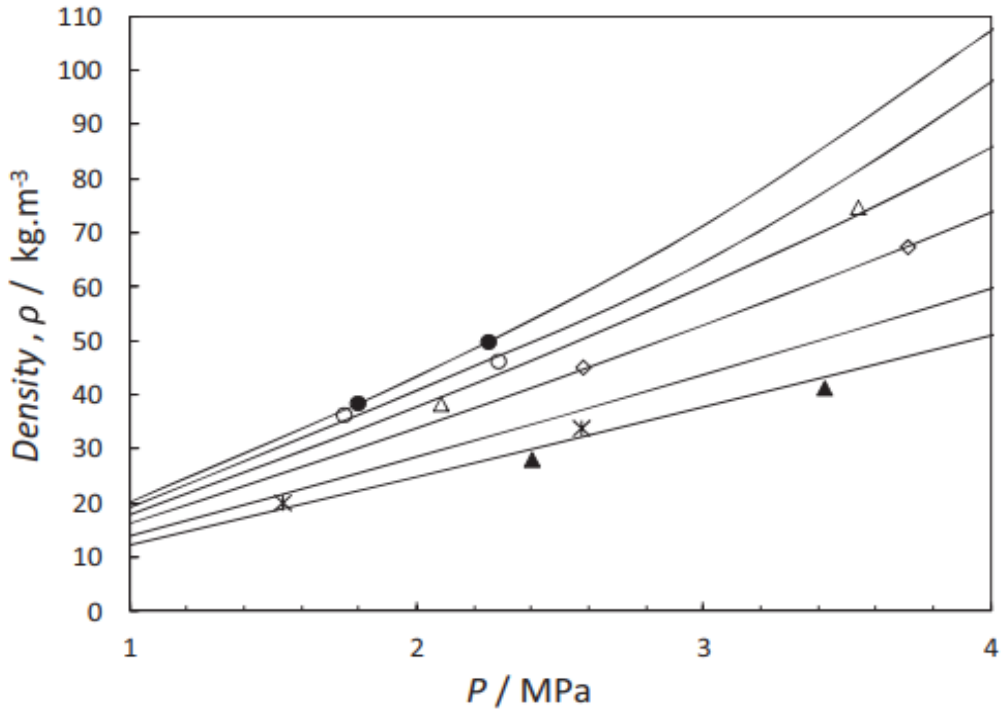

Figure 15"Predicted and experimental density of the multicomponent CO2-rich stream", (Ref.[5]).

Key:

Black lines: Predictions using the corrected SRK-EoS model.

This work: (●)T = 273.26K, (○)T = 283.31K, (Δ)T = 298.39K, (◊)T = 323.48K, (*)T = 373.54K, (▲)T = 423.43K.

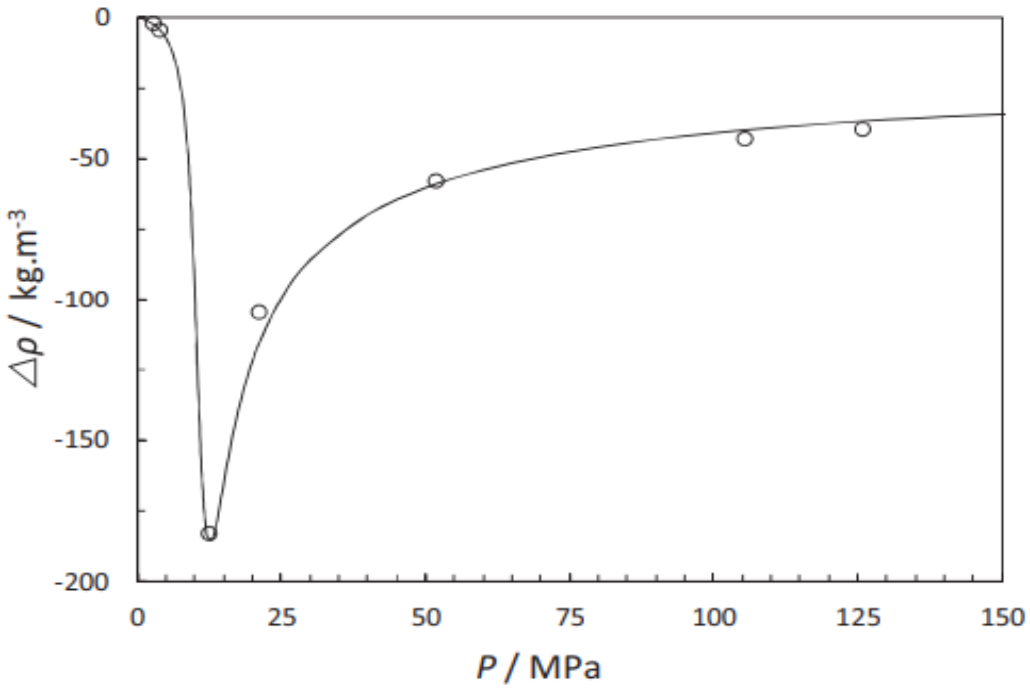

Figure 16"Predicted and experimental density difference, between the multicomponent CO2 density at 323.48 K.", (Ref.[5]).*

Key:

*: $\Delta\rho = \rho^{mix} - \rho^{CO2}$

Black lines: Predictions using the corrected SRK-EoS model.

This work: (○)T = 323.48K.

It is interesting to note the peculiar behaviour of the density at temperatures above the critical temperature compared to the density of pure CO_2 as shown in Figure 16 in which the difference between the density of the multicomponent mixture and pure CO_2 is plotted at 323.48K. For the CO_2 mixture at the stated temperature (323.48K), a maximum reduction in density from that of pure CO_2 occurs at a certain pressure. The maximum reduction is 180 kg/m^3 at a pressure around 12 Mpa, i.e., a 35% reduction. Ultimately, we will see that the density of the stream can be as much as 35% lower at the same temperature and pressure than pure CO_2, which can have a significant impact on transportation (pumping) costs.

2.1.3 Case study 2 – Simulation of the impact of impurities on CO_2 thermodynamic properties

This case study is based on a recent scientific article (Ref.[6]) concerning a process simulation of impurities to evaluate their impact on CO_2 properties.

The simulation was made using two programs:

• Apem HSYS, a chemical process simulator, was used to simulate pressure, temperature, phase envelope, density, critical pressure/temperature and viscosity;

• gPROMS, a general process model builder, was used to simulate pressure, temperature, density and viscosity.

Subsequently, Peng e Robinson (PR) equation of state was used in both the Aspen HYSYS and gPROMS analysis to calculate thermodynamic properties of CO_2 mixtures.

2.1.3.1 Impact on viscosity

Viscosity of a gas plays a role in the pressure loss calculation of CO_2 pipelines by opposing or resisting the flow. The Reynold's number used in the determination of the friction factor is a function of fluid viscosity. Temperature, pressure and composition strongly affect viscosity, an intensive property of fluids. Viscosity of CO_2 at temperatures slightly above the critical value shows nonlinearity, so a complex equation of state is recommended (McCollum and Ogden, 2006). Viscosity changes may be non-linear within the range of pressure and temperature of CO_2 pipeline transportation. Viscosity reduces with increase in temperature at high densities but increases with increase in temperature at low densities (Zabaloy et al., 2005). The viscosity of 99.44-mol % CO_2 and 0.56- mol % pentaerythritol tetra-2-ethylhexanoate (PEB3) measured at pressures between 10 and 60 Mpa decreased with increase in temperature (Pensado et al., 2008). Since density is high at supercritical pressures, usually greater than 10 Mpa in CO_2 pipelines, viscosity will increase with decrease in temperature. However, this behaviour was not readily verified in the simulated pipelines because both pressure and temperature decrease at the same time along the pipeline. The effect of impurities on the viscosity of CO_2 is shown Figure 17 in 10-mol % N_2 has the highest reduction in the viscosity while 6.5- mol % H_2O has the highest increase in viscosity. A reduction in viscosity reduces the friction between fluid molecules and allows the fluid to flow more freely. Higher pressure losses are expected with fluids with higher viscosity. Therefore, SO_2, H_2S and H_2O had a negative impact on the ease of fluid flow (Ref.[6]).

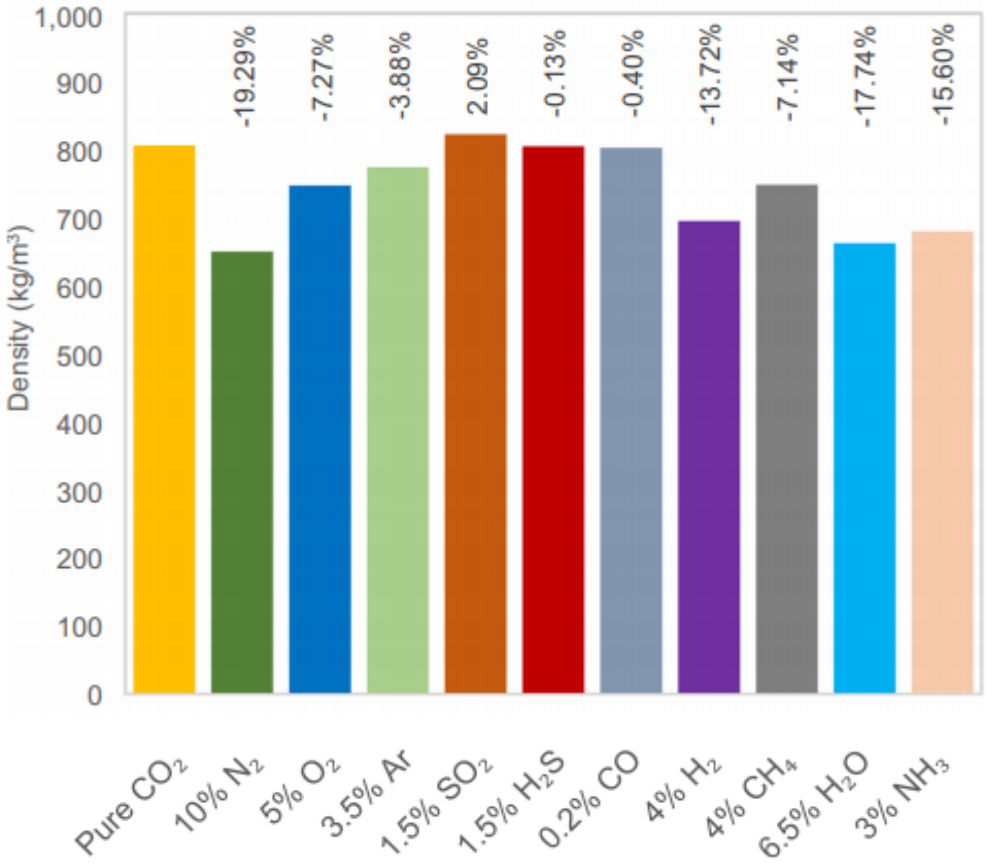

Figure 17 "Densities of CO_2 binary mixtures and percentage deviation from pure CO_2", (Ref.[6]).

2.1.3.2 Impact on pressure

Pressure changes in fluids flowing in pipelines are dependent on density, viscosity and velocity among other minor effects. At equal mass flow rates, lighter fluids result in higher pressure losses than denser fluids in horizontal pipes. This is due to increase in velocity in the pipeline for lighter fluids. For non-horizontal pipelines, the effect of density may outweigh the effect of velocity due to the elevation component. A high-density fluid will result in higher pressure losses in inclined pipelines but may result in lower pressure losses in horizontal pipelines and higher pressure gains in declined pipelines. Equation (26) presents frictional and elevation components of the common pressure drop equation. The acceleration component of pressure drop is usually ignored in the calculation of pressure losses.

$$\Delta P = \frac{fDlv^2}{2D} + \rho g \Delta z \quad (26)$$

Where:

• ΔP : pressure drop [Pa];

• f : friction factor;

• l : length [m];

• v : velocity $[m/s]$;

• D : pipeline internal diameter [m];

• ρ : fluid density $[Kg/m^3]$;

• g : acceleration due to gravity $[m/s^2]$;

• Δz : change in elevation [m].

In horizontal pipelines, gases lighter than CO_2 increase the pressure losses while denser gases reduce the pressure losses. This effect is due to the fact that a higher volume of lighter gases is required to make up the same mass flow, which consequently increases the velocity of fluid flow. This increased velocity when squared [see Equation (26)] outweighs the reduced density. The loss of pressure during flow determines the length of flow before recompression is required and may increase the cost of pipelines. The cost of CO_2 pipelines increases when there are high pressure losses resulting to higher capital cost (installation of more boosting stations) and higher operational cost in running the increased number of boosting stations. The analysis of the cost impact of impurities is the subject of our future work. Flowing pressures and pressure loss are the most important flow parameters in CO_2 pipeline design. Therefore, pipelines are designed to avoid high pressure losses. However, pipelines running downhill may increase in pressure. The increase in pressure may affect pipeline joints/seals, cause pipeline wall erosion, leakages, or necessitate the installation of pressure reducing stations. Only SO_2 and H_2O impurities resulted to lower pressure losses than pure CO_2 in horizontal pipelines. It means that in horizontal pipelines, CO_2 fluids with these impurities will flow for longer distances before recompression is required, thereby reducing the cost of transportation. The percentage change in horizontal pipes was at least at 0.9% with 3-mol % NH_3 while the largest change was 25.01% with N_2. 10-mol % N_2 also resulted to the highest pressure loss of 2.04 Mpa while 6.5-mol % H_2O resulted to the lowest pressure loss of 1.54 Mpa. A single impurity of 6.5-mol % H_2O would enable the fluid flow for 5.8% longer distance while 1.5-mol % SO_2 would enable the fluid travel 2.3% longer distance compared to pure CO_2 before recompression. Conversely, 10-mol % N_2 will cause the fluid to travel only 80% of the distance a pure CO_2 fluid would travel in the pipeline before requiring recompression. The effect of impurities on pressure also depends on pipeline profile. Impurities in pipelines at inclined positive angles tend to have reduced effects. The maximum impact resulting from 10-mol % N_2 in pressure change for the inclined pipeline is 5.62%, for horizontal pipeline is 25.01% and for the downhill pipeline is 55.46%. Impurities heavier than CO_2 increase pressure losses in the uphill pipeline and increase pressure gain in the downhill pipeline.

H_2O had the highest pressure loss in the inclined pipeline and highest pressure gain in the declined pipeline. In the inclined pipeline, 10-mol % N_2 had the highest positive change, reducing the pressure loss by about 0.29 Mpa. In the declined pipeline, (assuming that pressure gain is also not desirable), 10-mol % N_2 had the greatest positive change by reducing the pressure gain by about 1.1 Mpa while H_2O increased the pressure gain by about 0.32 Mpa. Overall, 1.5-mol % H_2S had the least impact, changing the pressure behaviour from that of pure CO_2 by about 0.03%, 0.49% and 0.30% on the uphill, horizontal and downhill pipelines, respectively. The pressure changes in the three pipeline profiles are shown in Figure 18 and the percentage change from the pressure drop of pure CO_2 is shown in Table 3. Negative values in Table 3 indicate a reduction in pressure loss and in the case of a downhill pipeline, a reduction in pressure gain. Any impurity that reduces pressure increase or pressure decrease has a positive impact. The negative values (bars) in Figure 18 indicate pressure gain. Table 4 shows the minimum dip (negative) angles for this pipeline to gain in pressure. All fluids including pure CO_2 increased in pressure along the downhill pipeline. Downhill pipelines with binary CO_2 fluids at the maximum specified mol % of impurities flowing in a pipeline with the assumed specifications at angles to the horizontal greater than the values shown will increase in pressure along the direction of flow. Increases in CO_2 fluid pressure during flow of fluids in pipelines is also not desirable because pressure reducing stations may be required be control the pressure. A minimal pressure loss along the length of pipelines transporting CO_2 fluids is desired (Ref.[6]).

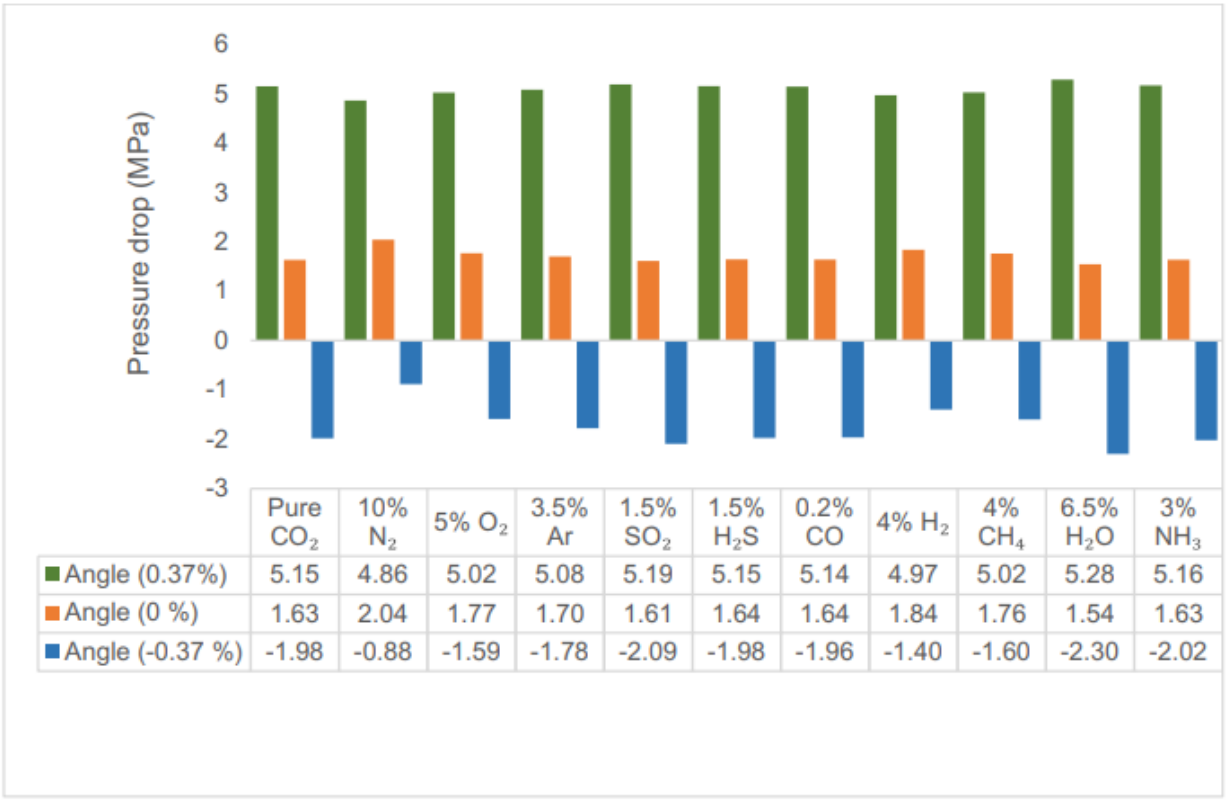

	Pure CO_2	10% N_2	5% O_2	3.5% Ar	1.5% SO_2	1.5% H_2S	0.2% CO	4% H_2	4% CH_4	6.5% H_2O	3% NH_3
Angle (0.37%)	5.15	4.86	5.02	5.08	5.19	5.15	5.14	4.97	5.02	5.28	5.16
Angle (0 %)	1.63	2.04	1.77	1.70	1.61	1.64	1.64	1.84	1.76	1.54	1.63
Angle (-0.37 %)	-1.98	-0.88	-1.59	-1.78	-2.09	-1.98	-1.96	-1.40	-1.60	-2.30	-2.02

Figure 18 "Pressure drop of CO_2 binary fluids in uphill, horizontal and downhill pipelines", (Ref.[6]).

Angle of inclination	+ 0.37^0	0°	- 0.37°
10% N_2	−5.62	25.01	−55.46
5% O_2	−2.53	8.15	−19.82
3.5% Ar	−1.38	4.12	−10.38
1.5% SO_2	0.77	−1.34	5.50
1.5% H_2S	0.03	0.49	−0.30
0.2% CO	−0.13	0.38	−0.97
4% H_2	−3.54	12.36	−29.50
4% CH_4	−2.42	7.83	−19.33
6.5% H_2O	2.63	−5.45	15.89
3% NH_3	0.31	0.09	1.83

Table 3"Percentage change of pressure drop of uphill, horizontal and downhill pipelines", (Ref.[6]).

Impurity	Pure CO_2	6.5% H_2O	3% NH_3	1.5% SO_2	0.2% CO	1.5% H_2S	3.5% Ar	4% CH_4	5% O_2	4% H_2	10% N_2
Dip Angle (degrees)	0.17	0.15	0.25	0.16	0.17	0.17	0.18	0.19	0.20	0.23	0.26

Table 4 "Minimum dip angle (to the horizontal) of pipeline to gain pressure", (Ref.[6]).

2.1.3.3 Impact on temperature

As CO_2 flows in the pipeline, heat is transferred from the flowing fluid to the soil or surrounding area. Heat transfer out of the pipeline occurs in three steps: convective heat transfer between the fluid and the inner pipeline wall, the heat conduction from the inner pipeline wall to the outer pipeline wall and the heat emission to the surrounding area. The maximum temperature of CO_2 fluids is reached immediately after exiting the compressor. This heat is transferred to the environment as the fluid flows in the pipeline. Fluid temperature is not a limiting factor in CO_2 pipeline design because the fluid stays in the dense phase as long as the pressure is above the critical value. During depressurisation, heat may be transferred from the surrounding area to the pipeline since the CO_2 cools due to vaporisation and the Joule-Thompson effect. This reverse heat transfer may occur only during start-up or shut down for a short period or during a leak. CO_2 pipelines may be pressured with N_2 at start-up before introducing the CO_2 fluid into the pipeline to avoid the cooling effect of expanding fluid. The bulk of heat transfer is from the flowing fluid, which increases in heat after compression, to the surrounding area. The temperatures of binary components at the maximum allowable impurity concentration from the pipeline inlet to the outlet were studied. Figure 19 shows the temperature drop of each binary mixture flowing in a horizontal pipeline and the percentage change from that of pure CO_2. 6.5-mol % H_2O content reduced the temperature loss by a maximum of 25.5% and 10-mol % N_2 increased the temperature drop by a maximum of 87.2%. A low temperature is desired because it results in increased volume transported due to increased density and lower pressure loss in CO_2 pipelines, it therefore implies that impurities increasing heat loss have a positive effect.

Pipelines do not need to be insulated (except to protect them from external corrosion) to enable rapid heat loss, which may result in reduced pressure loss. The greatest heat loss (4.03 °C) was due to 10-mol % N_2, increasing the heat loss by about 87.19%. Heat loss has a positive effect because it will result in a denser fluid and consequently in lower pressure losses. The lowest heat loss (1.60 °C) was due to 6.5-mol % H_2O reducing the heat loss by about 25.51% less heat loss compared to pure CO_2. 1.5-mol % H_2S had a negligible change on temperature variation at 0.11% (Ref.[6]).

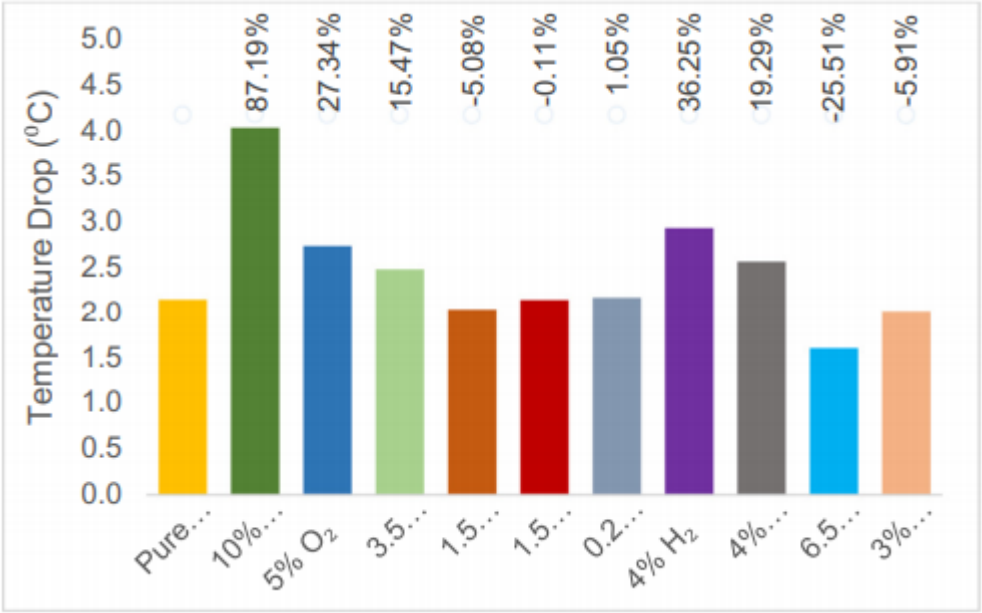

Figure 19 "Temperature drop of binary mixtures with percentage deviation from pure CO_2", (Ref.[6]).

2.1.3.4 Impact on critical pressure and temperature

To keep the fluid in a supercritical state, the temperature and pressure must be above the critical values. To achieve this, the fluid is compressed and the pipeline heated or insulated to reduce the heat transfer from pipeline to the surrounding area. Fluid compression and heating, where it is applied, are costly. Lower critical pressures require less compression and consequently less energy cost. All impurities increased the critical pressure above that of pure CO_2. An increase in critical pressure may increase the minimum pipeline pressure, which in turn increases the cost of operation of CO_2 pipelines. The cost of energy of compression increases along with the increase in critical pressure. 10-mol % N_2 has the highest critical pressure while 1.5-mol % H_2S has the lowest value. At equal mol %, H_2 has the highest critical pressure while H_2S has the lowest critical pressure. The minimum pressure of a CO_2 pipeline is stipulated to be slightly above the critical pressure. Minimum pressures are chosen slightly above (about 10% higher than) the critical pressure. Impurities that cause increases in critical pressure may result to an increase in the cost of fluid transportation, as more compression energy is required to compress the gas to supercritical condition. All impurities increased the critical pressure with N_2 having the highest increase at more than 19.6% while H_2S increased it by just 0.11%.

Three impurities, SO_2, H_2S and NH_3, increased the critical temperature while all others decreased the critical temperature. The temperature range for supercritical flow decreases with the increase in critical temperature. However, temperatures within the operational range of CO_2 pipeline pressures are not an issue. An increased critical temperature may result in lower pressure losses when the flowing fluid temperature decreases below the critical value and enters the subcritical state or liquid state. CO_2 fluids at subcritical or liquid state result to increased density and lower pressure losses. Therefore, an increase in critical temperature has a positive impact if supercritical flow is not a requirement. 10-mol % N_2 resulted to the lowest critical temperature of 23.61 °C representing 23.72% lower than pure CO_2 and 3-mol % NH_3 impurity resulted to the highest critical temperature of 34.26 °C, about 10.7% higher than that of pure CO_2. A high critical temperature may be desired to ensure that the fluid stays in the dense subcritical state rather than the supercritical state. However, where supercritical flow is specified, a lower critical temperature is desired to avoid heating the fluid to reach supercritical state. Table 5 shows the critical pressure and critical temperature of the CO_2 fluids (Ref.[6]).

Impurity	Pure CO_2	10% N_2	4% CH_4	3.5% Ar	1.5% SO_2	1.5% H_2S	5% O_2	4% H_2	0.2% CO	3% NH_3
P_c (MPa)	7.37	8.82	7.99	7.71	7.56	7.38	7.40	7.86	7.60	7.57
T_c (^{0}C)	30.9	23.6	27.8	28.8	34.0	31.2	30.8	28.5	28.0	34.3

Table 5 "Critical pressure and temperature of CO2 fluids", (Ref.[6]).

2.1.3.5 Final results

This research turns out to be quite "innovative" because the impact of each impurity on the transportation of CO_2 in pipelines at the maximum allowable concentrations has not been investigated before. From this work, it has been shown that at the specified maximum concentration of impurities, N_2 has the worst impact followed by hydrogen. 10-mol % N_2 increased the pressure loss by 25.0%, heat loss by 87.2%, critical pressure by 19.6%; and reduced the critical temperature by 23.7%, density by 19.4% and viscosity by 12.9%. H_2S has the smallest impact closely followed by CO on the transportation of CO2 fluids. 1.5-mol % H_2S increased the pressure loss by 0.5%, critical pressure by 0.1%, critical temperature by 0.9%, viscosity by 4.4%; and reduced the heat loss and density by 0.1%. Though allowable concentrations of the impurities also depend on the specifications for CO_2 storage or usage, the findings here can be used to modify the maximum allowable concentrations for each impurity and help in sensitivity analysis of CO_2 pipelines. For example, the permitted concentration of N_2 could be reduced because it has a high impact on the transport properties. The impact of H_2S is small, so a higher concentration may be allowed to save the cost of purifying the stream to a very low concentration. This work can serve as a guide during the design of CO_2 pipelines because it shows both the negative and positive parameters affected by each impurity. A pipeline designed to transport pure CO_2 may be overdesigned for CO_2 fluids with impurities having positive impact but under designed for impurities having negative impact. It is advisable to design each parameter of CO_2 pipeline transportation with a knowledge of the impact of each impurity found in the fluid.

2.2 Main CO_2 pipeline transportation issues

As we have seen in the previous paragraphs, impurities can alter some thermodynamic parameters (viscosity, density, pressure, etc.) and these variations will inevitably impact on the structure designated for the transportation, the pipeline in this case. This section will thoroughly analyse the aspects concerning the effects on design and operation parameters during the transport process.

2.2.1 Foreword

Impurities affect the design of equipment like pumps and compressors (Ref.[4]). For example, if the suction pressure is lower than the vapor pressure, unwanted cavitation will occur in the pump. The compression strategy will also be affected by impurities. For example, one can choose to pressurize the CO_2 by compression and condense the CO_2 to liquid prior to further pressurization by pump, impurities have also an effect upon the design and operation of blow down facilities. If a combustible compound is present which is not allowed to be vented to atmosphere (e.g. H_2S) a possible solution is to connect the blow down facility to a flare (It should also be noted here that combusting H_2S produces SO_2 which is also highly toxic). This again implies that a fuel gas system needs to be incorporated in the design. In such a case, the CO_2 needs to be mingled with enough fuel so combustion can take place. The impurities have a high impact on the transport capacity. For example, CO_2 plus 5 % methane decreases the flow by 16 % (flow adjusted to have an 82.7 Pa/m pressure drop at 10 341 kPa and 16 °C in 406 mm pipeline). In addition, impurities take up space in the pipeline that otherwise is used for transporting CO_2. Compared to transporting pure CO_2, 5 vol% impurities will reduce the volume of CO_2 transported by 5%. Since CO_2 is transported as a dense fluid it will be relatively easy to compensate for losses of capacity by boosting the pressure using a pump, as long as the pipeline is not already operating close to Mean Allowable Operating Pressure (MAOP). A CO_2 mixture containing 3 mole% of hydrogen halves the minimum distance between recompression stations compared to pure CO_2. When recompression is not an option, with a given pressure loss along the pipeline route, the minimum entrance pressure will have to be raised when the vapor pressure of the fluid is higher due to the presence of impurities. This in turn can necessitate to design the pipeline for higher operating pressures leading to for example large pipe wall thickness or stronger materials. The impurities can also have an effect upon the pipeline integrity. The vapor pressure sets the decompression pressure at a pipeline break. Thus, a high decompression pressure can facilitate further propagation of a fracture. Presence of atomic hydrogen can lead to hydrogen embrittlement of the pipeline steel or hydrogen induced cracking. For atomic hydrogen to occur, free water needs to be present. The underlying mechanism is that atomic hydrogen diffuses into the metal matrix and combines again to hydrogen molecules. This creates local internal pressure which reduces the ductility and tensile strength of the steel. The atomic hydrogen may also embrittle the steel through its interference with the plastic flow during deformation. Carbon steels used for pipelines can be specified with additional requirements to remediate this potential problem. Measures can include lower sulphur contents of the steel, limiting the hardness and alloying of the steel. Presence of H_2S is another issue of concern. Even without the presence of free water H_2S poses a potential problem (with free water also atomic hydrogen is produced). A reaction between iron and H_2S will occur at the pipe inner surface, creating a thin surface of iron sulphide and atomic hydrogen. This is called Sulphide Stress Cracking (SSC). The sensitivity for this can be reduced by for example adding nickel to the steel alloy composition. For pipeline operations, the presence of H_2S implicates that the steel has to be specified for so-called ‘sour service’. The presence of Oxygen is considered problematic from a corrosion point of view, especially when free water is present. Finally, impurities can affect the water solubility and hydrate formation conditions (Ref.[4]).

2.2.2 Effects on pipeline integrity – Corrosion

The presence of a significant level of water in the CO_2 stream causes many problems in pipelines and injection wells and is probably the most important impurity to control. To avoid excessive corrosion and stress corrosion, water levels should be as low as possible to prevent corrosion or hydrate formation. CO_2 streams should be dried to levels below 350 ppm H_2O, (in some situations suggested to below 50 ppm) to prevent significant corrosion. Water concentrations should be below 250 ppm to ensure no hydrate formation (above 70bar and -30°C). Hydrogen and H_2S levels should each be kept to below 100 ppmm if there is significant (>1000ppmm) moisture in the pipeline / injection systems (Ref.[7]).

2.2.2.1 Case Study 3 – Corrosion evaluation of packer rubber materials

Before corrosion test (Ref.[8]), the tensile properties and hardness of dumbbell-shaped samples of the three kinds of rubber materials in initial state were measured. The dumbbell-shaped samples and O-ring samples (marked every one) were separately put into gaseous phase and liquid phase of CO_2. And the simulated solution prepared was poured into the autoclave. And then the autoclave was sealed. Nitrogen gas was pumped into the vessel to displace oxygen for two hours. After that, it was heated to test temperature and a special pump was used to charge the autoclave CO_2 continuously. At last, the pressure in autoclave was pressurized to test required value and kept for 7 days. After the test, the pressure and temperature were released, and the samples were gotten out from the autoclave. And then the tensile mechanical properties and hardness of specimens were measured and their morphology after corrosion were analysed.The tensile mechanical properties were tested according to standard GB/T 528–2009 on the dumbbell-shaped samples in order to obtain accurate results. The elongation at break and tensile strength of rubber samples in initial state, the gaseous phase and the liquid phase of CO_2 were shown in Table 6, Figure 20 and Figure 21, respectively. As it can be seen from Table 6, Figure 20 and Figure 21, the elongation at break and tensile strength after corrosion in gaseous phase and liquid phase of CO_2 is lower than that in initial state. The elongation at break of NBR after being corroded in gaseous phase and liquid phase of CO_2 was reduced approximately by 17.68% and 42.90% of the original state, and the tensile strength after being corroded in gaseous phase and liquid phase of CO_2 was reduced approximately by 62.21% and 68.69%. The elongation at break of HNBR after being corroded in gaseous phase and liquid phase of CO_2 was reduced approximately by 38.68% and 66.98% of the original state, and the tensile strength after being corroded in gaseous phase and liquid phase of CO_2 was reduced approximately by 31.24% and 64.20%. The elongation at break of FKM after being corroded in gaseous phase and liquid phase of CO_2 was reduced approximately by 50.43% and 64.13% of the original state, and the tensile strength after being corroded in gaseous phase and liquid phase of CO_2 was reduced approximately by 24.36% and 40.83%. It is obvious that the tensile mechanical properties of rubber materials were weakened after corrosion by supercritical CO_2. Therefore, the influences of corrosion on mechanical properties of rubber materials should been taken fully into account in actual engineering design.

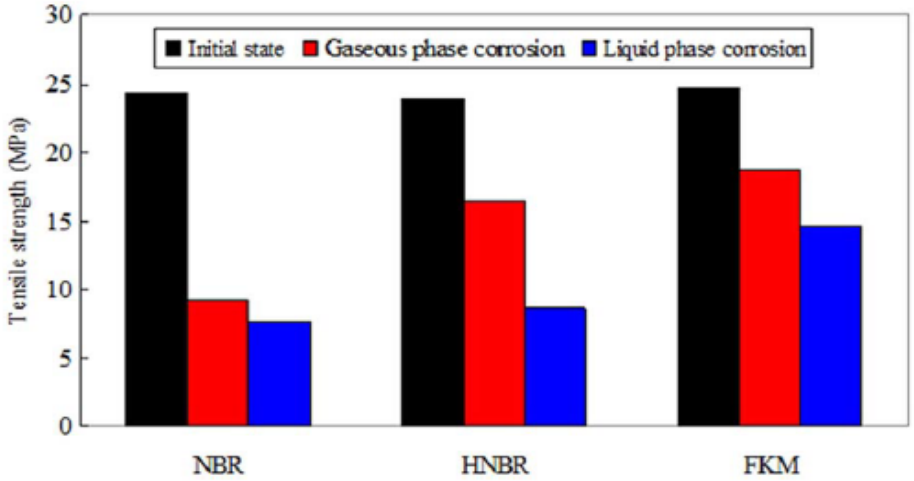

Figure 20"Comparison results of tensile strength", (Ref.[8]).

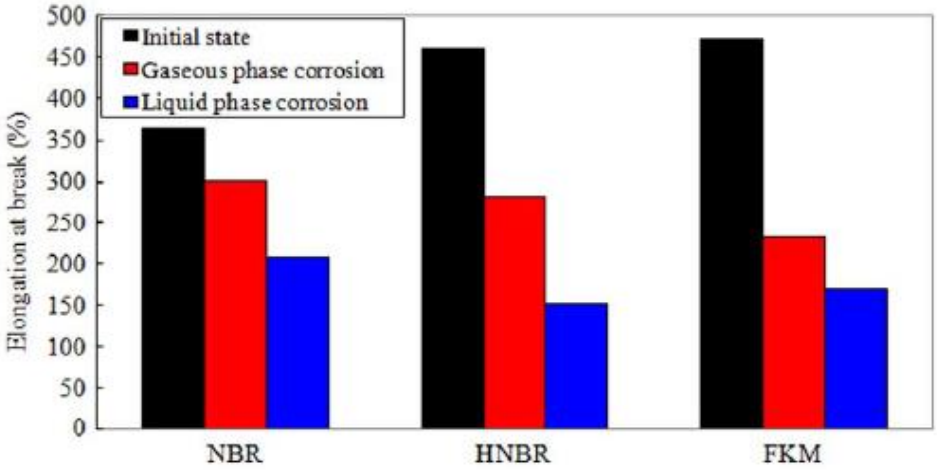

Figure 21"Comparison results of elongation at break", (Ref.[8]).

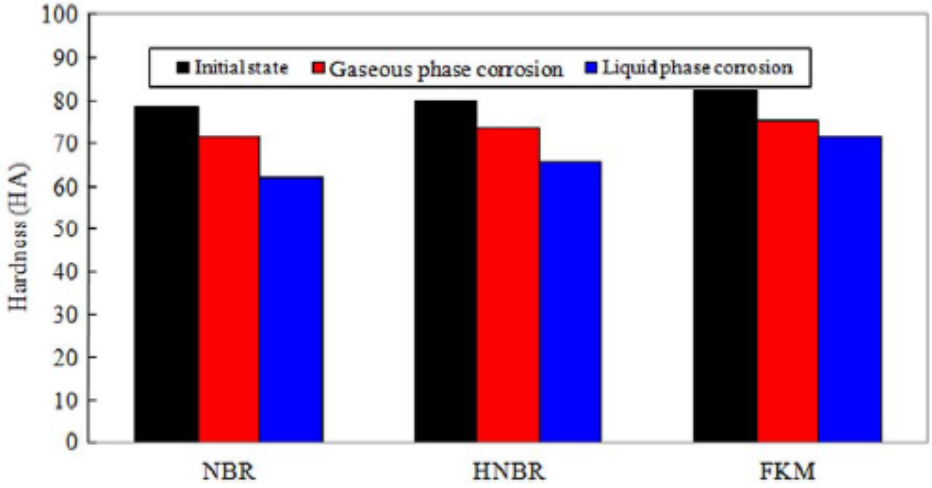

Figure 22"Comparison results of shore hardness before and after corrosion.", (Ref.[8]).

Rubber types	State	Tensile properties	
		Elongation at break (%)	Tensile strength (MPa)
NBR	Initial state	364.98	24.40
	Gaseous phase	300.46	9.22
	Liquid phase	208.40	7.64
HNBR	Initial state	460.03	23.91
	Gaseous phase	282.10	16.44
	Liquid phase	151.89	8.56
FKM	Initial state	472.08	24.71
	Gaseous phase	234.01	18.69
	Liquid phase	169.35	14.62

Table 6 "Tensile property results of dumb bell-shaped simples", (Ref.[8]).

Rubber types	State	Hardness (HA)
NBR	Initial state	78.62
	Gaseous phase	71.45
	Liquid phase	61.91
HNBR	Initial state	80.11
	Gaseous phase	73.68
	Liquid phase	65.76
FKM	Initial state	82.57
	Gaseous phase	75.42
	Liquid phase	71.38

Table 7 "Hardness results of dumb bell-shaped simples" (Ref.[8]).

From Table 7 and Figure 22 it can be seen that the shore hardness of rubber materials presented a decrease after corrosion both in gaseous phase and liquid phase of CO_2 as compared to that of samples in initial state. Corrosion in liquid phase of CO_2 was much more severe than that in gaseous phase environment. The shore hardness of three kinds of rubber materials corroded in liquid phase of CO_2 were reduced approximately by 21.25%, 17.91% and 13.55%. The hardness decrease of NBR was the largest, of which the corrosion resistance was the worst The effects of supercritical CO_2 attack on three kinds of rubber materials were studied under simulated downhole conditions in injection wells. The tensile mechanical properties of rubber materials were weakened after corrosion by supercritical CO_2. And the hardness also slightly reduced after corrosion.

Comparisons showed that rubber samples exposed to liquid CO_2 exhibited greater reactivity as compared to gaseous CO_2. Results showed that the corrosion resistance of FKM and HNBR was better than that of NBR. Bubbling, deformation and dissolution were typical forms for the failure of rubber materials. Therefore, actual working conditions and environments should be considered when selecting rubber materials for packers and suitable preventive measures should be adopted, eventually reducing risks and economic losses.

2.2.3 Combined effect of water and other impurities

In relation to the corrosion issues seen in the previous paragraph, an experience from the USA (Ref.[9]) showed that no corrosion problems have been reported in the part of the system that has been exposed to dry CO_2 only, corrosion has been reported in process systems where free water was present.

2.2.3.1 Presence of free-water

Corrosion rates of X65 steel exposed 150 to 300 hours at 40°C have been measured in water equilibrated with CO_2 at different pressures. As seen in Figure 2, the corrosion rate decreases with CO_2 pressure. The risk of forming aqueous phases during pipeline decompression should also be considered. Below the critical temperature, depressurizing the CO_2 to less than the critical pressure results in a two-phase gas/liquid system and impurities will partition between the two phases. The concentration of many impurities (H_2O, SO_2, NO_2) will increase in the remaining liquid CO_2 phase. If the water concentration in the liquid CO_2 phase exceeds the solubility, water will form a separate corrosive phase together with the other impurities. As the corrosion rate in free water can be very high, a strategy for handling accidental water ingress is required (Ref.[9]).

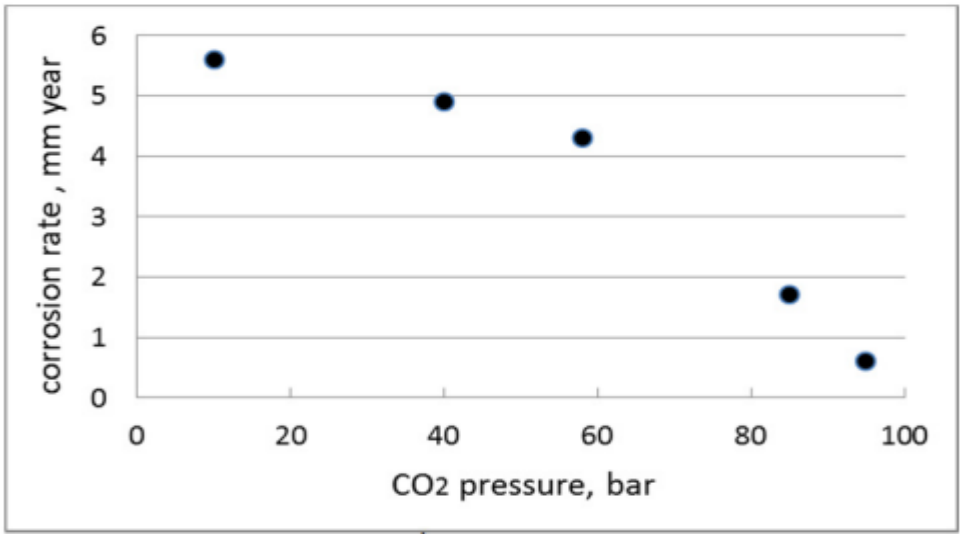

Figure 23 "The average corrosion rate measured by Seirstein during 150-300 hours exposure at 40 °C in water equilibrated with CO_2", (Ref.[9])

2.2.3.2 $CO_2 - H_2O - NO_2$ system

A limited number of papers report experimental data in the presence of flue gas impurities like Sox, Nox and O2. The corrosiveness of the CO2-H2O system increases considerably when NO2 is present. NO2 is highly soluble in water and reacts with water to produce nitric acid and NO under atmospheric conditions. The same type of reaction probably occurs in the dense phase CO2 system:

$$3NO_{2(g)} + H_2O_{(1)} = 2HNO_{3(aq)} + NO_{(g)}$$

As shown in Figure 24, a corrosion rate of 1.6 mm/year was measured in an IFE experiment performed with 1222 ppmv H2O and 478 ppmv NO2 and 0.7 mm/year in the experiments with 1222 ppmv H2O and 190 ppmv NO2. 35 The figure also shows results from experiments carried out with 488 ppmv water and the higher corrosion rate in the experiment with 96 ppmv NO2 compared to the experiment with 191 ppmv NO2 was attributed to the much shorter exposure time, 20 vs. 3 days. It was pointed out in this work that the measured corrosion rates probably would have been much higher if water and NO2 were replenished at the same rate as they were consumed.

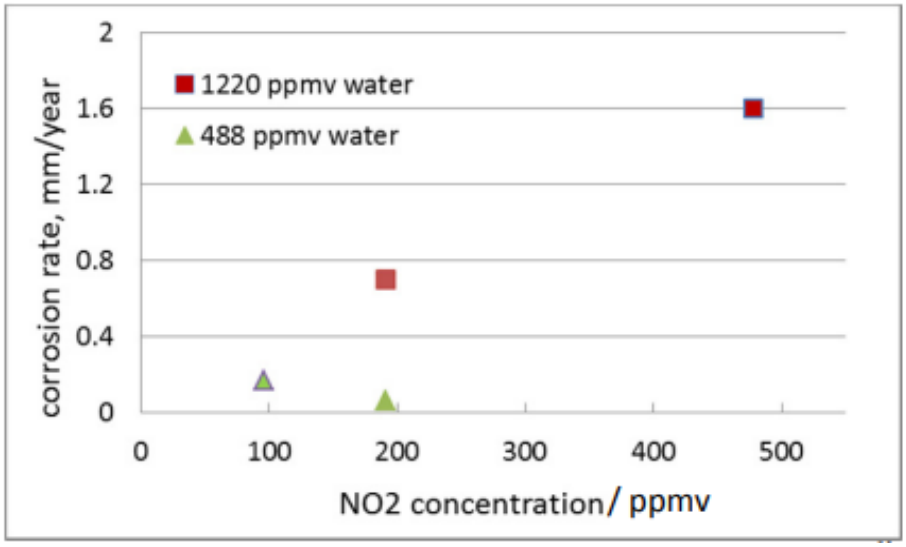

Figure 24 "Corrosion rates measured at IFE in system in CO2-H20-NO2 system at 100 bar and 25 °C ", (Ref.[9]).

In dense phase CO2 containing 1000 ppmv H2O, 4.7 vol% O2 and 100 ppmv NO. There is an extremely high corrosion rate, 11.6 mm/year, in dense phase CO2 containing 2440 ppmv water and 96 ppmv NO2. This high corrosion rate cannot be explained only by the higher water content. The corrosion rate was measured with electrochemical technique where water was added directly on the electrode surface and it should be confirmed whether the water dissolved quickly enough not to give significant corrosion attack before equilibrium was achieved. When mobility and reactivity of acids in supercritical CO2 were studied, it was found that nitric acid was very mobile and corrosive towards the carbon steel.

Thickness measurements showed localized material losses on carbon steel specimens exposed in dense phase CO_2 in an autoclave where a few droplets of nitric acid were positioned in the bottom. Some experiments in supercritical CO2 (76 bar, 50 °C) with varying concentrations of salts (NaCl, $NaNO_3$, Na_2SO_4), acid impurities (pH 4, HNO3) and 10g/L water have showed that the pit depth rate was the highest after exposure to HNO_3, 1-3 mm/y vs. 0.1-0.2 mm/y for salts. It was confirmed in other studies that NO_3 – impurities show the highest impact on corrosion rates compared to H_2SO_4, Cl- and SO_4 2- and that HNO_3 is approximately twice as corrosive when compared to H_2SO_4 and HCl. It was stated that contaminants such us HCl, HNO_3 and SO_3 will have dramatic effect on the pH of the aqueous phase even in small concentrations while the impact of SO_2 will be moderate. Depressurization of the pipeline will increase the concentration of NO_2 in the remaining liquid phase and this will steadily increase the corrosivity of the system (Ref.[9]).

2.2.3.3 $CO_2 - H_2O - SO_2$ system

The minimum water concentration required for acid formation is not known, but the presence of $FeSO_3$ and/or $FeSO_4$ on the corroded surface in some experiments indicates that the reactions occur at water concentrations far below the water solubility in the pure CO_2-water system. A survey of experiments performed with low amount of water, SO_2 and O_2 are shown in Table 8 . A very low corrosion rate was observed when the water content was lower than 50% of the relative humidity in the pure H_2O-CO_2 system. The corrosion rate was decreasing over time indicating the formation of a protective layer or depletion of impurities over time. Corrosion rates as high as 3-4 mm/y were reported when 1% SO_2 was present in supercritical CO_2 with 650 ppmv water. The corrosion rate decreased to 0.03 mm/y at a SO_2 level of 0.1%.55 It was stated that a concentration of SO_2 less than 0.1% did not lead to significant corrosion of carbon steel. However, in high pressure liquid CO_2 conditions with 650 ppmv of water and 0.05% SO_2, localized attacks were seen with a rate of about 2.4 mm/y. Similar to NO_2, SO_2 will also partition to the remaining liquid phase during pipeline depressurization. The exposed carbon steel foil got a black layer of corrosion products and the corrosion rate was ~0.1mm/year. Sulphuric acid, which is not very mobile, but very hydroscopic, will absorb water from the surrounding CO_2 phase. As concentrated (ca 70-80 mass %) sulphuric acid is less corrosive than diluted one, corrosion rate can increase over time.

H_2O ppmv	SO_2 ppmv	O_2 ppmv	T °C	P bar	Time days	CR mm/y	Reference
488	344	-	25	100	14	<0.005 (spots)	Dugstad[45, 46,56]
1220	344	-	25	100	14	0.02 (spots)	Dugstad[45, 46,56]
488	1000	100	25	100	7	0.01	Dugstad[45, 46,56]
488	200	100	25	100	7	<0.01	Dugstad[45, 46,56]
650	1%	-	50	80	1	3.48	Choi[63]
650	1%	4%	50	80	1	3.7	Choi[63]
650	0.1%	-	50	80	1	0.03	Farelas[55,]
650	0.05%	-	50	80	1	0.05	Farelas[55]
650	0.1%	-	25	80	1	6.8 (localized CR)	Farelas[62]
3310 (sat)	1%	-	50	80	1	5.6	Choi[63]
3310 (sat)	1%	4%	50	80	1	7	Choi[63]
Saturated	1.4%	0.1%	50	100	12	0.8	Xiang[58]
Saturated	0.2%	0.1%	50	100	12	0.15	Xiang[58]
saturated	2%	0.01%	50	100	5	1.5	Xiang[54,58-60]
RH 50%	2%	0.01%	50	100	5	0.04	Xiang[58,54,59,60]

Table 8 "Corrosion rates measured in dense phase CO2 containing water, SO2 and/or O2", (Ref.[9]).

2.2.3.4 $CO_2 - H_2O - SO_2 - NO_2$ and $CO_2 - H_2O - SO_2 - NO_2 - H_2S$ system

A synergistic corrosive effect of SO_2 and NO_2 dependent on relative humidity is observed in atmospheric corrosion. It is assumed that NO_2 increases the rate of SO_2 oxidation to sulphate and acts as oxygen carrying agent phase CO_2. Experiments were performed with different water content, at different temperatures and with different steels (carbon steels, chromium containing steels and corrosion resistant steels), at ambient pressure and at constant flow of CO_2. The water content was measured with a dew point meter. Visible condensation occurred at 5 °C at both 1000 and 8000 ppmv water and corrosion products containing $FeSO_3 \cdot 3H_2O$ and $FeSO_4 \cdot 4H_2O$ (rozenite) were detected. The condensed phase contained sulphuric acid and a 10 times lower concentration of nitric acid. It was reported that carbon steel specimen (L360NB) exposed to CO_2 containing 1000 ppmv H_2O and 4.7 vol% O_2 at 110 bar and 60 °C did not show sign of corrosion, neither after addition of 50 ppmv CO nor 70 ppmv SO_2. However, significant corrosion occurred after addition of 100 ppmv NO.

Different kinetics for the different acid formation reactions were suggested. It was concluded that NO seems to be oxidized to NO_2 and forms nitric acid whereas oxidation of SO_2 to SO_3 is kinetically hindered at such low temperatures and formation of sulphuric acid is hindered indirectly too. When both SO_2 and NO were present, sulphur was found in the oxide layer. A long-term experiment has been made with three different types of steel (CrMo, C, 13Cr) that were exposed to impure supercritical CO_2 at 60 °C and 100 bar. The fluid was changed every third day of the exposure, but the concentrations of the impurities in the CO_2 were not confirmed by any analytical method. The corrosion rate of the carbon steel decreased with exposure time. It was concluded that corrosion products precipitated out as a protective layer. The corrosion rates are very high and much higher compared to the corrosion rates measured at dense phase conditions. It can be questioned if all the condensed phase that is produced in dense phase CO_2 reached the corrosion sample and if there is another inhibiting factor like e.g. nickel presence in the condensed fluid. Another experiment has been performed in dense phase CO_2 containing H_2O, H_2S, NO_2, SO_2 and O_2. The experiment was performed in a rocking autoclave with continuous dosage of CO_2 and impurities. The concentrations of impurities were continuously measured during the exposure. Different analytical techniques were applied: tunable diode laser system for water measurements, non-dispersive, infrared, ultraviolet, visible photometer for Nox and Sox and gas chromatograph for H_2S and O_2 analysis. Impurities were dosed continuously to the autoclave with 3 separate dosing lines as many impurities cannot be premixed.

2.2.4 Effects of impurities on storage capacity

Impurities will affect the volumetric properties of injected CO_2 (Ref.[10]). Figure 25 shows calculated density of supercritical CO_2 with non-condensable impurities for a number of cases at 330 K, which is in the typical temperature range for CO_2 storage evaluations in western Canada.

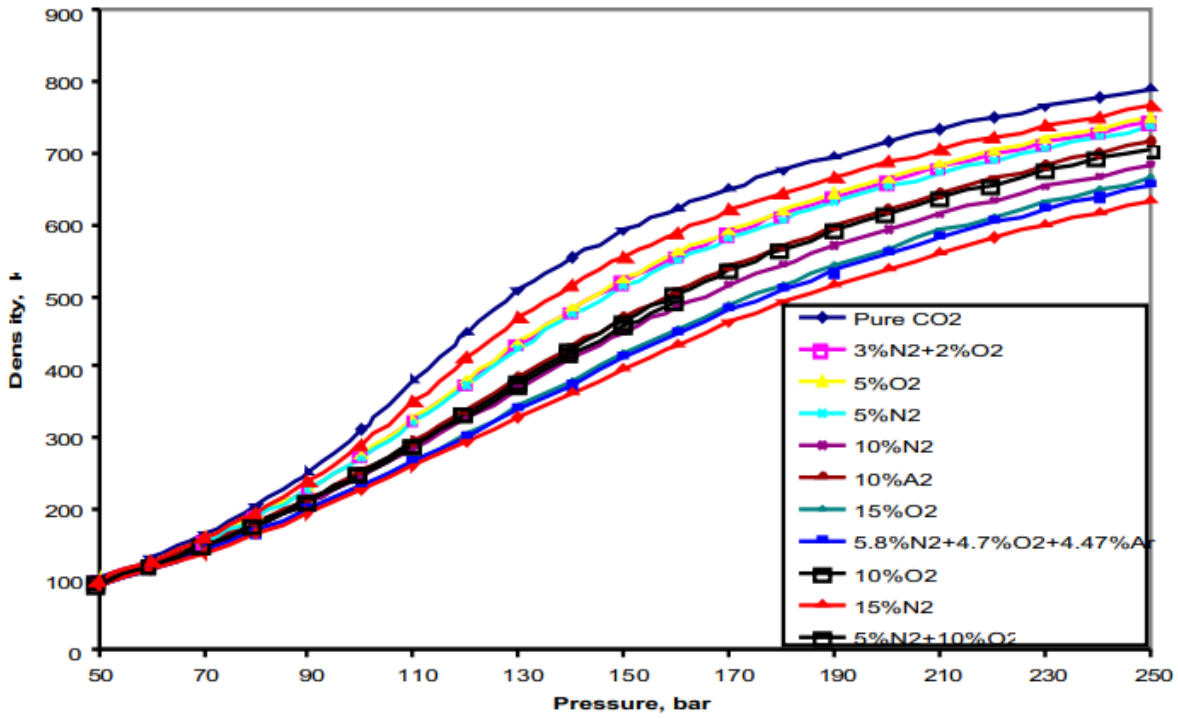

Figure 25 "Calculated density for CO2 and CO2 mixtures as a function of pressure at 330 K", (Ref.[10])

It can be seen that non-condensable impurities such as O_2, Ar, N_2 and H_2 significantly reduce the density of the supercritical CO_2 stream. The reduced density is largely related to increased volume, except for H_2, where the effect of smaller molecular weight is also significant. All these impurity components in CO_2 would cause a volume increase greater than their molar or volume fractions at standard temperature and pressure. For example, 5% vol N_2 will result in a volume increase greater than 5% in the temperature range not above the critical temperature of CO_2. This can be understood from the fact that non-condensable impurities are less dense than CO_2 and hence take greater volumes. If they had the same molar volume as CO_2 there would be no volume increase, provided the interactions between unlike molecules are negligible. The decrease of CO_2 storage capacity due to the contained impurities is thus not only caused by the lower volume fraction of CO_2, but also by the additional volume of less dense impurities. To produce a simple relation regarding the effect of the impurities on the storage capacity for CO_2 for given storage volume, we propose the following expression for the storage capacity (expressed in mass) as a function of density of the CO_2 stream:

$$\frac{M}{M_0} = \frac{\bar{\rho}}{\rho_0(1 + \sum_i m_i/m_{CO2})} \quad (27)$$

Where:

• M and M_0: mass of CO2 in the mixture and in the pure stream, respectively, which occupy the same volume;

• ρ_0 and $\bar{\rho}$: density of the mixture and the pure stream;

• m_i/m_{CO2} : ratio of the mass of impurity i to the mass of CO_2 in the mixture.

The ratio $\frac{M}{M_0}$ represents a normalized store capacity for CO_2 in its supercritical phase, in the case of pure CO2 (zero impurity effect) the ratio equals unity. The right hand side of the equation (27) is a function of temperature, pressure and mixture composition and can be calculated from equations of state. Accordingly, the normalized storage capacity can be determined for given temperature and pressure conditions. Calculated results for a number of mixtures are shown in Figure 26.

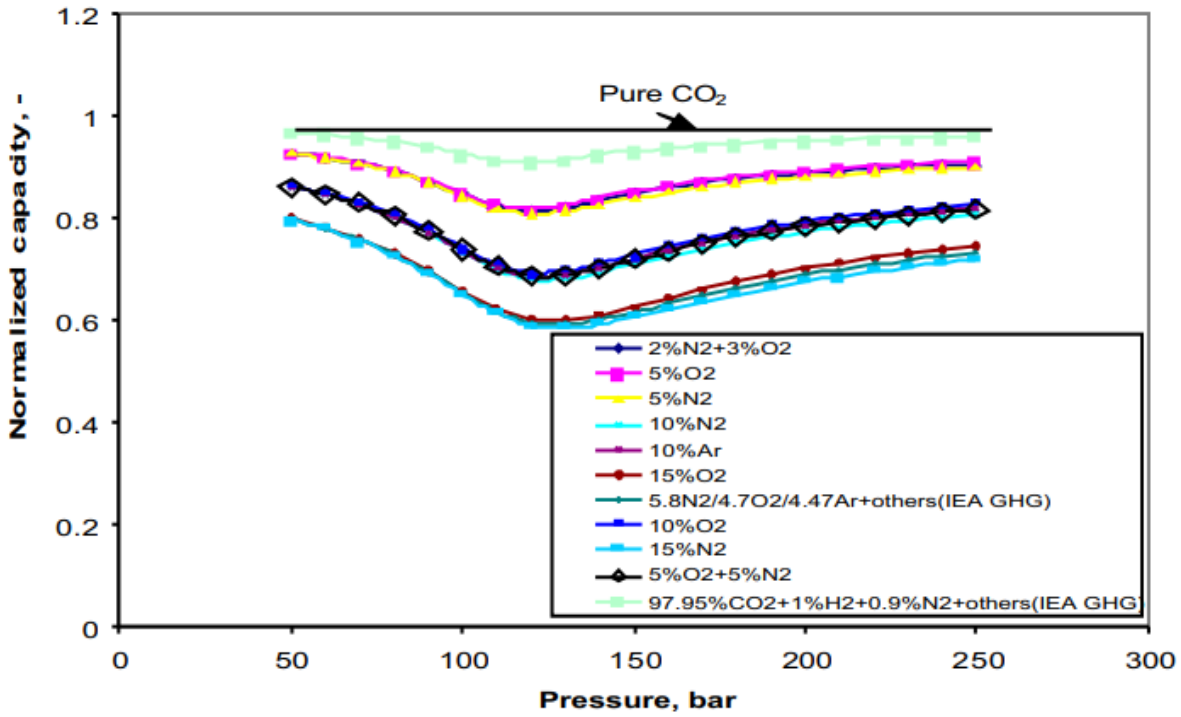

Figure 26 "Normalized CO_2 storage capacity at 330 K in terms of Equation (27)", (Ref.[10]).

For impurities which have higher critical temperature than that of CO_2, no storage capacity minimum would occur in the corresponding CO_2 mixture. Rather, a maximum can appear based on an analysis similar to the one for non-condensable impurities. This has been verified with calculated results for the CO_2 mixture with 2.9 vol % SO_2. The result shows a maximum at about 110 bar, where the storage capacity is increased by over 5%. It is interesting to see that in the maximum region, SO_2 can create space for CO_2. This can be rationalized from the consideration that SO_2 decreases average distance between the molecules of the mixture – an opposite effect of that of the non-condensable gases (Ref.[10]).

2.2.5 Effect of impurities on materials selection

It should be considered that any components which could be present in the streams delivered to the CO_2 capture plant could also be carried through to the exported CO_2 stream at very low levels (Ref.[11]). The types and levels of these trace elements therefore are very hard to quantify as coal and biomass can contain many different types of elements at low levels and some capture options might also add trace elements due to the nature of the process. Consequently, the approach that has been taken for this study has been to consider the effect that the trace elements could have on the various aspects of pipeline transportation and comment on the levels required for these conditions to occur. Table 9 shows a summary of a study made about this issue.

Scenario	CO_2	O_2	N_2	Ar	H_2	CO	H_2S	CH_4	Saturation Pressure (bar)
REF	100								
CO2 MEM1	93		7						82.0
CO2 MEM2	97	3							69.5
ADS1	90	1	9						82.2
ADS2	95		5						75.5
Ca LOOP	95	1	2	2					79.8
OXY1	90	6	3	1					86.7
OXY2	96.5	0.5	2.5	0.5					77.2
PRE	98				2				62.3
H2 MEM	96		1		1	0.5	1.5		77.1
CH4-RICH	98							2	59.0
ULCOS	96		0.5			3.5			82.5

Table 9 " Saturation pressures for scenario compositions for a pipeline decompressing from 150bar and 30°C", (Ref.[11]).

The solubility of water in pure CO_2 has been studied extensively as a function of temperature and pressure. The specification of water in currently operating pipelines ranges between 640ppmv and 20ppmv to avoid the formation of free water in the pipeline at the operating conditions. However, whilst it is known that the presence of impurities will affect the solubility of water in CO_2, there has been little research into the absolute effects of these impurities and the published data is limited. The CO_2-H_2O-CH_4 system has been studied by a number of researchers and the experimental results and thermodynamic models indicate that the addition of CH_4 requires a more stringent water content to be specified as the solubility of water decreases with increasing CH_4 content. Similar results have been seen in the CO_2-H_2O-N_2 system where it has been shown that at a temperature of 40°C, an addition of 10% N_2 can lower the solubility of water in CO_2 by up to 26%.These ternary systems provide useful information on the potential effects of individual components, the data on representative CO_2 streams as presented in the scenarios in this paragraph is extremely limited (Ref.[11]).

2.2.6 Effect of impurities on compressors

CO_2 captured from coal and biomass fired plants is expected to contain larger amount of impurities as compared to gas-fired plants (Ref.[12]). Table 10 provides a listing and typical concentrations of main fluid components found in CO_2 streams captured in post-combustion, pre-combustion and oxy-fuel processes. Given that the thermodynamic state of the CO_2 stream leaving the capture process is expected to have a direct impact on the design and operation of the compression unit.

	Oxy-fuel			Pre-combustion[c]	Post-combustion[d]
	Raw/dehumidified[a]	Double flashing[b]	Distillation[b]		
CO_2 (% v/v)	85.0	96.78	99.30	98.07	99.8
O_2 (% v/v)	4.70	1.20	0.40	-	0.015
N_2 (% v/v)	5.80	1.60	0.20	0.02	}0.045
Ar (% v/v)	4.47	0.40	0.10	0.018	
NO_x (ppm_v)	100	150	33	-	20
SO_2 (ppm_v)	50	36	37	700	10
SO_3 (ppm_v)	20[1]	-	-	-	-
H_2O (ppm_v)	100	-	-	150	100
CO (ppm_v)	50	-	-	1300	10
H_2S (ppm_v)	-	-	-	1700	-
H_2 (ppm_v)	-	-	-	15000	-
CH_4 (ppm_v)	-	-	-	110	-
Bubble-point temperature (°C) at 62 bar	–54.5	14.8	23	16	23

Table 10 "Average compositions of CO2 mixtures captured in oxy-fuel, pre-combustion and post-combustion technologies", (Ref.[12]).

As reported in the introduction of this paragraph, combustion capture is divided into three main parts that will be explained below.

2.2.6.1 Post-combustion capture

In post-combustion capture processes, CO2 is separated from flue gas originating from air-fired combustion. Traditionally, amine-based absorption systems operating at close to ambient conditions [ca 1.5 bar and ca 40 °C] are used to capture the CO2 from the flue gas, which typically contains only 5–15% v/v CO2, with the remaining major components being O2, N2, Ar, H2O, CO, NOX and SO2 (Table 10). Using amine-based solvents CO2 can be purified to above 99% v/v. Due to its relatively high purity, the impact of impurities on thermodynamic properties of post-combustion CO2 streams is often neglected.

2.2.6.2 Pre-combustion capture

In pre-combustion capture, coal is partially oxidised to produce syngas containing CO2 which is then converted in a gas-shift reaction to CO2 and H2. CO2 is later removed in an absorption process. After capture, the pre-combustion stream typically contains ca 98% v/v CO2, up to 1% v/v of N2, H2, CO, CH4, H2O and Ar, and ppm level of acid gases (SO2 and H2S) (Table 10). In contrast to the post-combustion process, which starts from near-atmospheric pressure, in pre-combustion capture the flashing is achieved at pressures around 4.8–11.5 bar, whilst the Selexol absorption system operates usually at pressures from 20 to 130 bar.

2.2.6.3 Oxy-fuel combustion capture

Among the several capture processes, oxy-fuel combustion is considered as one of the most promising options which enables capturing the vast majority of CO_2 from coal-fired power plants and can be retrofitted to the existing fleet of modern pulverised coal-fired power plants. In the oxy-fuel capture, the fuel is burned in a mixture of purified oxygen and recycled flue gas from the boiler containing mainly CO_2 and water vapour. The oxy-fuel flue gas contains relatively high amounts of oxygen and water, other major impurities include N_2 and Ar. Before dehumidification, the CO_2 concentration in oxy-fuel flue gas is around 70%. Water scrubbing is commonly achieved at ambient pressure to condense water vapour and remove traces of ash. Similar to pre-combustion capture, further purification of oxy-fuel derived CO_2 is performed in a sequence of steps at progressively increasing pressures. Removal of some reactive and soluble gases such as SO_3 and HCl can be achieved at pressures below 15 bar. At this stage, the increasing CO_2 stream has purity of ca 75–85% v/v (see Table 10). Also, the 'sour compression' process proposed by Air Products allows reducing the removal SOx and NOx impurities. To further reduce the amount of non-condensable components (such as O_2, N_2 and Ar) and achieve CO_2 purity of over 95% v/v, flash-evaporation and distillation are applied at pressures of ca 15–30 bar (Ref.[12]).

2.2.6.4 Centrifugal compressor

One of the compression technologies used for CCS is the centrifugal compressor that represents a conventional choice for CO_2 compression in the power generation industry. Given that the pressure ratio in a single-step centrifugal compressor is limited to 1.7–2.1, reaching pressures of ca 150 bar requires using either integrally-geared or centrifugal compressors or trains of single-stage compressors, combined with the inter-stage cooling. Current designs of integrally-geared compressors use 8–10 stages to achieve pressures up to 150–200 bar. Centrifugal compressors work by using impellers spinning at a high speed (N) to impact momentum tangentially to the working fluid flowing into the machine through the inlet port. Within the compressor, the fluid flows at high speed through blade channels in the impeller. Adjacent to the outlet duct of the compressor, the fluid decelerates due to flow resistance in the passages of the diffuser and converts to pressure in accordance with Bernoulli's Principle. The outlet pressure (P2) is a function of the density and the velocity of the working fluid. The impurities featured in this study namely N_2, H_2, CH_4 and CO all have lower molecular weights than carbon dioxide. Their introduction into the carbon dioxide stream has the effect of reducing the overall density which will immediately result in the decline of the fluid angular momentum developed from the torque of the compressor rotor shaft. Reduction in fluid angular momentum will lead to degradation of the discharge pressure head. These impurities also increase energy losses resulting in the reduction in the isentropic efficiency. The severity of the degradation of the compressor performance depends on the type and concentration of the impurity in the CO_2 stream flowing in the machine. At the same time, because of large energy losses, the energy requirement of the compressor is highest while isentropic efficiency is lowest. All these elements can be attributed to the drastic reduction in the overall fluid density because sharp contrast between molar mass of hydrogen (2.016 g/mol.) and that of carbon dioxide (44.01 g/mol.). The other impurities, nitrogen, methane and carbon monoxide, have higher molar masses than hydrogen and therefore their effects on compressor performance are less severe.

Therefore, the discharge pressure (P2) will have to be raised far above the critical pressure (P_{crit}) of each working fluid. This will ensure that the working fluids are in the supercritical phase prior to introduction into the transport pipeline. In a centrifugal compressor, the discharge pressure (P2) can be raised either by increasing the shaft speed (N) or enlarging the diameter of the impeller. These methods of increasing the discharge pressure will have different consequences for the energy losses incurred as a result. Increasing the shaft speed while machine size remains unchanged will generate far more energy losses than vice-versa. In other words, increasing shaft speed to generate a particular discharge pressure will require more work input (W_{INPUT}) than if the machine size was proportionally increased while the shaft speed remained constant. The relationship between compressor sizing and work input was investigated using only working fluids with CO_2 purity of 90% and 100%. Only the pure CO_2 and CO_2/CH_4 mixture were sufficiently pressurized to flow out of the discharge port as supercritical fluids. In the remaining three cases (CO_2/N_2, CO_2/H_2 and CO_2/CO mixtures) the discharge pressures (P2) were below their individual critical pressures (P_{crit}) causing them to emerge from the compressor's outlet port in gaseous state. To ensure that all selected working fluids flow out of the compressor in supercritical phase, a standard outlet pressure (P2) of 120 bar was chosen.

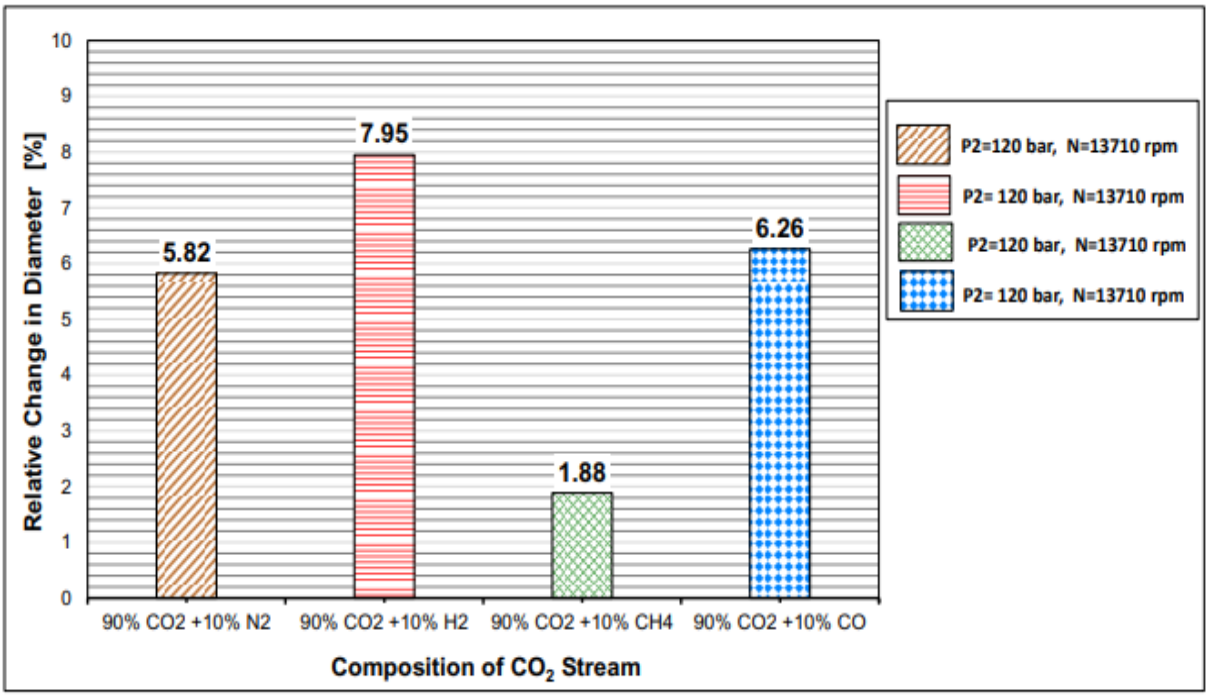

Figure 27 "Effect of raising P2 on relative change in compressor size for different CO_2 streams", (Ref.[13]).

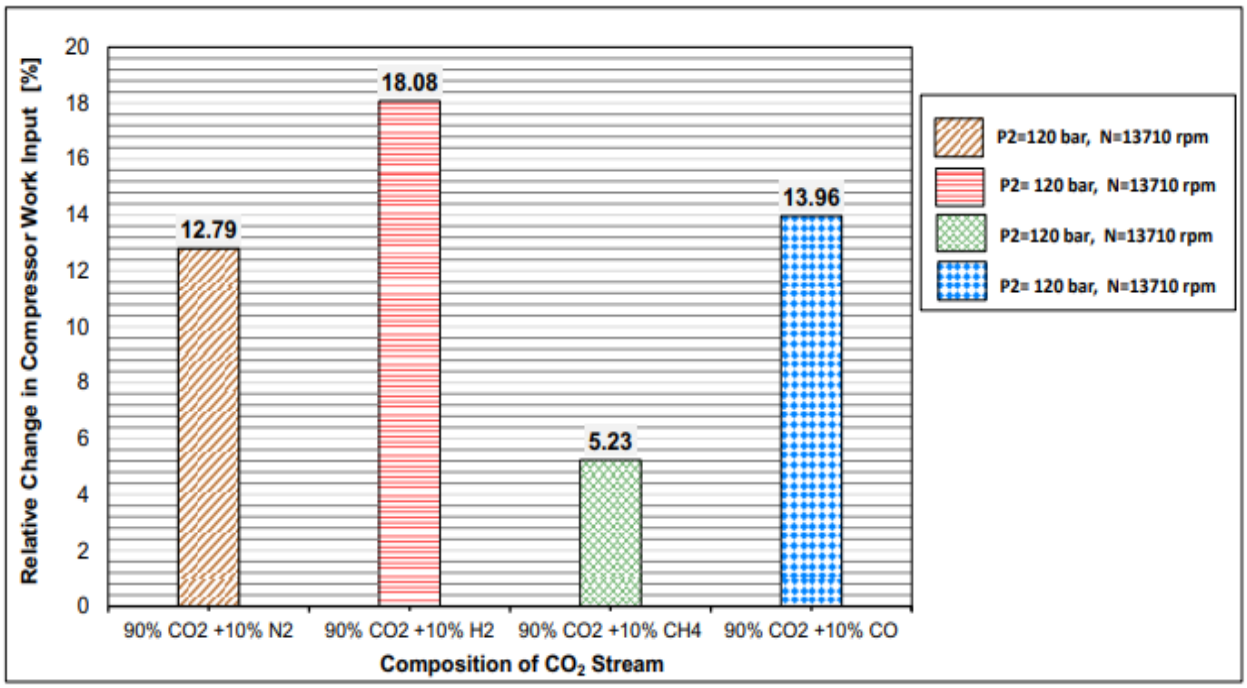

Figure 28 "Effect of raising P2 on relative change in work input for different CO2 streams", (Ref.[13])

Therefore, for each working fluid, compressor size and work input required to raise the compressor discharge pressure to 120 bar was calculated. Relative changes in compressor size and work input are shown Figure 27 and Figure 28. These percentage differences are used as a method of evaluating how the increase in P2 affects the impeller diameter size and energy requirement for a compressor handling each of the selected CO_2 mixtures compared to one handling pure CO_2. For a given temperature and pressure, the fluid density progressively decreases as working fluid changes from pure CO_2 to CO_2/CH_4, CO_2/N_2, CO_2/CO and finally, CO_2/H_2 mixtures. Therefore, it is not surprising that a compressor handling the CO_2/H_2 working fluid the least dense mixture will require the highest amount of energy (W_{INPUT}) to generate the stipulated outlet pressure of 120 bar. After all, compression work input is inversely proportional to fluid density. For a constant shaft speed of 13710 rpm, this energy requirement will translate to the largest compressor resizing effort. In relative terms, the compressor size will increase by 7.95% and work input will increase by 18.08% as shown in Figure 27 and Figure 28 when the compressor shifts from handling pure CO_2 to CO_2/H_2 mixture. The CO_2/CH_4 mixture, with the second highest density values after those of pure CO_2, requires the least amount of energy and the least compressor re-sizing effort. In relative terms, the work input will increase by 5.23% and the machine size will increase by 1.88% when compressor shifts from handling pure CO_2 to CO_2/CH_4 mixture. Generally speaking, for a given shaft speed and discharge pressure, compressor sizing and work input are in a directly proportional relationship. That relationship is inversely proportional to the overall fluid density which in turn is dependent on the composition of the working fluid (Ref.[12][13]).

CHAPTER 3 – EXPERIMENT: PIPELINE FAILURE

3.1 Foreword

This chapter will focus on the analysis of a recent scientific paper (published in 2019) based on experimental approaches to evaluate how and how much impurities impact in CO_2 transport applications. In particular we will see a case study related to the effects of high pressure dense phase CO_2 (as we have seen in chapter 2, high pressure and other anomalies in thermophysical properties are caused by the presence of impurities) on some technical pipeline aspects. The work investigates the consequences of pipeline failure.

3.2 Case study 4 – Pipeline failure through experimental and numerical studies

Transportation of Carbon Dioxide (CO_2) via high-pressure pipelines from source to storage site represents an important link in the Carbon Capture and Storage (CCS) chain. The safety of the operation is a priority, it is therefore necessary to develop a comprehensive understanding of the consequences of a possible pipeline failure. CO_2, as we know, is a hazardous substance and its accidental release may lead to catastrophic damages. This case study describes an experimental investigation of the dispersion of CO_2 in the atmosphere in a full-scale burst test of a pipeline containing high-pressure dense phase CO_2. The experiment was carried out to simulate a CO_2 pipeline failure in the real world. The test rig consisted of a buried 85 m long, 610 mm diameter pipeline test section connected at either end to 116 m long reservoirs. An explosive charge detonated at test section half-length initiated a rupture in the pipe wall top surface, releasing the high-pressure contents. The atmospheric dispersion of the CO_2 following the explosive release was measured. Computational Fluid Dynamics (CFD) simulations of the dispersion of CO_2 following the release are also described. The CFD models were validated against the experimental data. The models were then extended to estimate the consequence distances related to CO_2 dispersion following failure of longer pipelines of various diameters under different wind speeds and directions. Comparison of the results with prior studies was carried out (Ref.[14]).

3.2.1 Experimental set-up and procedures

The test featured a 610 mm Outer Diameter (OD), X65 steel pipe, filled with a mixture of about 91% CO_2 and 9% N2 pressurised to 15 Mpa. The initial temperature of the mixture was about 12 °C. The test section was about 85 m long and consisted of an assembly of eight pipe segments connected to reservoirs at either end. The reservoirs are also pipes of 610 mm OD, each about 116 m long. The overall pipe length was thus about 317 m. The pipe was laid West-East and buried under about one metre of soil. An explosive charge installed on the top surface of the test section at half-length would be detonated to initiate a propagating fracture in the pipe which extended along the pipeline in both directions. It was expected that the fracture would be arrested within about 20 m on either side of the initiation point. The released gas would disperse over the terrain in response to the prevailing wind conditions on the day.

Weather forecasts suggested that around the date of the test, the wind at the site would blow predominantly from the West-Southwest (WSW) direction about 11.5° with respect to the pipe axis laid West-East. Figure 29 shows the fan-shaped sensor layout for spot measurements of CO_2 concentration compatible with this expected wind direction. The sensors were oxygen cells set up to measure the spot concentration of O_2, from which the CO_2 concentration could be deduced. A total of 50 sensors were installed at the locations indicated by the red and blue dots in Figure 29. Two probes were located directly upstream of the source, and another four in the cross-wind direction. The remaining 44 probes were arranged in a 'fan' pattern spanning an angle of ± 45° symmetrically on either side of the expected wind direction, and located on 50 m, 100 m, 200 m, 300 m, 400 m and 500 m arcs centred at the mid-point of the test section.

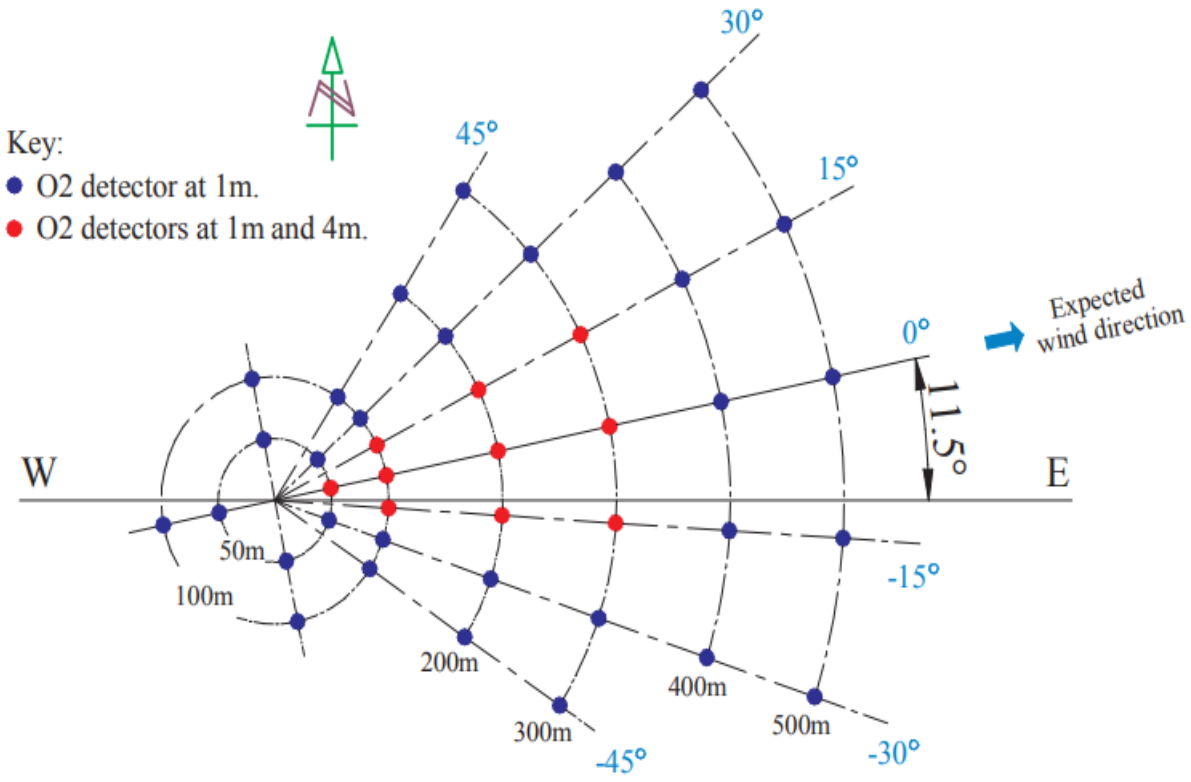

Figure 29 " Field instrumentation in the experiment, showing locations of O2 detectors downwind", (Ref.[14]).

The burst test was carried out in the afternoon on 30 September 2017 when the wind speed and direction looked promising as measured using two wind probes placed about 460 m upstream of the test site, at 5 m and 10 m height from the ground. Figure 30 shows the measured wind speed and direction over a period of 300 s, starting at the instant when the explosive charge was detonated and the CO_2 was released into the atmosphere. Over this period, the wind speed was reasonably consistent. The wind direction was close to the expected direction. This meant that the test scenario was such that all of the sensors would lie in the path of the spreading CO_2 cloud. This conclusion was reached based on the results of a number of pre-test CFD simulations carried out to validate the sensor arrangement.

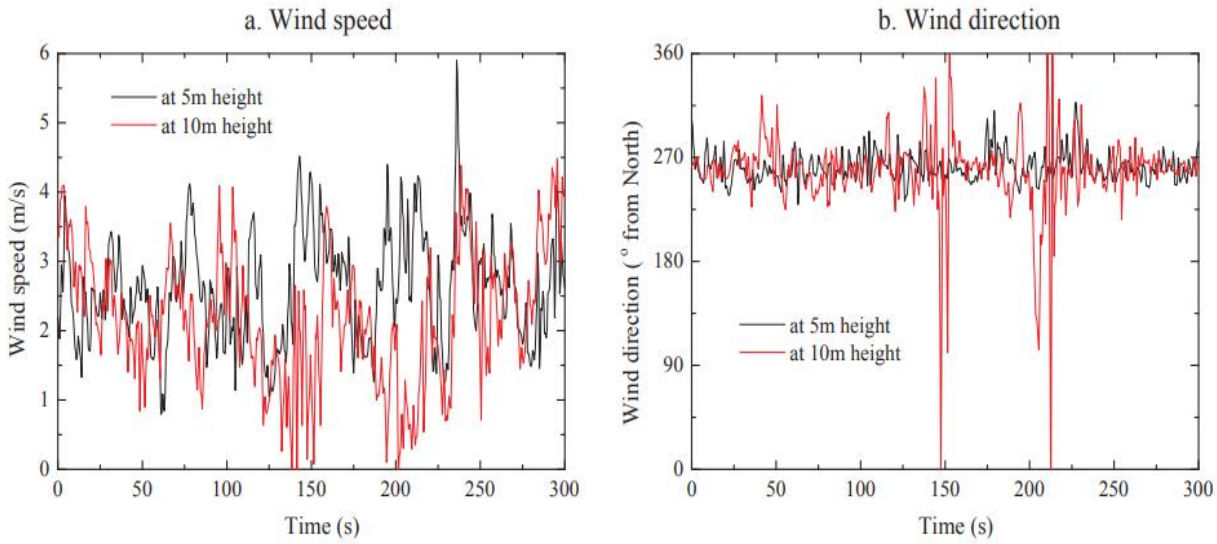

Figure 30 "Wind speed and wind direction histories at 5 m and 10 m heights, measured from the instant of the test initiation at about 460 m upstream of the source ", (Ref.[14]).

Figure 31 shows a snapshot of the spreading CO_2 cloud captured by an aerial drone, as well as the crater formed by the CO_2 explosion and the fractured test section. In the test, the CO_2 cloud rose momentarily to about 250 m, as was the debris that was thrown out of the crater formed. Thereafter, the cloud sank to the ground, even as it was dispersed by the prevailing wind. The measurements reflect that the CO_2 cloud took about 300 s to blow over the site. The fracture in the pipe wall propagated along the top surface towards both ends, and was arrested when the total fracture length reached about 42.5 m. Figure 31 also shows that the force of the explosion caused the pipe to bend sideways at about half-length, even as the bent half was thrown out of the crater. After the event, a series of measurements using drones were carried out to estimate the area of the crater opening at ground level.

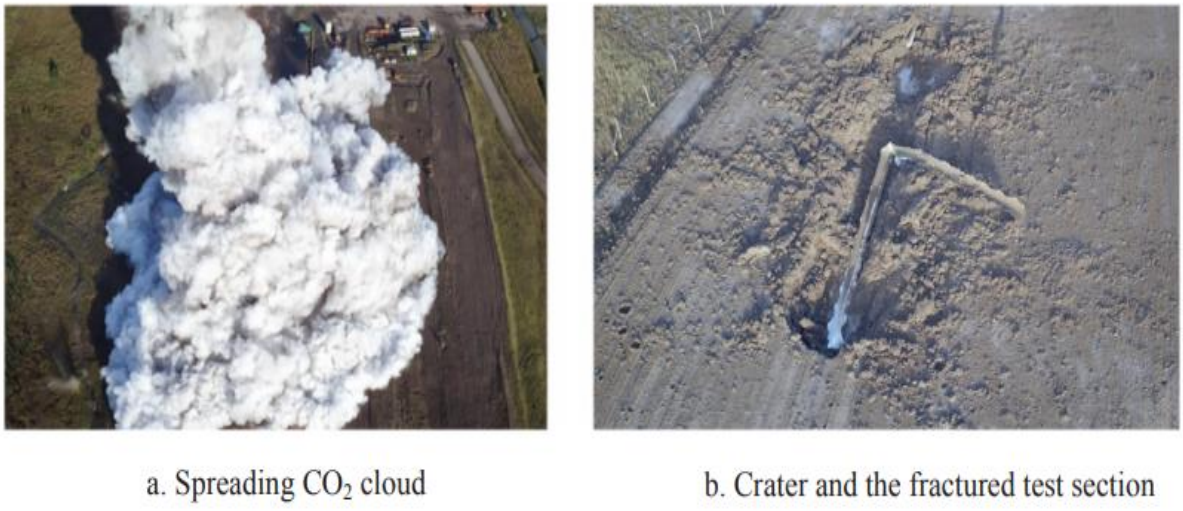

Figure 31 "Aerial views of the spreading CO2 cloud, crater formed by CO2 explosion, and the fractured test section.", (Ref.[14])

Figure 32 shows the result in the form of an outline of the crater. The total length of the crater is 44.85 m, slightly longer than the fracture length. The average width of the crater is about 7.4 m, which is 12 times of the pipe OD. Figure 33 shows the measured pressure decay in the reservoir. It indicates that the contents of the pipe were released in less than 12 s. The kink in the reservoir pressure transients corresponds to the saturation pressure of about 7.8 Mpag (Ref.[14]).

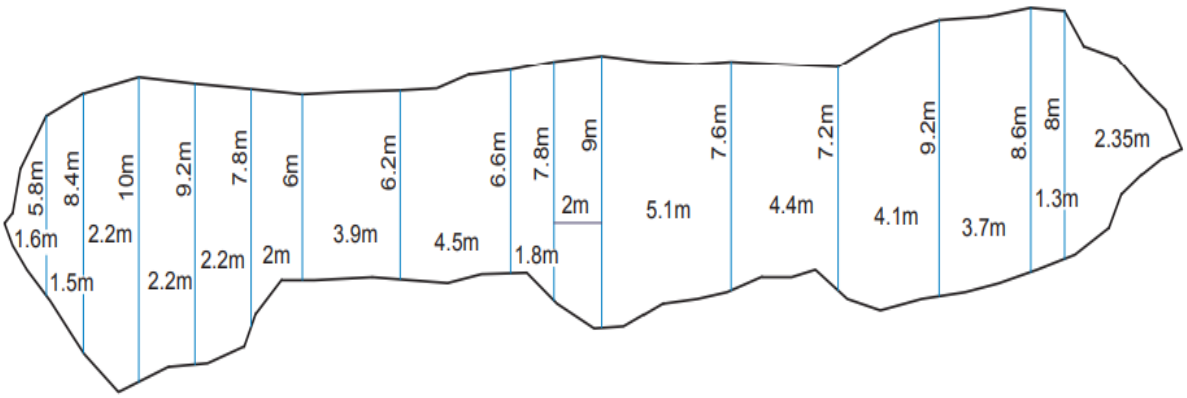

Figure 32 "Crater outline as measured in the West-East and South-North directions.", (Ref.[14]).

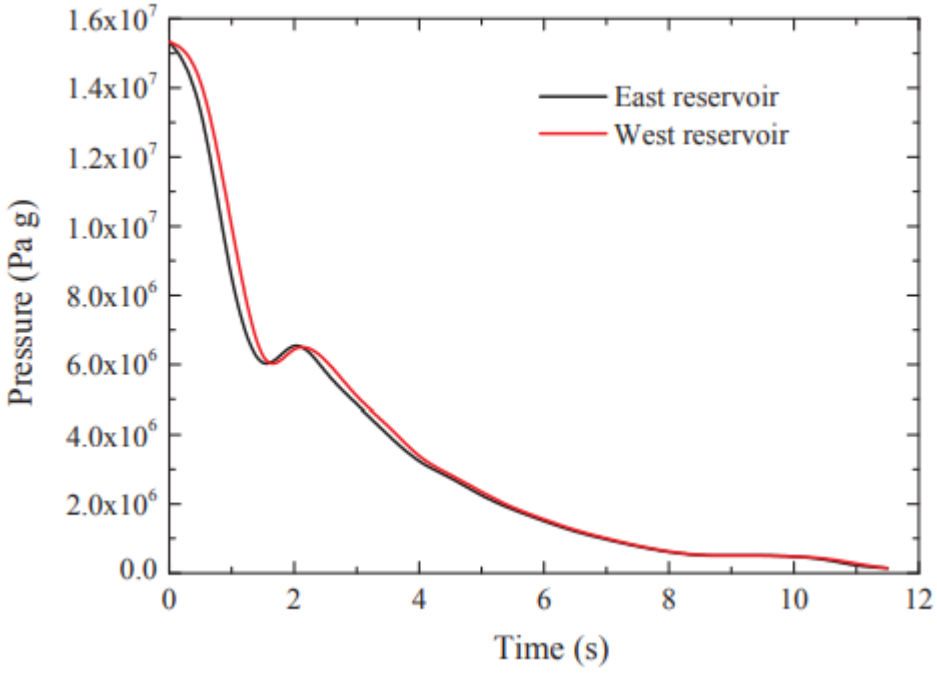

Figure 33 "Measured pressure decay in the reservoirs", (Ref.[14]).

3.2.2 Mathematical models

This section describes all of the mathematical and physical notions relevant for the work done, in particular it shows all of the equations and models useful to evaluate some phenomena. For a pipeline containing high-pressure CO_2 in liquid or supercritical state, the initiation of a fracture will be followed by rapid depressurisation of the gas. This will result in a two-phase flow in the pipe, and a decompression wave travelling along the pipe away from the opening, at nearly the speed of sound. Also, the released gas will be exposed to the ambient pressure, leading to a highly under-expanded region near the fracture. During the atmospheric expansion, the fluid will cool down significantly due to the Joule-Thompson effect. This may cause the formation of dry ice particles in the fluid. The solid particles may sublimate in mid-flight or deposit on the ground, but eventually will undergo sublimation due to the much warmer environment. The depressurisation and expansion of the CO_2 along with details of the fracture propagation directly affect the release source strength. However, as this process is highly complicated, a numerical simulation to obtain the release rate will be very time-consuming. In this study, the release rate due to the fracture propagation is approximated by:

$$\dot{m} = C_1(e^{C_2 t} - e^{C_3 t}) \qquad (28)$$

Where:

• t : time;

• C_1 and C_3 : constants controlling the peak release rate, the release rate decay and the overall released mass;

For a specific explosive release due to pipeline fracture, the constants in equation (28) are determined to give the right values of mass inventory (equal to the area under the $\dot{m}(t)$ curve), the peak release rate and the release duration. In conjunction with the source plane used in the dispersion modelling, the peak release rate tuned by the constants will ensure that the corresponding maximum fluid velocity after expansion agrees with the fluid velocity calculated by the atmospheric expansion model. For the above full-scale burst, considering that the mass inventory was emptied within 12 s (Figure 33), the constants are defined as:

$$C_1 = 75{,}300\ kg/s;$$
$$C_2 = -1\ s^{-1};$$
$$C_3 = -10\ s^{-1}.$$

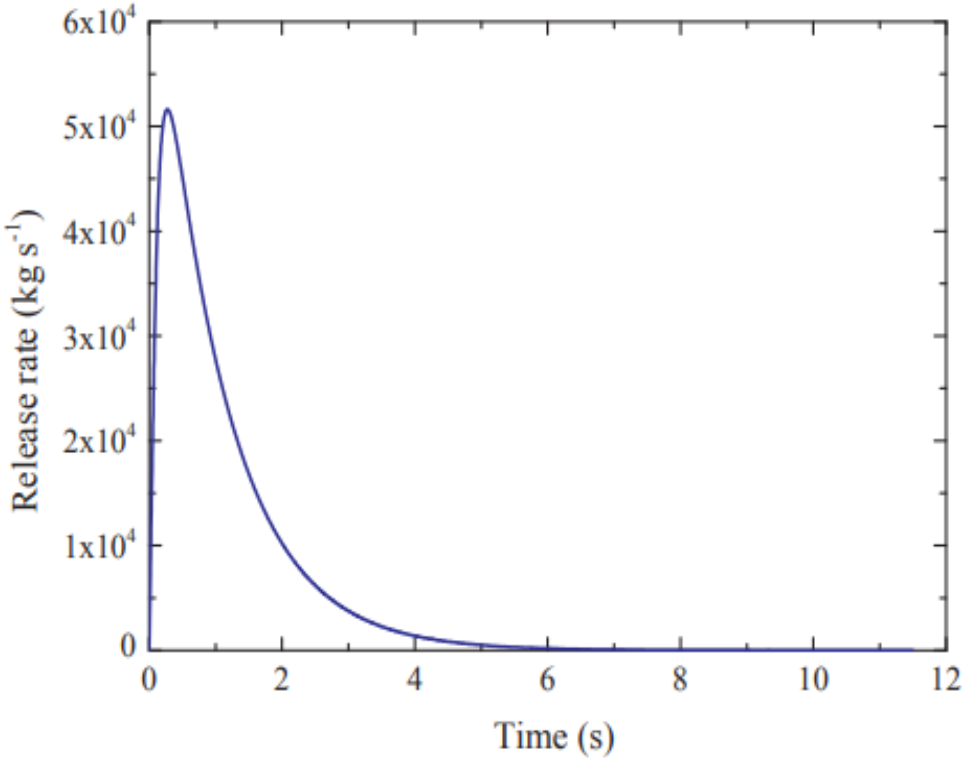

Figure 34 "Assumed release rate for the full-scale burst test", (Ref.[14]).

Figure 34 shows the simulated time history of the release rate. The specified constants ensured that the total mass released within 12 s is about 67 tonnes, which agrees with the mass inventory in the pipeline. The possible formation of solid CO_2 particles in the source may affect the dispersion. However, in the experiment, it was not observed that there were dry ice particles deposited on the ground. This may be because the particle size was quite small and they did not have a chance to deposit on the ground to form a visible dry ice bank before sublimating in mid-flight. To reduce the complexity of the model, the source fluid for dispersion modelling was assumed to be in a gaseous state. This is also preferable for risk assessment as conservative gas concentrations will be predicted. In the model, the effect of low temperature at the CO_2 source on thermodynamic properties such as density was considered. However, constant values were used for transport properties like viscosity and thermal conductivity. The viscosity and thermal conductivity of CO_2 were set as $1.37 \times 10^{-5}\, kg/m\,s$ and $0.013\ W/mK$ respectively in the dispersion model. In the experiment, the CO_2 was released from an opening created in a buried pipe. The released fluid had to burst through the soil cover, creating a trench above the pipe, before emerging out into the atmosphere.

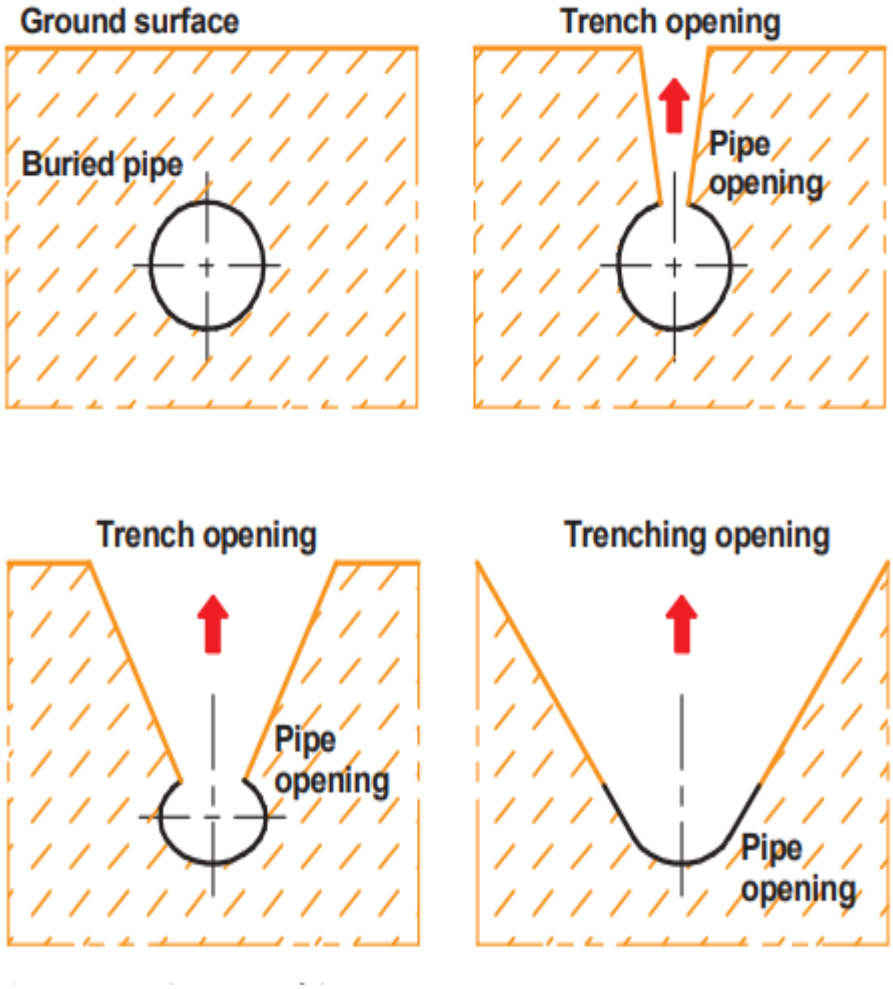

Figure 35 "Schematic trench opening process (not to scale.", (Ref.[14]).

Figure 35 shows schematically the possible sequence of steps resulting in the creation of the trench in the experiment. The pipe axis is perpendicular to the plane of the diagrams. In this study, the trench opening at ground level was assumed to be the inlet to the dispersion domain. It is assumed that at the ground level, the fluid is already at post-expansion stage and the pressure reaches the ambient pressure. Therefore, incompressible flow can be assumed in the dispersion model to reduce the computing time. According to the crater opening dimensions obtained in the test (see Figure 32), a rectangle on the ground surface with a length of the fracture length and a width of 12 times of the pipe diameter will be used as the CO_2 inlet plane for dispersion modelling.

In this study, ANSYS Fluent V14.5 (a simulation program) was employed for the dispersion simulation, which solves the Reynolds-averaged mass, momentum, energy and scalar transport equations.

Continuity equation:

$$\frac{\partial \rho}{\partial t} + \nabla \cdot (\rho \vec{v}) = 0 \qquad (29)$$

Momentum equation:

$$\frac{\partial (\rho \vec{v})}{\partial t} + + \nabla \cdot (\rho \vec{v} \vec{v}) = -\nabla p + \nabla \cdot (\bar{\tau}) + \rho \vec{g} \qquad (30)$$

Energy equation:

$$\frac{\partial (\rho E)}{\partial t} + \nabla \cdot [\vec{v}(\rho E + p)] = \nabla \cdot \left[k_{eff} \nabla T - \sum_i h_i \vec{J}_i + \left(\vec{\tau}_{eff} \cdot \vec{v} \right) \right] \qquad (31)$$

Where:

- ρ : density;
- $\vec{v}$: velocity vector;
- p : pressure;
- $\rho \vec{g}$: gravitational body force per unit volume;
- E : total energy;
- k_{eff} : effective thermal conductivity;
- h_i : specific enthalpy of species i;
- $\vec{J}_i$: diffusion flux of species i;

While:

$$\bar{\tau} = \mu\left[(\nabla\vec{v} + \nabla\vec{v}^T) - \frac{2}{3}\nabla\cdot\vec{v}I\right]$$

Where:

• μ : dynamic viscosity;

• I : unit tensor.

The 'species transport' model was employed to predict the fraction of each species, by solving the convection-diffusion equation given by:

$$\frac{\partial(\rho Y_i)}{\partial x} + \nabla(\rho\vec{v}Y_i) = \nabla\cdot\vec{J}_i + R_i \quad (32)$$

Where:

• Y_i : mass fraction of species i;

• R_i : net rate of production of species i;

The SST k-ω model was used for representing the effects of turbulence, as it was proposed to be more appropriate for dispersion modelling of high-momentum CO_2 releases. Compared with the standard k-ω model, the SST k-ω model has a modified turbulent viscosity formulation to account for the transport effects of the principal turbulent shear stress, and it also applies gradual change from the standard k-ω model in the inner region of the boundary layer to a high Reynolds number version of the k-ε model in the outer part of the boundary layer. The transport equations for the turbulence kinetic energy k and the specific dissipation rate ω are given by:

$$\frac{\partial(\rho k)}{\partial t} + \frac{\partial(\rho k v_i)}{\partial x_i} = \frac{\partial}{\partial x_j}\left[\left(\mu + \frac{\mu_t}{\sigma_k}\right)\frac{\partial k}{\partial x_j}\right] + G_k - Y_k \quad (33)$$

and

$$\frac{\partial(\rho\omega)}{\partial t} + \frac{\partial(\rho\omega v_j)}{\partial x_j} = \frac{\partial}{\partial x_j}\left[\left(\mu + \frac{\mu_t}{\sigma_\omega}\right)\frac{\partial\omega}{\partial x_j}\right] + G_\omega - Y_\omega + D_\omega \quad (34)$$

Where:

• v_i and v_j : velocity components;

• μ : dynamic viscosity;

• μ_t : turbulent viscosity;

• σ_k and σ_ω : turbulent Prandtl numbers for k and ω respectively;

• G_k and G_ω : generation of k and ω respectively;

• Y_k and Y_ω : dissipation of k and ω due to turbulence respectively;

• D_ω : cross-diffusion term.

Standard coefficients were used for turbulence modelling and the Boussinesq approximation was used to model the effect of buoyancy. In the dispersion modelling, appropriately simulating the wind velocity is very important, as it will directly affect the dispersion process. In the atmospheric boundary layer, the wind velocity usually reduces with a decrease in altitude due to frictional effects. To account for the variation in wind velocity with elevation, a power-law is used to describe the vertical wind profile:

$$u = u_r(z/z_r)^\alpha \quad (35)$$

Where:

• u : wind velocity at height z;

• u_r : reference wind velocity measured at the reference height z_r;

• α : wind shear exponent;

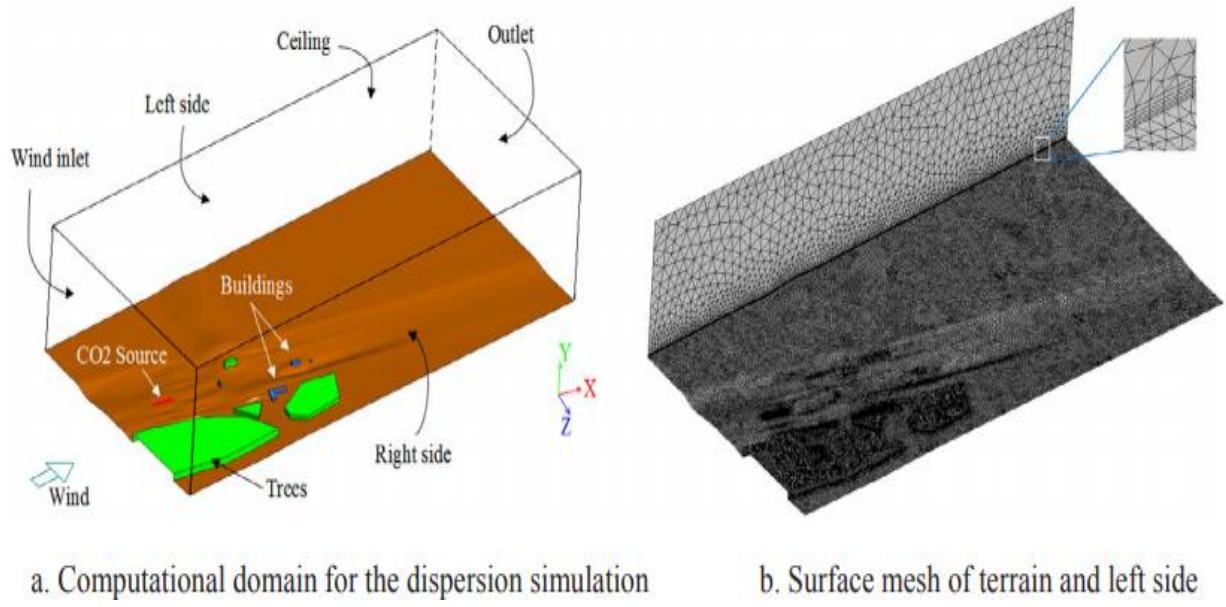

Figure 36 "Computational domain showing the wind direction and boundaries, and the corresponding computational mesh showing the local refinement and the detail of 'inflation' layers", (Ref.[14]).

The proposed numerical methods were used to simulate the CO_2 dispersion in the full-scale burst. Figure 36a shows the computational domain of the dispersion model, measuring 1500 m (length) × 800 m (width) × 400 m (height). The wrinkles in the ground surface show that floor conforms to the terrain topography. The computational domain was aligned with the time-averaged wind direction during the test (Figure 30b). The wind inlet was placed 200 m upstream of the source at ground level. The lateral and vertical dimensions were chosen such that the dispersion plume could be accommodated within the computational domain throughout the duration of the dispersion. The outlet of the computational domain is located sufficiently far downstream of the source and the region most likely to be affected by the dispersion. Since the aim is to model the dispersion in the atmosphere, obstacles such as patches of trees and buildings are 'removed' from the computational domain, so that they are not part of the atmosphere. Boundary conditions for the dispersion model were defined as follows (Figure 36a):

I. Wind inlet: velocity inlet, ambient pressure and temperature, velocity profile described by equation (35).

II. CO2 source: mass flow inlet, gaseous CO_2 at ambient pressure and temperature of −78 °C, mass flow rate described by equation (28).

III. Outlet: pressure outlet with ambient pressure and temperature.

IV. Ground, surfaces of buildings and tree blocks: no-slip, isothermal wall with temperature equal to the ambient temperature.

V. Ceiling, left side and right side: impermeable 'symmetry' boundaries.

Figure 36b shows part of the surface mesh at ground level and the left side of the computational domain. As the geometry is relatively complex, the computational domain was mainly discretised into tetrahedral cells. The overall mesh consists of a total of about 1 million cells, which are densely packed in regions where large gradients in the flow parameters are expected, such as near the source and in the ridges on the ground. The detail in Figure 36b also shows 5 inflation layers were used adjacent to the ground surface for adequate simulation of the boundary layer. The time-averaged wind speeds at 5 m and 10 m heights measured during the test (Figure 30a) were used to deduce the wind shear exponent of the power-law correlation for the Wind Inlet boundary. With a reference height of 5 m, the reference wind velocity and the wind shear exponent were obtained as 2.7 m/s and 0.055, respectively. Both the vertical wind profile described by equation (35) and the mass flow rate time history shown in Figure 34 were modelled using User-Defined Functions (UDFs), and they were applied to the Wind Inlet and CO_2 Source boundaries respectively. The overall simulation was carried out in two steps:

I. A steady-state simulation to establish the wind field over the terrain, which provided the initial conditions;

II. A transient simulation in which the CO_2 was introduced from the 'source' (CO_2 inlet to the dispersion domain).

Figure 37 compares the measured and predicted histories of CO_2 concentration at specific locations (refer to Figure 29 for the locations where the concentrations were monitored) at progressively increasing distances from the release location at time intervals after the rupture event. Overall, there is good agreement between the simulated and measured CO_2 concentration over time at different distances from the rupture site. At a downwind location, the CO_2 concentration tends to rise to a maximum value initially and then gradually reduce. This trend was well captured by the model at different distances. At almost all downwind distances, the maximum CO_2 concentration was captured reasonably well. Although the CFD model tended to over-predict the peak concentration, it is usually preferable for risk assessment. In the experiment, it seems that the CO_2 was dispersed slower than in the simulation. This may be due to the variation of the wind direction in reality. In the CFD model, average (and constant) values of wind speed and direction were applied, with the variation ignored.

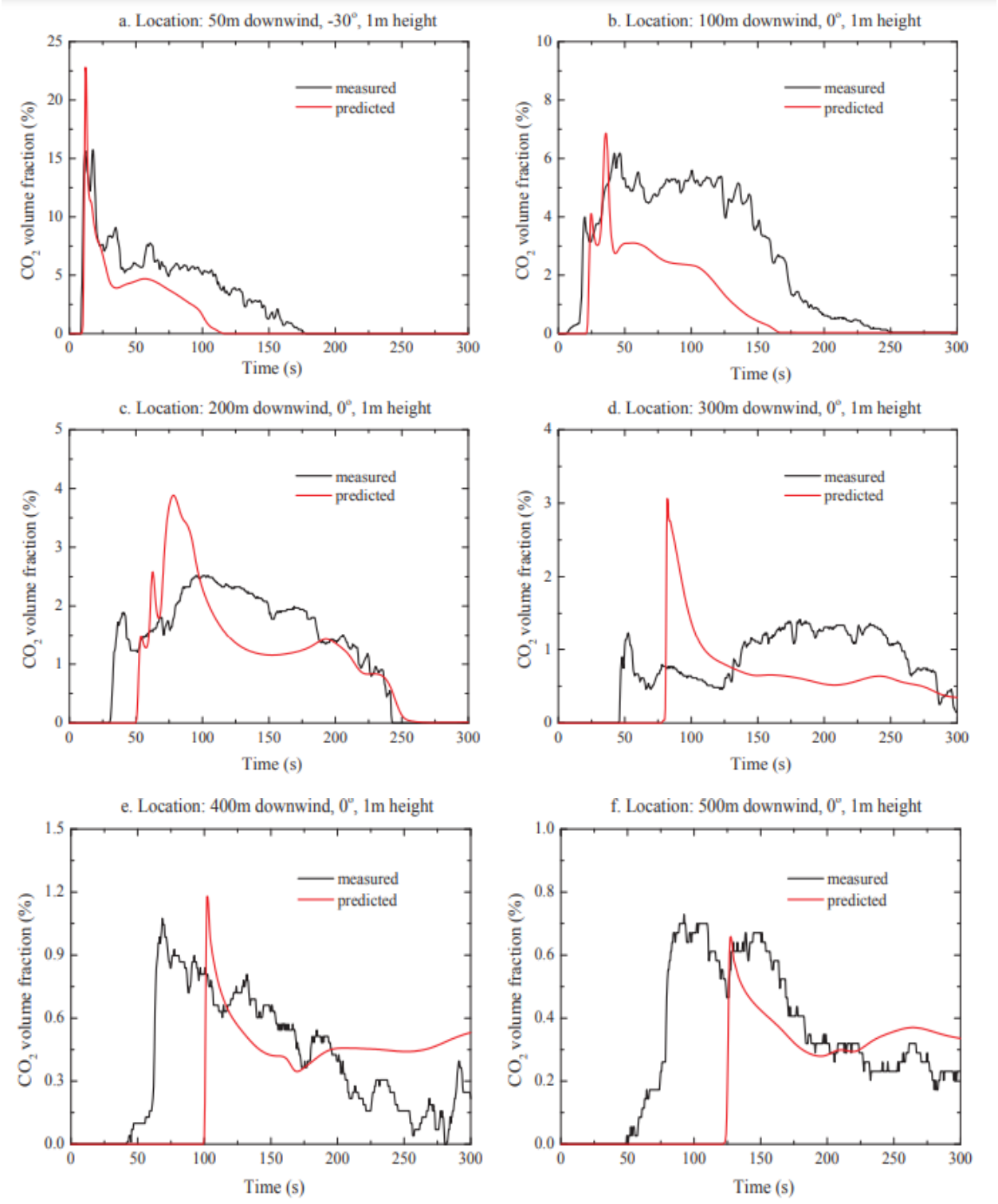

Figure 37 "CO2 concentration at downwind locations: measured vs predicted", (Ref.[14]).

To evaluate the performance of a dispersion model, a set of statistical performance measures has been proposed. These include the Geometric Mean (MG), the Geometric Variance (VG), the Fractional Bias (FB), the Normalised Mean Square Error (NMSE), and the fraction of Cp (predicted concentration) within a FACtor of 2 (FAC2) of Co (observed concentration).

A perfect model would have MG = VG = FAC2 = 1 and FB = NMSE = 0. While these values are virtually impossible to achieve in reality, a model with acceptable performance has been defined as one with the following feature:

I. FAC2 > 0.5;

II. −0.3 < FB < 0.3 or 0.7 < MG < 1.3;

III. NMSE < 4 or VG < 1.6;

MG	VG	FB	NMSE	FAC2
0.86	1.14	−0.18	0.25	0.96

Table 11 "Summary of model performance measures", (Ref.[14]).

Considering the predicted and observed peak concentrations at all the monitored downwind locations, the performance measures of the CFD model were calculated as shown in Table 11. It indicates that all performance measures are within the acceptable range. This suggests that the proposed numerical methods are capable of handling the dispersion simulation of a large CO_2 release in a full-scale burst test and providing satisfactory predictions of the dispersion patterns (Ref.[14]).

3.2.3 Consequence distance prediction of CO2 pipeline failure

To obtain a comprehensive understanding of the consequences of high-pressure CO_2 pipeline failures, the proposed CFD model was applied in a number of simulations to predict the consequence distance following fracture of a pipeline carrying pure CO_2 with ID varying from 200 mm to 800 mm. The length of the pipeline considered here is 10 km, with the fracture initiated at the mid-point and propagating towards either end. The initial pressure and temperature inside the pipeline were assumed 15 Mpa and 10 °C, respectively. For a well-designed pipeline, the fracture propagation is expected to be arrested within four pipe segments. As the length of one pipe segment is about 15 m, in this study, the length of the overall fracture is assumed to be 60 m. This provides the basis for the estimation of two-stage mass flow rate specification (explained below) and the dimensions of the CO_2 inlet to the dispersion domain in the CFD model.

Pipeline ID (mm)	Mass inventory (tonnes)	Release duration (s)	Peak release rate (kg s^{-1})	C_1 (kg s^{-1})	C_2 (s^{-1})	C_3 (s^{-1})
200	292	890	19,950	40,000	−3.45	−15.55
400	1170	730	40,290	58,500	−1.46	−14.20
600	2632	665	62,710	90,010	−1.00	−10.00
800	4679	630	80,920	195,500	−0.95	−3.11

Table 12 "Summary of release parameters", (Ref.[14]).

The release rate due to the fracture was estimated at first. Table 12 lists the basic source parameters, including the mass inventory, release duration and the maximum release rate. It indicates that for pipelines with the same length, larger pipe diameter leads to shorter emptying time.

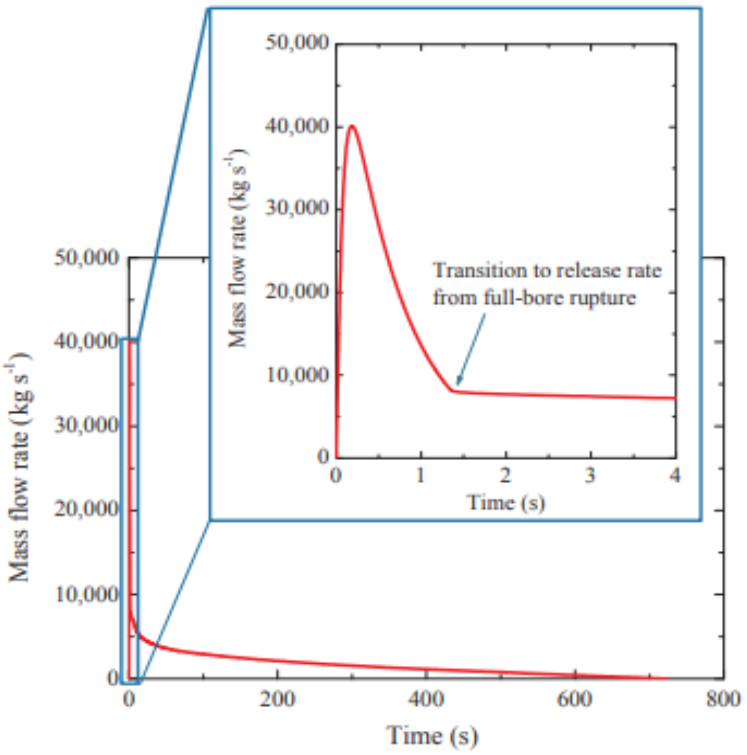

Figure 38 "Release rate of the 10 km long pipeline with 400 mm ID, with the initial variation shown in detail", (Ref.[14]).

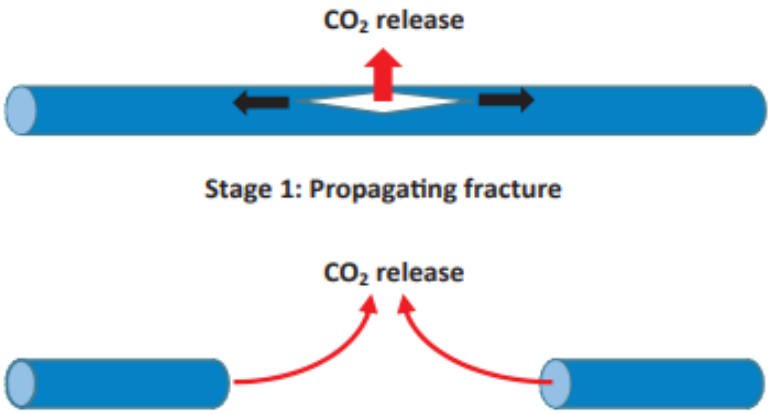

Figure 39 "A schematic diagram of the release stages: (1) stage 1, during fracture propagation; (2) stage 2, after arrest of propagating fracture, release rate modelled as discharge from two full-bore ruptured pipelines", (Ref.[14])

Figure 38 shows the release rate time history of the 400 mm ID pipeline. The release consists of two stages (refer to Figure 39). The first stage is an explosive discharge due to the propagating fracture. This lasts for a very short time and presents a spike in the release rate, the release rate in this stage was modelled using equation (28). The second stage represents the CO2 release after the arrest of the fracture propagation. In this stage, the total release rate is made up of discharge from two full-bore ruptured pipelines. The release rate due to a full-bore rupture can be solved using one-dimensional transient mass, momentum and energy balance equations expressed in terms of fluid velocity, density, and pressure in conjunction with a real gas equation of state. The detail in Figure 38 clearly shows the transition from explosive discharge to full-bore discharge. The dispersion was modelled over a flat featureless terrain. In all subsequent dispersion simulations, a 'neutral' atmospheric stability class was assumed. Wind speeds from 2 m/s to 10 m/s at a reference height of 10 m were used to evaluate the wind inlet velocity profiles and setting up the steady-state wind field.

Reference wind speed (m s^{-1})	α
2	0.20
4	0.13
6	0.12
8	0.11
10	0.10

Table 13 "Wind shear exponent α used for different wind speeds", (Ref.[14]).

Table 13 shows the wind shear exponents used in the simulations. It should also be noted that the pipeline is assumed parallel to the wind direction, as this configuration was supposed to result in the longest consequence distance.

In the following analysis of the consequence distance, two representative CO_2 concentration levels were considered: 50,000 ppm and 80,000 ppm. According to the Australian Standard, a CO_2 concentration level of 50,000 ppm will result in 'very rapid breathing, confusion and vision impairment', while that of 80,000 ppm will cause 'loss of consciousness after 5–10 min'. The consequence distance was determined as the maximum distance away from the pipe fracture centre contained by two concentration envelopes corresponding to these two concentration levels.

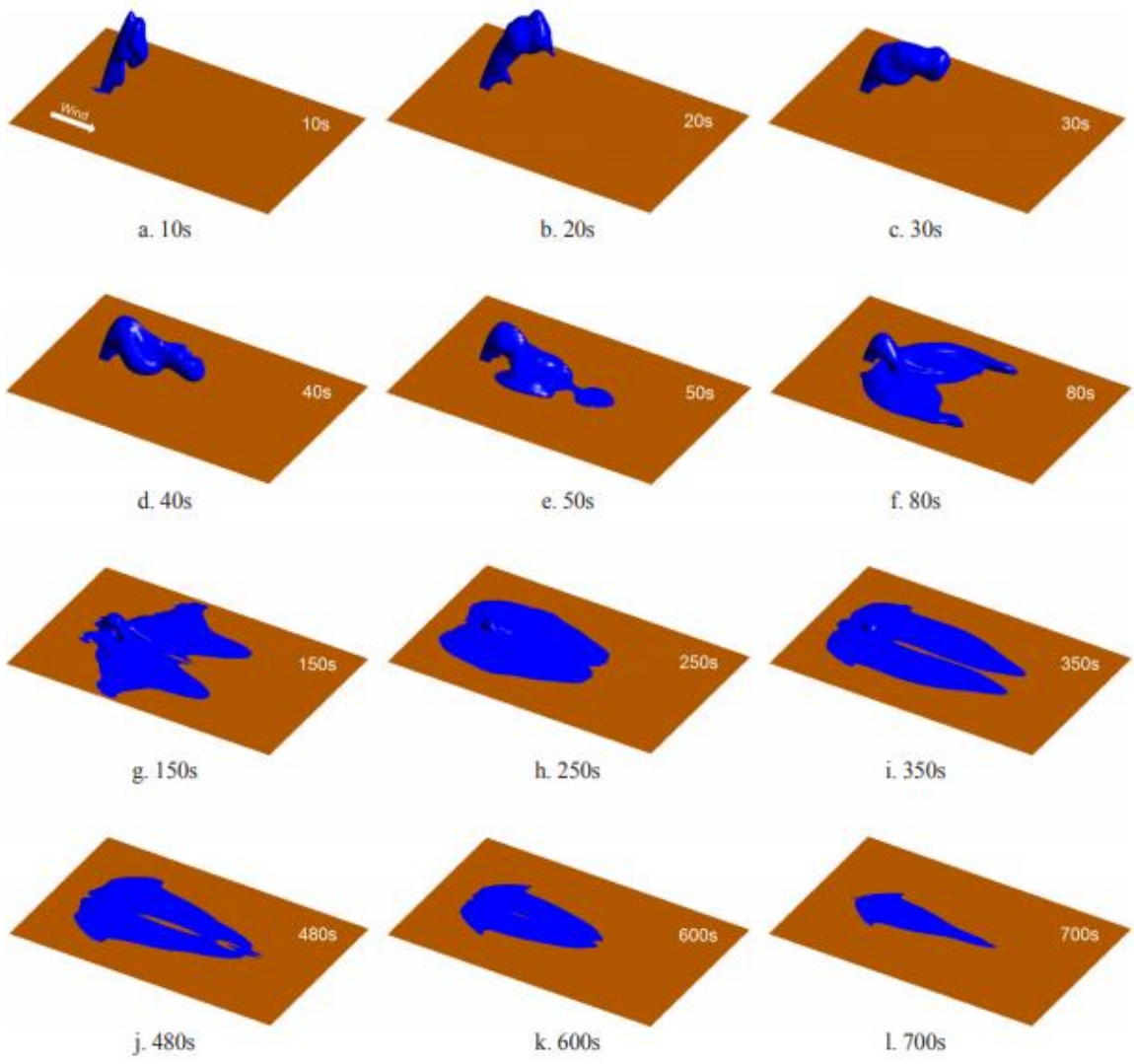

Figure 40 "Evolution of CO_2 envelope (80,000 ppm isosurface) due to release of the 400 mm ID pipeline under 4 m/ s wind", (Ref.[14])

Figure 40 shows the predicted evolution of the CO_2 cloud (represented by 80,000 ppm isosurfaces) in a typical case, dispersion following the fracture of a 400 mm ID pipeline, simulated assuming a 4 m/s wind speed. It is found that initially the dispersion reflects the high release rate, causing the heavy gas plume to reach a high altitude. In this case, the 80,000 ppm envelope can reach a height of over 200 m.

After travelling for a certain distance with the wind, the cloud loses its initial vertical momentum and gradually begins to sink towards ground level. Simultaneously, the CO_2 cloud is weakened due to diffusion, turbulent mixing and entrainment of the ambient air into the cloud. Eventually, the envelope corresponding to a certain concentration value reaches its maximum distance on the ground when the source strength is too weakened to cause further spread. In this test case, at 480 s, the 80,000 ppm CO_2 envelope reaches its maximum distance from the release centre. Subsequently, it is gradually weakened by the wind.

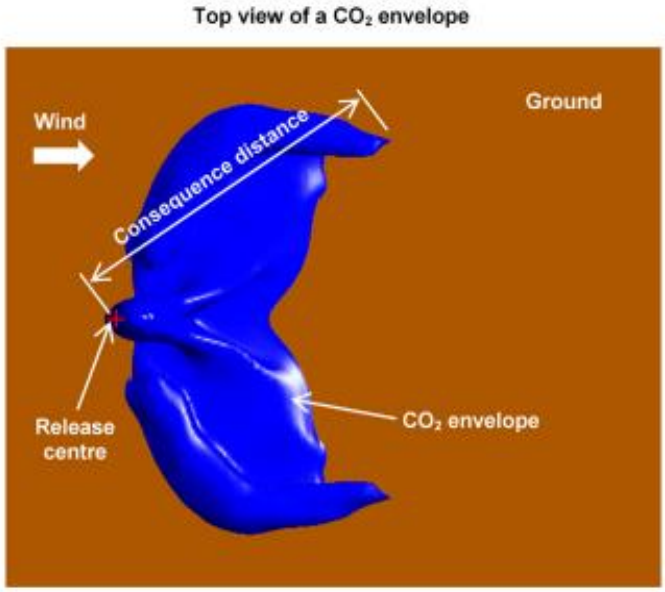

Figure 41 " Schematic of the measurement of consequence distance. The distance is determined as the maximum distance away from the pipe fracture centre contained by the concentration envelope, indicating the farthest reach of the cloud ", (Ref.[14]).

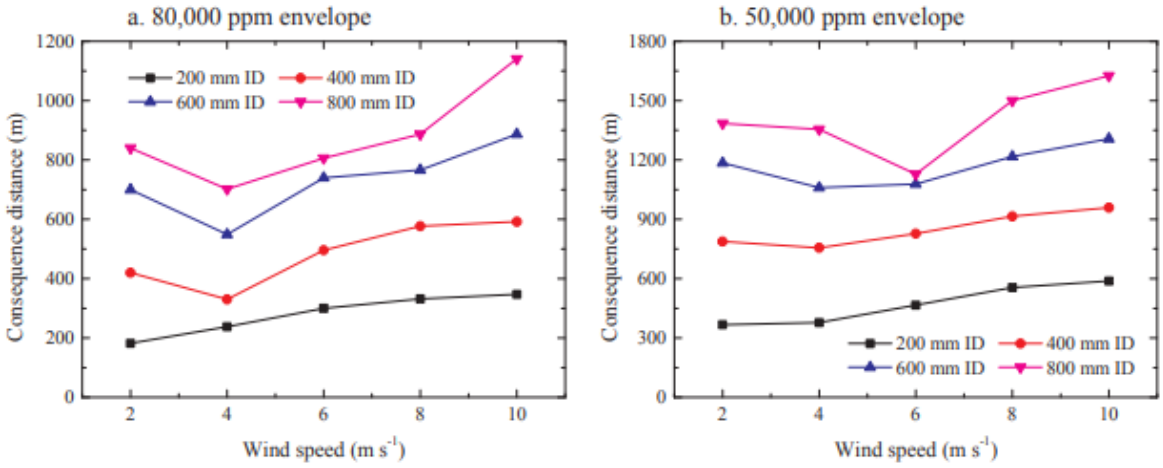

Figure 42 "Consequence distances obtained for different wind speeds", (Ref.[14])

Figure 41 shows how the consequence distance is measured. It can be observed that the farthest reach of the CO_2 cloud is not necessarily in the strictly downwind direction.

Figure 42 shows the predicted consequence distances for the 10 km long pipeline with different IDs as a function of wind speed. For the same stagnation pressure, it is clear that larger diameter pipelines correspond to longer consequence distance, reflecting the larger initial mass inventory released into the atmosphere. Figure 42 shows that the wind speed significantly affects the consequence distance. For wind speed ranging from 2 m/s to 10 m/s, compared to the minimum values, the consequence distance defined by the 80,000 ppm concentration envelope can be increased by 90%, while that of 50,000 ppm concentration can be increased by 60%. Figure 42 also shows that most of the time higher wind speed produces longer consequence distance and this works well for the 200 mm ID pipeline. However, for pipelines with larger ID, it can be observed that the consequence distances produced by 2 m/s wind are longer than those produced by 4 m/s wind. This may be due to the less mixing due to lower turbulence levels at the lower wind speed. If the release source is strong enough, it will take a long time before the CO_2 cloud is sufficiently diluted. During this longer amount of time, the cloud can be transported over longer downwind distances even by a low wind speed.

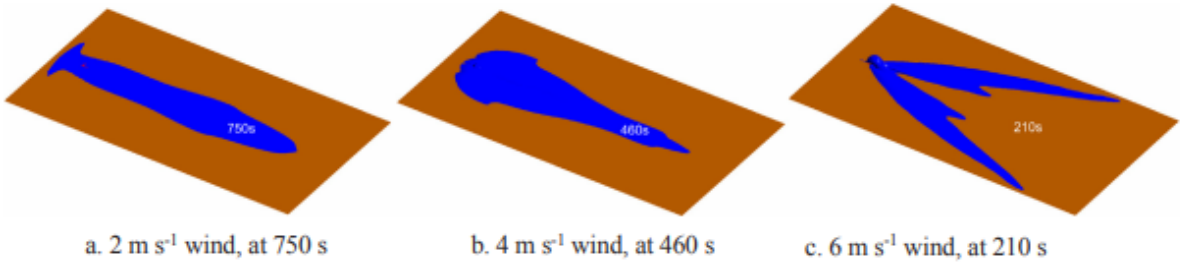

Figure 43 "CO2 envelope (50,000 ppm isosurface) at its longest distance from release centre under different wind speeds (400 mm ID pipeline)", (Ref.[14]).

Figure 43 shows the CO_2 envelopes due to the release of 400 mm ID pipeline at their longest impact distances from release centre under different wind speeds. Clearly, the dispersion under 2 m/s wind speed is much slower, taking 750 s for the cloud to travel downwind (Figure 43a) before it starts shrinking. On the contrary, with a wind speed of 6 m/s , the 50,000 ppm envelope stops advancing much sooner (in ~210 s, Figure 43c). It can also be noted in Figure 43 that: for the 80,000 ppm envelope, a 2 m/s wind can result in a longer consequence distance than a 6 m/s wind, for a 800 mm ID pipeline; for the 50,000 ppm envelope, a 2 m/s wind can result in a longer consequence than a 6 m/s wind, for both 600 mm and 800 mm ID pipelines, while a 4 m/s wind can produce a longer consequence distance than a 6 m/s wind, for a 800 mm ID pipeline. It is noted that a V-shaped envelope develops for a 6 m/s wind speed (Figure 43c). A V-shaped envelope is usually seen in a vertical release, which is due to vortices set up by the difference in buoyancy between air and the released gas. The V-shaped concentration profiles can also be observed in natural gas dispersion (Ref.[14]).

3.2.4 Summary of results

In this study, an experimental investigation and CFD (Computational Fluid Dynamics) simulations of the dispersion of CO_2 following a full-scale burst test are presented. The full-scale burst test featured a 610 mm OD, 317 m long steel pipe, filled with a CO_2-N_2 mixture of 91% CO_2 and 9% N_2, pressurised to 15 Mpa. The fracture was initiated at half-length of the pipe, propagating towards both ends, and was arrested when the total fracture length reached about 42.5 m. The full-scale burst was instrumented to measure the pipe fracture propagation characteristics, and the dispersion of CO_2 in the atmosphere following release from the fractured pipe. This study deals only with the dispersion aspect. A site-specific CFD model is employed to simulate the experimental scenario and the predicted downwind concentrations showed good agreement with measurements. The evolution of CO_2 concentration at different downwind locations was well captured and the peak concentrations were also predicted reasonably well. The CFD model is extended to simulations of releases due to the fracture of a 10 km long CO_2 pipeline. Dispersion patterns are generated for various combinations of pipe diameter (200–800 mm ID) and wind speed (2–10 m/s), and assuming a flat featureless terrain. The consequence distances obtained provide a basis for the estimation of the 'measurement length' before the deployment of CO_2 pipelines. This information will contribute to the identification of safe distances and the selection of appropriate safety class and design factors. This will help encourage industry investment in further deployment of CCS technology through removal or reduction of technical, safety and economic factors currently hindering these projects. Wind speed significantly affects the consequence distance. Usually higher wind speeds will produce longer consequence distances. However, for a relatively large release, even lower wind speed can result in longer consequence distance due to lower turbulent mixing rate and entrainment, requiring more downwind travel time before the gas cloud is sufficiently diluted. For example, for pipeline ID ranging from 400 mm to 800 mm, a 2 m/s wind speed results longer consequence distance than a 4 m/s wind speed. In prior studies, estimates of the consequence distance were based on the analysis of a horizontal release due to a full-bore rupture, which were expected to provide conservative prediction. Results in the present study indicate that, compared to a vertical release due to a full-scale pipeline fracture, the consequence distances were significantly underpredicted in prior work. This is due to the much larger release rate from a full-scale fracture compared to the release rate due to a full-bore rupture. To provide sufficient confidence, results from simulations of full-scale fractures should be used in the risk assessment. The orientation of the pipeline with respect to the wind direction may significantly affect the consequence distance for relatively high wind speeds. If the pipeline is neither parallel nor perpendicular to the wind direction, a high wind speed can spread the pollutant mainly on one side, resulting in much longer consequence distance measured on that side. Simulation results show that a wind speed greater than 6 m/s can result in a much longer consequence distance when the pipeline is aligned 45° to the wind direction. For a 400 mm ID pipeline with its axis at 45° to the wind direction, the consequence distance can increase by up to 60% for wind speed higher than 6 m/s, compared to a symmetrical configuration and dispersion pattern. Release from a longer pipeline will usually produce longer consequence distance. However, the rate of increase of the consequence distance diminishes progressively longer pipelines. Simulations of a 400 mm ID pipeline under 4 m/s wind speed indicate that the consequence distance curves tend to plateau off when the pipeline length is increased up to 30 km.

Due to the Joule-Thompson effect, CO_2 exits from the high-pressure pipeline with very low temperature following an accidental release. Although the CO_2 cloud will be gradually warmed up by the warmer air, it will create a relatively low-temperature zone in the atmosphere as it disperses. Simulation results show that, for the fracture of a 400 mm ID pipeline, the temperature of a region within a distance up to 600 m from the release centre can be reduced by 10 °C. It should be noted that, the consequence distances obtained in this study were calculated for wind speeds below 10 m/s. If the effects of pipeline length and the pipeline orientation with respect to wind direction are considered in determining the separation between a CO_2 pipeline and residential areas, an appropriate safety factor should be carefully chosen (Ref.[14]).

CHAPTER 4 – CONCLUSIONS

The purpose of this document was to analyse the issues concerning the transport of CO_2, with an emphasis on the consequences of impurities on both the thermodynamic properties and the characteristics of the pipeline. However, CO_2 transport is a fairly complicated technological process that must take into account many factors, furthermore this process has been subject to several variations over the years. This chapter aims to summarize the processes of transport of CO_2 by pipeline through the reading of a recent scientific article (published in 2020), containing a systematic review of the topic, in order to understand what are the technologies and methodologies characterising this process nowadays.

4.1 General description

First of all it is necessary to describe the main physical and chemical properties of CO_2: some of the main properties and implications are shown in Table 14 (Ref.[15]).

Transport method	Description	Requirement	Advantage	Disadvantage	Applications
Gaseous transport	CO_2 is always gaseous during transportation.	CO_2 needs to be throttled and depressurized before entering the pipeline. The pressurization during the transport process must not exceed the critical pressure to avoid the phase change of CO_2. No insulation required for the pipeline.	The requirements of pipeline materials for gaseous transport are relatively low.	In the same situation, the transport volume is small, and the economy is poor. Poor adaptability to high-pressure transport.	Small capacity, short distance pipeline, densely populated area.
Liquid transport	CO_2 is always liquid during transport.	Temperature control needs to be very strict to prevent CO_2 from becoming gaseous or solid.	The friction during the transport is small, the viscosity is small, and the density is small, which is convenient for transportation.	High vapor pressure may affect regular transport.	Small capacity, short distance pipeline, densely populated area. Suitable for use in oil fields.
Dense-phase transport	CO_2 is always in dense-phase during transportation.	The transport temperature should be slightly lower than that of supercritical transport, and the whole pressure range should not be changed	The investment cost of dense-phase transport is much lower than gaseous transport and liquid transport, but closer to supercritical transport.	Only applicable to areas with relatively small populations.	Pipeline with large capacity and long-distance. Less densely populated areas.
Supercritical state transport	CO_2 is always in a supercritical state during transportation.	The transport temperature and pressure are both above the critical value.	Good economy.	Due to changes in temperature and pressure, many impurities may precipitate from the CO_2 and form a gas phase.	Pipeline with large capacity and long-distance. Less densely populated areas.

Table 14 "Characteristics of the four CO2 transport methods", (Ref.[15]).

CO_2 pipeline is similar to the natural gas pipeline, which can reach thousands of kilometres passing through mountains, cities, and oceans.

However, the differences between CO_2 pipelines and gas pipelines are transmission medium, operation and pipe material strength, which are explained subsequently. CO_2 is similar to natural gas in colour, odour, and transportation form, but CO_2 is non-toxic and non-flammable. When a pipeline leaks, CO_2 spreads much slower than natural gas since it is heavier than air, and it accumulates in low-lying areas. Although the frequency of leakage failure of CO_2 pipelines is low, its leakage and diffusion patterns are still worthy of further study.As the physical properties of CO_2 are quite different from those of natural gas and its transportation form is greatly affected by temperature, pressure, and impurities, it is obvious to assist to phase transformation during the transportation process. In the process of natural gas transportation, special attention should be paid to the temperature and pressure to control the formation of the hydrate. For CO_2, the impurity limit should also be considered. CO_2 pipes are more prone to ductile fracture. Because of low temperature transportation and decompression waves, the material properties of CO_2 pipes have higher requirements (Ref.[15]).

4.2 CO_2 pipeline transport – Process and pipeline design

Two aspects will be reviewed to describe CO_2 transport via pipeline, that are process and pipeline design (Ref.[15]). The research of the CO_2 transport process can be divided into three aspects that are state equation, transport process, and thermodynamic analysis, while the design aspect, in order to be understood, has to be analysed under several aspects that are: length, pipe diameter, wall thickness, pressure, and construction.

4.2.1 State equation

The phase behaviour of CO_2 is at the basis of transport research. At different temperatures and pressures, CO_2 will have different phase states. In the study of phase states, the determination of state equation is of critical importance. At present, scholars from various countries have not agreed on a common opinion on the selection of CO_2 state equation proposed to consider the impact of impurities and to verify the reliability of the state equation for specific impurity components in the design of CO_2 pipelines. Several scientists over the years have proposed models to evaluate the most appropriate equation of state of carbon dioxide; a comprehensive summary of this aspects is proposed here below. Farris (1983) proposed Benedict-Webb-Rubin-Starling (BWRS) equation as the state equation for CO_2. Through the CO_2 pipeline project in Rocky Mountain, the economy of supercritical transport is proved. Hein used Peng-Robinson (PR) equation (Peng and Robinson, 1976) and Soave Redlich Kwong (SRK) equation to calculate the thermodynamics of CO_2. Zhang et al. (2006) adopted the Boston-Mathias modified PR equation (PRBM) as the basis of CO_2 thermodynamic calculation. Li and Yan (2006) proposed that the reliability of the state equation needs to be verified experimentally because the choice of the state equation has a significant influence on the pipeline design. Huh et al. (2009) investigated the reliability of SRK, PR, BWRS, and other state equations through experiments, and concluded that PR and PRBM equations are more suitable for CO_2 pipeline transport. Seevam et al. (2008) used PR equation to analyse the influence of impurities on CO_2 pipeline transport, and determined that impurities may affect pipeline design, compressor or pump power. Through the comparison of the experimental and theoretical results, Chen (2016) concluded that PR equation is more practical to calculate the physical parameters of CO_2.

It can be inferred from the review that in different case studies, many scholars have obtained inconsistent results and recommended different state equations, demonstrating that gas quality analysis is necessary before conducting phase analysis. It can be also concluded that the PR-based state equation (PR equation or its improved form) is more suitable for CO_2 pipeline.

4.2.2 Transport process

The forms of CO_2 transport include gaseous transport, liquid transport, dense-phase transport, supercritical transport, and solid transport. In terms of feasibility, the first four methods are more suitable for long-distance and large-scale transportation.

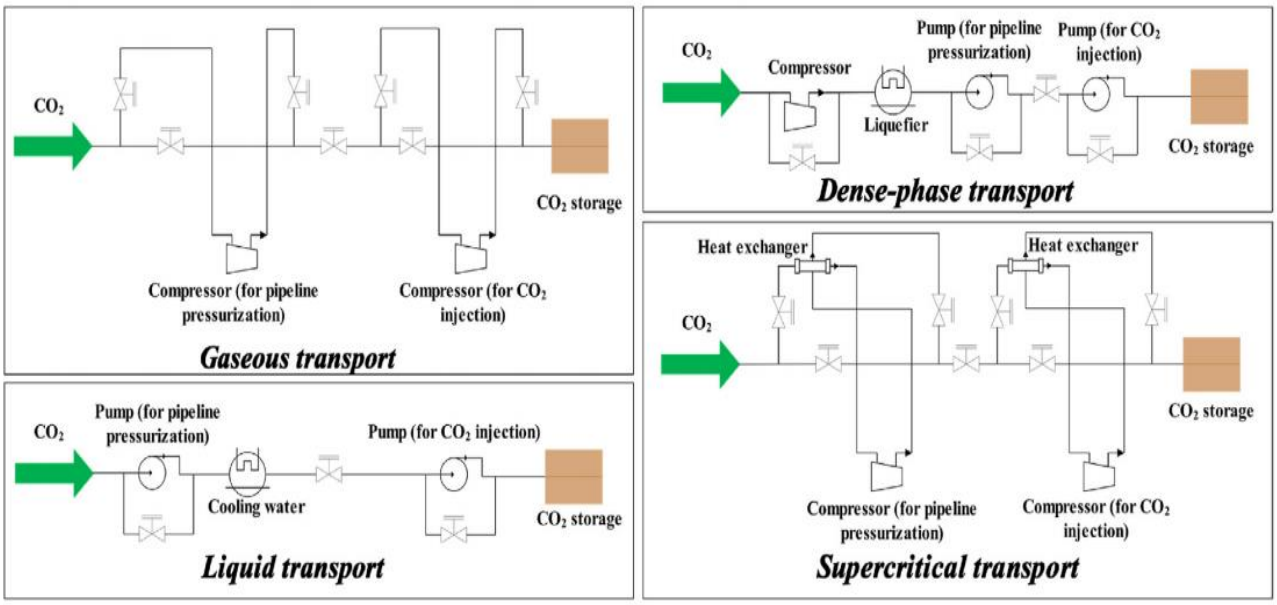

Figure 44 "Four process flow diagrams suitable for large-scale CO2 pipeline transport", (Ref.[15]).

Figure 44 shows the process flow chart of these four transport methods. Table 14 lists the transport features and applications of different methods. Through the summary of practice, gaseous transport and liquid transport can be used for short-distance pipelines, and dense-phase transport and supercritical transport can be utilized for long-distance pipelines. Among them, supercritical transport and dense-phase transport are more convenient. Some scholars or institutions have conducted some basic research regarding CO_2 transport. Zhang et al. (2006) studied the pressure drop of pipelines during CO_2 transportation. They concluded that the pressure along the pipeline continued to drop until the CO_2 evaporated, and the pipeline may eventually be blocked, thus inferring that the CO_2 transportation has the largest safe transportation distance. Yu et al. (2009) studied CO_2 transportation technology and concluded that the pressure drop of supercritical transport is greater than that of liquid transport and dense-phase transport, while that of liquid transport is greater than that of dense-phase transport. Wang et al. (2016) simulated the processes of different transport methods and performed a sensitivity analysis. Under gaseous transport conditions, the lower the temperature of the CO_2 pipeline inlet, the higher the pressure drop (Wang, 2017). Ambient temperature has a more significant impact on the pressure drop of the pipeline.

The higher the ambient temperature, the greater the pressure drop. Moreover, compared with the natural gas pipeline, if the operating conditions are the same, the CO_2 pipeline will have a smaller pressure drop than the natural gas pipeline, but the temperature drop is greater, and CO_2 is more likely to generate hydrates than natural gas. Therefore, the gaseous transport of CO_2 has high requirements for the control of temperature and pressure. When dense-phase transportation is adopted, the effect of the pipeline inlet temperature on the pressure drop is small and the effect on the temperature drop is substantial. With the increase of the transport distance, the influence of the ambient temperature on the pressure of the pipeline increases. The higher the ambient temperature, the greater the pressure drop of the pipeline. If supercritical transport is used, the influence of pipeline inlet temperature on pressure is small. However, during the transportation process, the temperature decreases rapidly, so that the phase transition will occur under a shorter transportation distance. Ambient temperature has less effect on the pressure drop of the pipeline but has a greater effect on the temperature drop. In addition, the author compared dense-phase transport with supercritical transport. Under the same conditions, the pressure drop of supercritical transportation is more significant. In dense-phase transport, the temperature of the pipeline will drop to ambient temperature, but no phase change will occur. However, supercritical transport may require additional heating stations to maintain temperature. Sinopec also did some basic research on the physical properties of CO_2 to provide a basis for the transport process. These studies allowed to develop the relationship curves between different parameters, including temperature-density, pressure-density, temperature-viscosity, pressure-viscosity. Moreover, some design companies are also carrying out relevant research, such as Project Consulting Services, in the United States, which have analysed the influence of impurities on pressure loss at different positions of pipelines. From the above review, it reveals that temperature and pressure control are key technologies in CO_2 pipeline transport, and the presence of impurities will have a high impact on transportation. Therefore, some scholars have studied the optimization of CO_2 pipeline transport. Zhang and Feng (2005) performed numerical simulations on the processes of supercritical transport and liquid transport for CO_2. It may be concluded that under appropriate climate conditions, the use of liquid transport could reduce operating energy consumption, and the use of pumps as pressurizing equipment can also lower the cost. Zhang et al. (2006) compared the supercritical transport with the subcooled fluid transport of CO_2. Through numerical simulation, they concluded that the subcooled fluid transport method could effectively improve energy efficiency, reduce costs under the conditions of isothermal and adiabatic transports, and that the scheme is more suitable for cold areas. Di (2013) conducted simulation and optimization studies on CO_2 pipelines, concluding that the presence of nitrogen and methane has little effect on the temperature and pressure drop of supercritical transport, but has a greater impact on liquid transport, and the impact of nitrogen is greater than methane. By optimizing the current project, it may be concluded that low pressure supercritical pressure boosting at the gas gathering station and the use of low-pressure supercritical transport can improve the economics of operation. Mohammadi et al. (2019) proposed an optimization framework to minimize the cost of CO_2 transport via pipeline, and they used genetic algorithms to find the solution with the lowest total cost. The results show that the pipe elevation and pipe diameter are the most critical parameters affecting costs. From the literature review it comes out that dense-phase transport and supercritical transport have more advantages in long-distance, large-scale CO_2 pipeline engineering, temperature and pressure control are still a key element in the transportation process. In recent years, some scholars have started research on transportation optimization, mainly considering the economic aspects of pipeline operation.

4.2.3 Pipe material strength

For CO_2 pipelines, temperature control is particularly important. The temperature of the pipeline is not only related to the inlet temperature, but also to the ambient temperature. Therefore, many researchers have analysed the thermodynamics of pipelines. Brown et al. (1996) proposed a computational model for tube bundle heat transfer. Zabaras and Zhang (1998) analysed the transient cooling performance of six different tube bundle structures. Jackson et al. (2005) analysed the effect of seawater around submarine pipelines on the adiabatic layer. Xie et al. (2014) analysed the leakage of the CO_2 pipeline using supercritical transport method. The results show that the thermal boundary layer in the pipeline is constantly changing when CO_2 leaks, and the convection intensity near the leakage point is the largest. Witkowski et al. (2014) proposed that the design of the CO_2 pipeline needs to consider the extreme conditions of the ambient temperature, and analysing the example the maximum transmission distance at 35 °C is 310 km. Li et al. (2014) studied the flow and heat transfer characteristics of CO_2 pipelines in case of leakage. They concluded that the mass flow rate and Nusselt number can be used for the leakage detection of CO_2 pipelines using supercritical transport method. Yu et al. (2017) experimentally studied the thermodynamic characteristics of the supercritical transport of CO_2 during decompression. The results show that the release of CO_2 will lead to the decrease of pressure, temperature and pipe wall temperature, and then tend to be stable, and the temperature drop in the initial stage is the largest. Wang (2017) performed a sensitivity analysis on the total heat transfer coefficient of CO_2 pipelines with different transport processes, and concluded that when CO_2 is transported in a gaseous state, if the total heat transfer coefficient is in the range of 0.84-3.02 ($W \cdot m^{-2} \cdot °C^{-1}$), the total heat transfer coefficient has a small effect on the pressure drop. When transported in the liquid phase, if the total heat transfer coefficient is in the range of 0.84-1.9 ($W \cdot m^{-2} \cdot °C^{-1}$), the total heat transfer coefficient has a small effect on the pressure drop. When dense-phase transport is adopted, the thermal insulation performance of the pipeline is not high. When supercritical transport is used, the total heat transfer coefficient has a small effect on the pressure drop. The review of thermodynamic analysis indicates that the analysis of thermal insulation and pressure drop during the CO_2 transport process is critical to the regular pipeline operation. At the same time, this is also the focus of flow assurance research.

4.2.4 Length

The CO_2 pipeline can be divided into large-scale and small-scale according to the length. According to the statistics, considering a total of 65 CO_2 pipelines in two important reports, the pipeline length ranges from 1.9 to 808 km, which is relatively broad. The shortest and longest pipelines are in the United States, the Decatur pipeline project (1.9 km) in Illinois and the Cortez pipeline project (808 km) in Texas. The longer the pipeline, the higher the designed transport capacity (Figure 46). Although there is no direct relationship between transport capacity and length, operating companies usually do so to maximize utilization. Since the longer the pipeline, the greater the pressure to be provided, the power of the initial booster is usually positively related to the length of the pipeline. If CO_2 is in the gas phase, compressors are used for pressurization. If CO_2 is in liquid or dense phase, pumps are used. For a long-distance pipeline, it is usually necessary to adopt a stepwise pressurization method, and multiple booster stations will be established along the way.

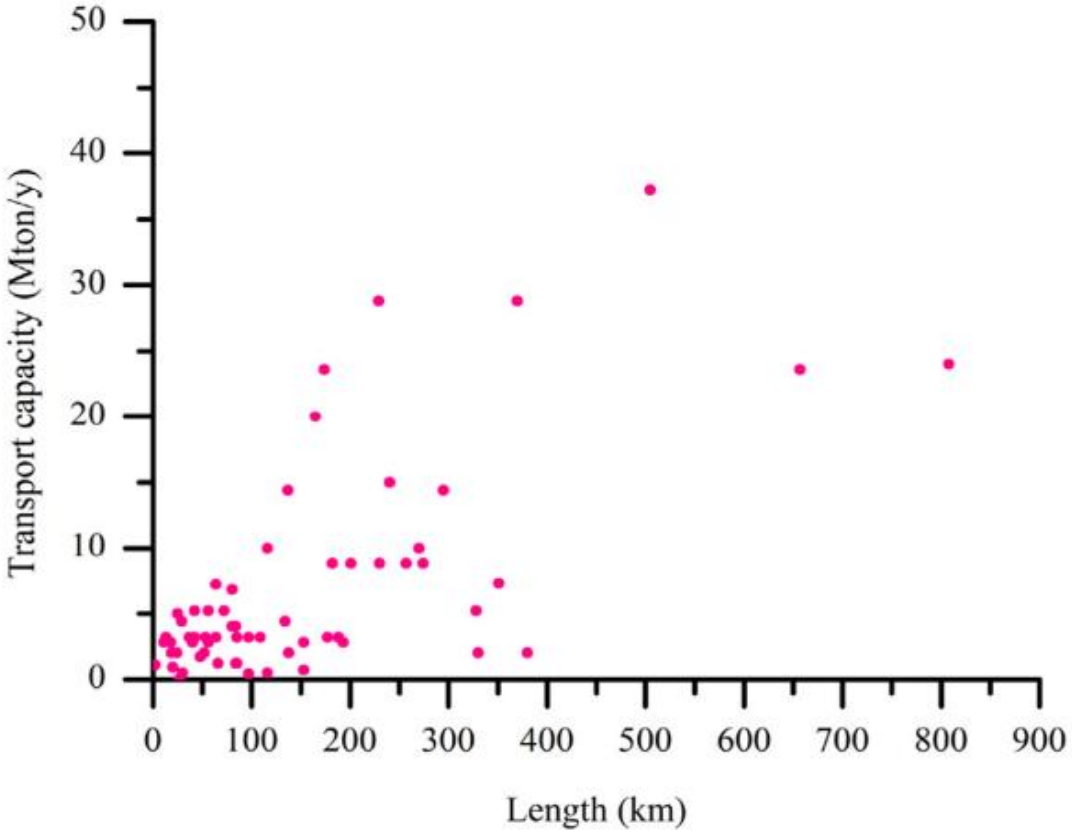

Figure 45 "Pipe length and transport capacity", (Ref. [15]).

Design parameter	High	Medium	Low
Length (km)	657–808	116–380	1.9–97
Transport capacity (Mt/y)	10–37	2.8–7.2	0.06–2
Initial booster power (MW)	43–68	15–17	0.2–8

Table 15 "Length, capacity, and initial booster power range of different categories of CO_2 pipeline", (Ref. [15]).

Based on the collected data of CO_2 pipeline projects, the Global CCS Institute divides them into three categories according to the transport scale; their length, capacity, and initial booster power range are shown in Table 15.

4.2.5 Diameter and wall thickness

In the design of CO_2 pipeline, the calculation of pipe diameter is the most important because it directly determines not only the transportation capacity, but it also determines the investment. Generally, the larger the pipe diameter, the greater the investment.

Therefore, the most reasonable choice is to minimize the pipe diameter based on compliance with transmission requirements. In the design of pipe diameter, in addition to the above factors, pressure, flow rate, and fluid flow should also be considered. The pipe wall is used to bear the internal and external pressure on the pipe. The larger the wall thickness, the higher the pressure bearing capacity of the pipeline, but at the same time, the investment will increase. Because CO_2 may be transported in different ways, the phase state should be considered in the design of wall thickness. Teh et al. (2015) proposed that if other conditions are the same, the wall thickness required for liquid transport is smaller than that for supercritical transport. Similarly, the Global CCS Institute divides the existing CO_2 pipeline projects into three categories according to pipe diameter and wall thickness, as shown in Table 16.

Design parameter	High	Medium	Low
Diameter (mm)	600–921	305–508	152–270
Wall thickness (mm)	19–27	10–13	5.2–9.5

Table 16 "Diameter and wall thickness range of different categories of CO_2 pipeline", (Ref.[15])

It can be obtained that the design of pipe diameter and wall thickness of CO_2 pipeline is based on the results of hydraulic analysis and stress analysis, just like that of natural gas pipeline. This means that the wall thickness needs to be determined according to the material of the pipeline under the premise of satisfying the transportation conditions. Under the same conditions, the higher the steel grade, the smaller the wall thickness required for the material, and it also means that the cost will be higher.

Steel grade (API 5L X grade)	Minimum yield strength (MPa)	Minimum tensile strength (MPa)
X52	359	455
X56	386	490
X60	414	517
X65	448	531
X70	483	565
X80	552	621

Table 17 "Properties of some common pipeline steels", (Ref.[15]).

Table 17 lists the characteristics of some common materials. As the transport pressure level of CO_2 may be higher than that of natural gas, a more conservative scheme is recommended for the design of wall thickness.

4.2.6 Pressure and temperature

Temperature and pressure directly determine the CO_2 transport state in the pipeline. A report states that for CO_2 to be transported under supercritical conditions, the temperature and pressure ranges should be 12-44 °C and 8.5-15 MPa, respectively. The temperature and pressure during CO_2 transport are not constant, and both fluctuate within a certain range. Among them, the lower pressure limit is based on the consideration of CO_2 supercritical transport, and the upper-pressure limit is based on economy and risk. For example, an offshore CO_2 pipeline can have a maximum pressure of 30 MPa because it is far away from populated areas. The lower temperature limit is based on the ambient temperature in winter, and the upper-temperature limit is determined based on the outlet temperature of the booster station and the temperature limit of the outer casing material.

Design parameter	High	Medium	Low
Maximum pressure (MPa)	15.1–20.0	9.8–14.5	2.1–4.0
Minimum pressure (MPa)	7.2–15.1	3.1–3.5	0.3–1.0

Table 18 "Maximum and minimum pressure range of different categories of CO2 pipeline", (Ref. [15]).

Another report pointed out that if CO_2 is transported in a low-pressure gas phase, the maximum pressure is 4.8 MPa. If the pressure is greater than 9.6 MPa, it can ensure that CO_2 can be transported in the dense phase at any temperature. The Global CCS Institute divides the pressure levels of CO_2 pipelines into three categories according to the minimum and maximum pressures (IEA Environmental Projects Ltd, 2014), as shown in Table 18.

4.2.7 Considerations

The pipeline route is determined by the source and destination of CO_2. It will not only determine the length of the pipeline, but also affect the design of the pressure, temperature, and material of the pipeline. The long-distance CO_2 pipeline may pass through different areas, the pipeline design and construction in different areas will also have different considerations, such as economy and special areas, as shown in Table 19 .

Area	Considerations
Urban area	The urban area should be avoided as much as possible because it will increase the construction cost, increase the construction period and increase the risk of the operation. However, the consideration of trenchless technology in pipeline installation can reduce the damage to urban pavement to a certain extent without affecting the traffic.
Land covered area	Some areas with steep slopes and unstable soil layers need to be avoided, such as landslides and seismic zones.
Pipeline colligate alure	Use existing facilities whenever possible.
Sensitive area	Sensitive areas such as nature reserves need to be avoided in principle.
Linear features	Linear features such as rivers, highways, and railways, trenchless technology can be considered for crossing.
Deepwater	Generally, it is necessary to select the areas with the flat seabed and deep seabed, so that the impact of wave load on the pipeline will be relatively small. However, this will also increase the construction cost. According to the existing engineering data, the depth of the CO_2 pipeline can exceed 2000 m (Metz et al., 2005).

Table 19 "Route selection considerations for different areas", (Ref.[15]).

One of the preconditions of construction is to obtain the right of way (ROW) (Figure 46). Therefore, before determining the route, it is usually necessary to give multiple schemes because the optimal scheme (less investment, short distance) is not necessarily feasible in law. According to the research, the acquisition of ROW may account for 4%-25% of the total construction cost, and ROW in suburban areas is easier to obtain than that in cities because there are fewer infrastructures. The construction of a CO_2 pipeline is similar to that of the oil and gas pipeline. For an onshore pipeline, three steps are required: installation and cleaning, connection with the compressor station (or pump station), air tightness test (or pressure test). For offshore pipelines, a pipelay vessel is usually required. In addition, trenchless technology has great potential in pipeline installation, not only has excellent advantages in urban and crossing projects, but also has faster speed and lower cost than traditional methods in offshore pipe laying.

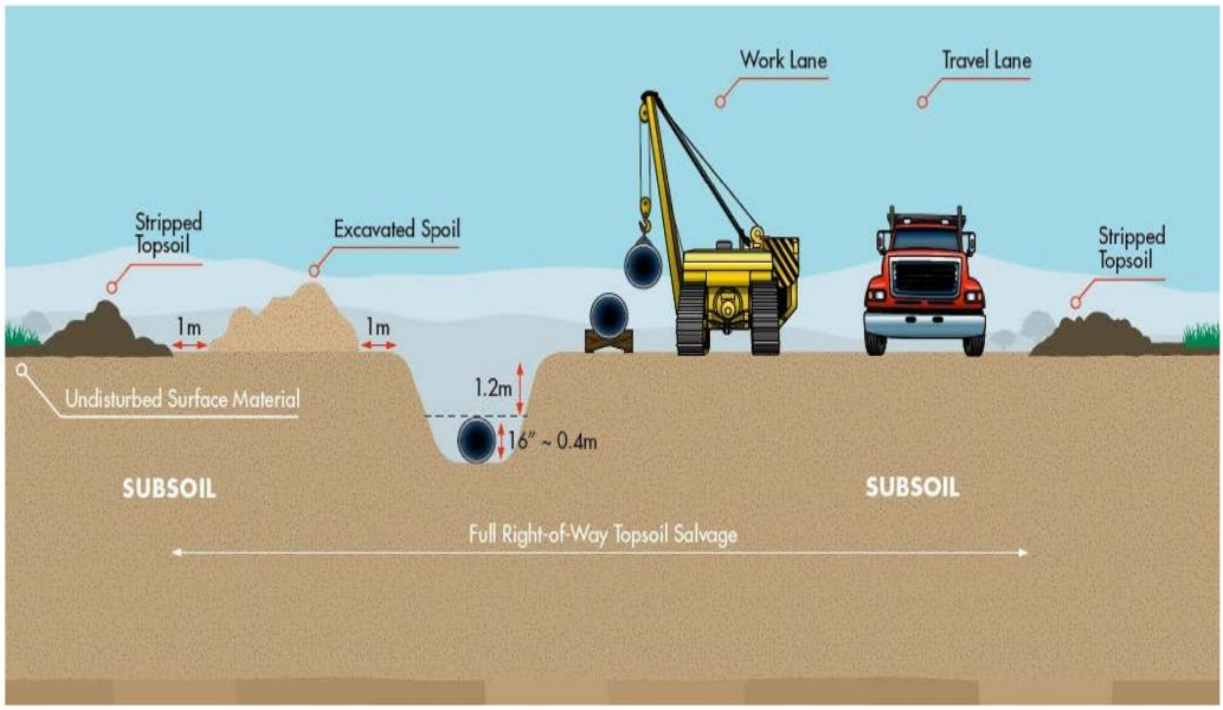

Figure 46 "ROW in CO2 pipeline construction", (Ref.[15]).

Note that the carbon footprint of trenchless technology is also much lower than that of traditional methods, and the more common trenchless installation technology is shown in Figure 47.

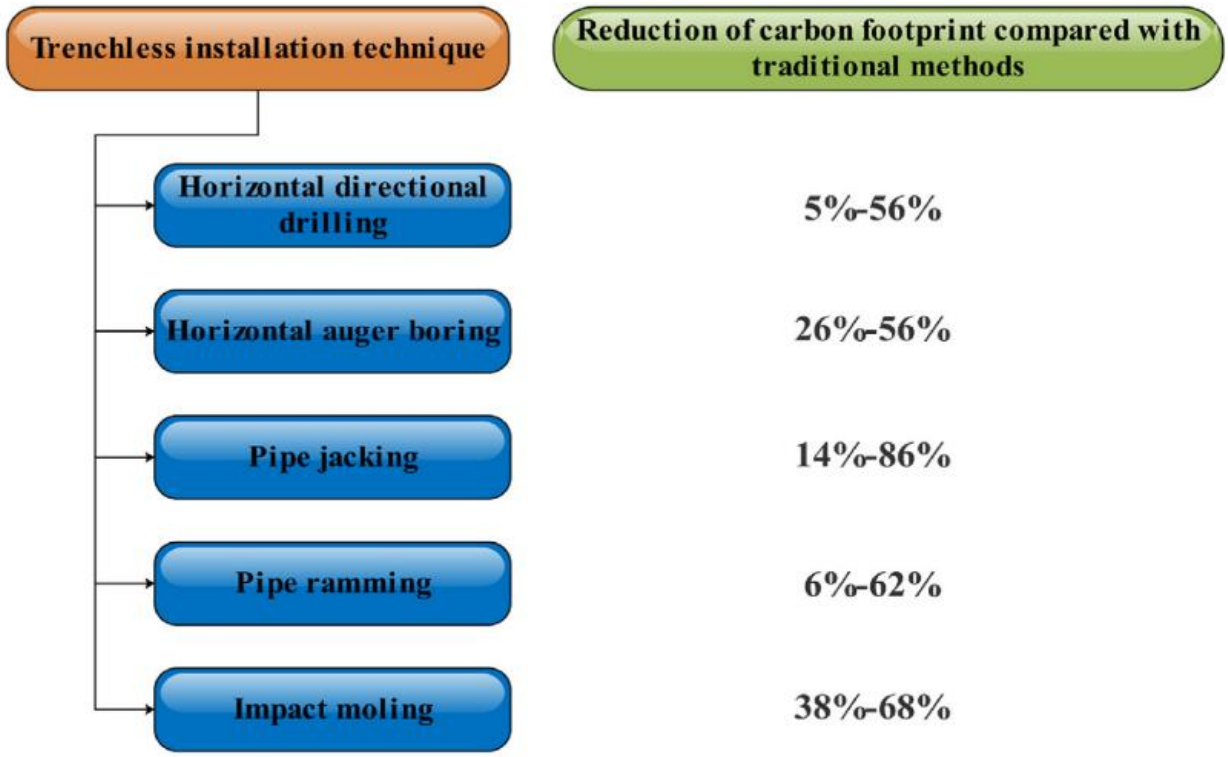

Figure 47 "Common trenchless installation technologies and their carbon footprint reduction ratio", (Ref.[15]).

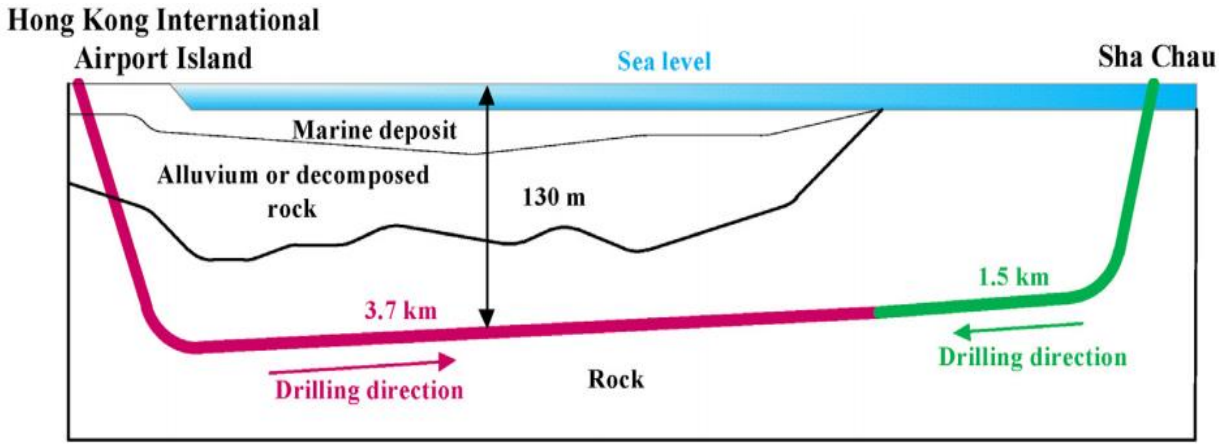

Figure 48 ". Schematic diagram of the Hong Kong International Airport HDD pipeline project", (Ref. [15]).

In May 2018, the Hong Kong International Airport completed the laying of two submarine pipelines using horizontal directional drilling (HDD) technology. Due to the long distance (5.2 km), the constructor used the method of laying from opposite ends and then splicing, as shown in Figure 48. It can be seen that the construction consideration of CO_2 pipeline is similar to that of natural gas pipeline, and new construction technology can be considered more in the future construction (Ref.[15]).

4.3 Conclusions and future works

In conclusion, from what has been said in these chapters, impurities (which can be different and have been extensively discussed in Chapter 2) play a fundamental role in the process of transporting carbon dioxide, in particular they cause significant changes to the thermodynamic properties of the flow and consequently imply technical and structural problems not indifferent to the pipeline, so the issues of maintenance and sizing are a very delicate subject and today are the intensively studied as they can represent an added value for future applications. The purpose of this review is to provide systematic information and reference about CO_2 pipeline for the designers and researchers. The primary findings are as follows:

I. Regarding the CO_2 pipeline process, the control of temperature and pressure has always been the focus of pipeline operation since the phase equilibrium of CO_2 containing impurities is complex. Further research is needed because the relevant knowledge system is not perfect

II. For the design of the pipeline, based on the existing projects, the scope and design points of various parameters are summarised. Although the CO_2 pipeline and natural gas pipeline are similar, their design considerations are still different. Temperature and pressure controls are stricter than for natural gas pipelines. In addition to the formation of hydrate, the phase state also needs to be considered. Construction considerations are similar to those of natural gas pipelines however some new construction technologies are recommended.

Research area	Future directions
Pipeline design	Effect of impurities on phase equilibrium
	Techno-economic framework for different CO_2 pipelines (Onyebuchi et al., 2018)
	Optimization of transport scheme, especially from the perspective of energy consumption and safety
Pipeline material	Ductile fracture index
	Corrosion mechanism of CO_2 pipeline in different environments
	Development of high-strength, corrosion-resistant steel
Pipeline construction	New construction technology, such as trenchless installation method
	Submarine pipeline construction
Safety and maintenance	Risk assessment system and method for CO_2 pipeline
	CO_2 leakage and diffusion mechanism
	Detection, monitoring, and emergency repair technologies for CO_2 pipeline
Management	Formulation of specifications and standards specifically for CO_2 pipelines
	Application of intelligent pipeline in transport deployment and monitoring
	Application of digital twin technology in safety management and early warning of CO_2 pipeline
	Establishment of CO_2 pipeline integrity system

Table 20 "Future research directions of CO2 pipelines", (Ref.[15])

Through the review of CO_2 pipeline transport technology, the current challenges and technical gaps are clarified. In terms of transport technology, it turns out that impurities in CO_2 have a great impact on the regular transportation of pipelines. However, there is still no systematic methodology to assess the impact of different impurities on the phase equilibrium and corrosion of CO_2 pipelines. In the field of pipeline safety, although there are many related research studies on oil and gas pipeline, the risk assessment and safety control of CO_2 pipeline still have not formed a system. Especially, the ductile fracture index and fracture control technology of the CO_2 pipeline are still developing slowly. In the field of CO_2 pipeline material research, the study of failure mechanisms and the development of corrosion-resistant and high-grade materials are also a major challenge. In terms of management, it is necessary to establish a techno-economic framework for the CO_2 pipeline, which will affect not only regulatory issues, but will also guide related policies. Furthermore, the literature review shows that the establishment of a pipeline maintenance system (such as detection, monitoring, emergency repair, etc.) is quite weak and standards for CO_2 pipelines are quite limited. While representing a challenge, the establishment of such a system also brings great opportunities. These hotspots focus not only on the CO_2 pipeline itself, but also on some interdisciplinary subjects, as shown in Table 20 (Ref.[15]).